Self-stabilization of 3D Walking of a Biped Robot

Qiuyue Luo

CENTRALE NANTES

THÈSE DE DOCTORAT DE

L'ÉCOLE CENTRALE DE NANTES

ÉCOLE DOCTORALE N° 601
Mathématiques et Sciences et Technologies de l'Information et de la Communication
Spécialité : *Automatique Productique et Robotique*

Par

« Qiuyue LUO »

« Marche Bipède 3D Auto-Stabilisante »

« Self-stabilization of 3D walking of a biped robot »

Thèse présentée et soutenue à « L'École Centrale de Nantes», le « 18/06/2020 »
Unité de recherche : UMR 6004, Laboratoire des Sciences du Numérique de Nantes (LS2N)

Rapporteurs avant soutenance :

Olivier Stasse, Directeur de recherche, LAAS, Toulouse
Andrea Cherubini, Maître de conférences HDR, Université de Montpellier

Composition du Jury :

Président :	Claude Moog	Directeur de recherche, CNRS, École Centrale de Nantes
Examinateurs :	Olivier Stasse	Directeur de recherche, LAAS, Toulouse
	Andrea Cherubini	Maître de conférences HDR, Université de Montpellier
	Jean Paul Laumond	Directeur de recherche, INRIA, Paris
	Yannick Aoustin	Professeur des Universités, Université de Nantes
Dir. de thèse :	Christine Chevallereau	Directrice de recherche, CNRS, École Centrale de Nantes

CONTEXTE ET ORGANISATION DE LA THÈSE

Motivation

Les robots humanoïdes, bien adaptés pour évoluer dans les milieux humains, peuvent avec leurs bras et mains effectuer des tâches complexes. Ils peuvent être considérés comme l'un des robots ultimes. Ils suscitent un grand engouement dans la société humaine car ils peuvent devenir des partenaires très utiles dans le quotidien et en milieux industriels. Cependant, la marche bipède reste un phénomène complexe qui n'a pas été entièrement compris. Les robots humanoïdes étant des systèmes très complexes avec des degrés de liberté (ddl) élevés, de nombreux modèles simplifiés ont été étudiés. L'un des modèles les plus simples et les plus populaires est le modèle pendule inversé linéaire (LIP) [1]. Avec le modèle LIP, le robot est supposé être une masse concentrée avec une accélération verticale nulle du centre de masse (CdM), des pieds pointus et des jambes sans masse. Une approche de commande classique est le modèle de commande prédictif (MCP) [2], qui a été utilisé pour de nombreux robots humanoïdes avec des pieds. Il peut être adapté dans de nombreux environnements complexes. Une autre méthode populaire est fondée sur les approches qui utilisent le point de capture (CP) [3] qui fonctionnent bien pour rejeter une perturbation comme une poussée extérieure appliquée au robot humanoïde. Ces approches, y compris certaines méthodes de commande basées sur l'optimisation [4], sont appelées commande de haut niveau, qui se réfère à des approches basées sur la prédiction des états futurs du CdM et des emplacements des pieds.

On sait que la marche des humains sur un sol relativement plat ne nécessite pas d'attention [5] et il existe une phase de déséquilibre pendant la marche. La stabilité de marche des êtres humains est obtenue en changeant alternativement la jambe de position. Un problème canonique est de savoir comment concevoir un correcteur basé sur la phase de déséquilibre. L'approche de commande basée sur les contraintes virtuelles [6] est un bon outil pour étudier ce problème. Les contraintes virtuelles sont les relations fonctionnelles entre les états du système, c'est-à-dire que les variables commandées sont définies comme

des fonctions d'une variable de mise en phase basée sur l'état interne du robot au lieu du temps. Cela signifie que lorsqu'une démarche est perturbée, le système n'a pas à se resynchroniser avec le temps après la perturbation. Avec un bon choix de contraintes virtuelles, une auto-synchronisation et une auto-stabilisation peuvent être obtenues. Les notions d'auto-synchronisation et d'auto-stabilisation se réfèrent à la synchronisation et à la stabilité obtenues sans commande de haut niveau mentionné précédemment. La notion d'auto-synchronisation qui a été proposée par Razavi et al. [7], se réfère aux périodes des mouvements pendulaires dans les plans sagittal et frontal tendant à une période commune.

En 2000, un groupe de laboratoires français comprenant Irccyn (l'ancien nom de LS2N) avec Université du Michigan (UM) construit Rabbit [8], qui est un robot planaire avec 5 corps et 4 actionneurs. Il y a donc 1 degré de sous-actionnement lors d'un simple appui du robot bipède sur le sol. Notez que comme il n'y a pas d'actionnement aux extrémités des jambes, ce qui fait avancer le robot est la gravité. Pour Rabbit, les quatre articulations actionnées sont choisies comme variables commandées. Un autre choix peut être la position du pied pivotant dans l'espace Cartésien ou l'orientation du torse. La variable de phasage doit être monotone. Ainsi, l'angle entre l'axe vertical et la ligne reliant le pied d'appui et la position CdM de la hanche ou sagittale peut être choisi comme variable de mise en phase. Lorsque les variables commandées suivent parfaitement l'évolution souhaitée, un système d'ordre réduit peut être obtenu, appelé dynamique zéro hybride (HZD) [9]. Dans les travaux de Chevallereau et Aoustin [10], il a été prouvé que dans l'espace 2D, la stabilité est obtenue si la vitesse du CdM est dirigée vers le bas à la fin d'une étape.

L'objectif général de la thèse est d'essayer de comprendre les conditions physiques que les allures doivent satisfaire dans l'espace 3D pour maintenir la stabilité dans la marche périodique, et de produire une stratégie de commande avec laquelle l'auto-synchronisation et l'auto-stabilisation peuvent être obtenues.

Organisation de la thèse

— Dans la première partie (Chapitre 2), le LIP modèle est utilisé pour étudier les stratégies de commande. L'influence du placement du pied libre sur le sol et les conditions de changement de jambe d'appui, en fonction du temps ou de l'état interne du robot sont étudiées. Il est montré que ni l'auto-synchronisation ni l'auto-stabilisation ne sont observées lorsque la commutation de jambe d'appui est fondée sur le temps ou lorsque la longueur et la largeur de pas sont fixes. D'autre part,

l'auto-synchronisation peut être obtenue lorsque la condition de transfert de la jambe d'appui est fondée sur une combinaison linéaire des positions du CdM le long des axes sagittal et frontal. De plus, l'auto-stabilisation peut être obtenue lorsque la vitesse du CdM dans le plan sagittal est prise en compte. Lorsque l'auto-stabilisation est obtenue, aucune méthode de commande du haut niveau n'est requise.

— Dans la deuxième partie (Chapitre 3), afin d'analyser l'influence de l'oscillation verticale du CdM du robot sur la stabilité de marche, le modèle de pendule inversé de longueur variable (VLIP) est utilisé. Il est démontré que l'oscillation verticale du CdM, le placement du pied libre et le choix de la condition de transfert jouent un rôle crucial dans la stabilité. De plus, un correcteur proportionnel intégral (PI) en fonction de la vitesse du CdM le long de l'axe sagittal est également proposé de telle sorte que la vitesse de marche du robot puisse converger vers un mouvement périodique choisi avec une vitesse de marche donnée.

— Dans la dernière partie (Chapitres 4-5) un nouveau modèle de marche, nommé le modèle essentiel est proposé. Il a la même dimension que le modèle 3D LIP mais il prend en compte la dynamique complète de l'humanoïde. Le modèle essentiel définit la dynamique de la position horizontale du CdM en fonction d'une trajectoire souhaitée du zéro moment point (ZMP). Les trajectoires de référence des variables commandées sont définies en fonction des états internes du robot et/ou d'informations externes, générant ainsi des modèles à des fins différentes. La stratégie de commande proposée pour les modèles LIP et VLIP est étendue à travers le modèle essentiel pour commander un modèle humanoïde complet. L'introduction du modèle complet modifie légèrement la gamme des paramètres qui conduisent à des allures auto-stables. L'algorithme de marche proposé ci-dessus est appliqué sur les robots humanoïdes Roméo et TALOS.

Certains des résultats de la thèse ont été publiés ou acceptés dans des conférences ou des revues.

Revues internationales

— Q. Luo, V. De-León-Gómez, A. Kalouguine, C. Chevallereau and Y. Aoustin, *Self-Synchronization and Self-Stabilization of Walking Gaits Modeled by the Three-Dimensional LIP Model*[J], dans IEEE Robotics and Automation Letters, 2018, 3(4): 3332-3339 (presenté dans IROS2018)

— Q. Luo, C. Chevallereau, and Y. Aoustin, *Walking Stability of a Variable Length Inverted Pendulum Controlled with Virtual Constraints*[J], dans International Journal of Humanoid Robotics, Vol. 16, No. 06, 1950040 (2019)

— V. De-León-Gómez, Q. Luo, A. Kalouguine, J.A. Pámanes, Y. Aoustin, and C. Chevallereau, *An essential model for generating walking motions for humanoid robots*[J], dans Robotics and Autonomous Systems, 2019, 112: 229-243.

Conférences internationales

— Q. Luo, V. De-León-Gómez, A. Kalouguine, C. Chevallereau, and Y. Aoustin, *Self-Synchronization and Self-Stabilization of Walking Gaits Modeled by the Three-Dimensional LIP Model*, communiqué dans 2018 IEEE/RSJ International Conference on Intelligent Robots and Systems, October, 1-5, 2018 Madrid, Spain.

Acknowledgement

My deepest gratitude goes first to my supervisor Prof. Christine Chevallereau and Prof. Yannick Aoustin who have put their valuable experience and wisdom at my disposal. They provided critical advices in my researches and suggested many important additions and improvements. It has been a greatly enriching experience to me to work under their authoritative guidance. I also thank Dr. Víctor De-León-Gómez and Dr. Anne Kalouguine for their suggestions and comments of my research work. I have spent a great time working with them.

I would also like to express my gratitude to the China Scholarship Council (CSC) for providing me the financial support during the three years.

I want to thank Dr. Abhilash Nayak, Mario Ciranni, Yang Deng, Vamsi Krishna GUDA, Yankai Xing for sharing their knowledge with me and helping sloving my confusions when I met a problem in my work. In Nantes, I am lucky to have many friends from China who are studying in different research areas so that we can share different stories and life experiences together. Thank you all for caring about me and the sincere encouragement.

Last but not least, I want to express my gratitude to my parents, who encourage me to pursuing the PhD for the subject I am passionate about, with their endless love and selfless support.

Abstract

Humanoid robot, which can walk by two legs and perform skillful tasks using both arms with hands, could be considered as one of the ultimate robots. They are especially desirable in human society as they can work well in the environments that have been designed for humans, and become our partners. However, bipedal walking remains a complex phenomenon that has not been fully understood.

The thesis is dedicated to find some physical insights that can explain the stability of periodic walking on horizontal floor. In human walking, the gait is usually expressed as a function of a phasing variable based on the internal state instead of time. The controlled variables (swing foot trajectories, vertical oscillation of center of mass, upper body motion, etc.) of the robots are based on a phasing variable via the use of virtual constraints and the step timing is not explicitly imposed but implicitly adapted under disturbances.

In the first part, a simplified model of the robot: the linear inverted pendulum (LIP) model is used to study control strategies. Landing positions of the swing foot, and conditions to switch the stance leg, based on time or on the internal state of the robot are studied. It is shown that neither self-synchronization nor self-stabilization is observed when the stance leg switching is based on time or when both the step length and width are fixed. On the other hand, self-synchronization can be obtained when the switching condition of the stance leg is based on a linear combination of the positions of the center of mass (CoM) along the sagittal and frontal axes. Moreover, self-stabilization can be obtained when the velocity of the CoM in the sagittal plane is taken into account. When self-stabilization is obtained, no high-level control methods are required (such as model predictive control, capture point-based control, optimization-based control etc.).

In order to analyze the influence of the vertical oscillation of the robot CoM on walking stability, the variable length inverted pendulum (VLIP) model is used. It is shown that the vertical CoM oscillation, positions of the swing foot and the choice of the switching condition play a crucial role in stability. Moreover, a PI controller of the CoM velocity along the sagittal axis is also proposed such that the walking speed of the robot can converge to a chosen periodic motion with a given walking speed.

In the last part, the essential model is proposed, which is a novel model for walking that

has the same dimension as the 3D LIP model but considers the complete dynamics of the humanoid. It can be written based on the internal states of the robot and possible external information, thereby generating models for different purposes. The essential model defines the dynamics of the horizontal position of the CoM as a function of a desired trajectory of the ZMP, assuming a perfect tracking of the reference trajectories. The proposed control strategy for the LIP and VLIP models is extended through the essential model to control a complete humanoid model. Introducing the complete model modifies slightly the range of parameters leading to self-stable gaits. The walking algorithm proposed above is applied on the humanoid robots Romeo and TALOS.

Key words: Humanoid and bipedal locomotion, passive walking, dynamic stability, hybrid systems, modeling

Table of Contents

Chapter 1

Introduction

1.1 Background

Humanoid robots, which can walk with two legs and perform skillful tasks using both arms with hands, could be considered as one of the ultimate robots. They are especially desirable in human society as they can work well in indoor environments and use the tools that have been designed for humans, and become partners of human beings. Back in 1996, the great success of HONDA humanoid robot boosted worldwide research on humanoid robots [11]. Developing a humanoid robot that is able to accomplish the tasks like human beings is not only an academic pursuit, it also becomes a more and more imperative issue due to the labor shortages caused by declining global birthrate.

One of the applications of humanoid robots is service robotics. It can work as a life companion, a housekeeper, a reception or a security guard. Thanks to their anthropomorphic appearance, it is easier for human beings to interact with them in the daily life. Humanoid robots can also be used to take care of aged people and monitor their health situation.

Besides service robotics, it is also expected that humanoid robots can be used in disaster rescue and work in an environment that is impossible or dangerous for human-beings, such as the earthquake, tsunami, nuclear accidents, space exploration or work in an environment full of contagious virus or bacteria, such as the outburst of COVID-19 happened lately [12]. It would be better to use robots to replace human beings when performing daily care or delivery of food to the quarantined people.

Humanoid robots will play a crucial role for building the factory of future. In some environments such as building sites, aircraft facilities or shipyards, robot technologies can assist workers to accomplish some specific tasks. It is difficult to rebuild the facilities that have been designed for human beings to be suitable for robots. Because humanoid robots physically resemble people, they can work without requiring environmental changes, possibly relieving workers of heavy labor.

Knowledge of humanoid robots can also be useful for medical application and rehabilitation. The knowledge of humanoid equilibrium or walking can be useful to build exoskeletons, prostheses or rehabilitation systems.

1.2 The development of humanoid robots

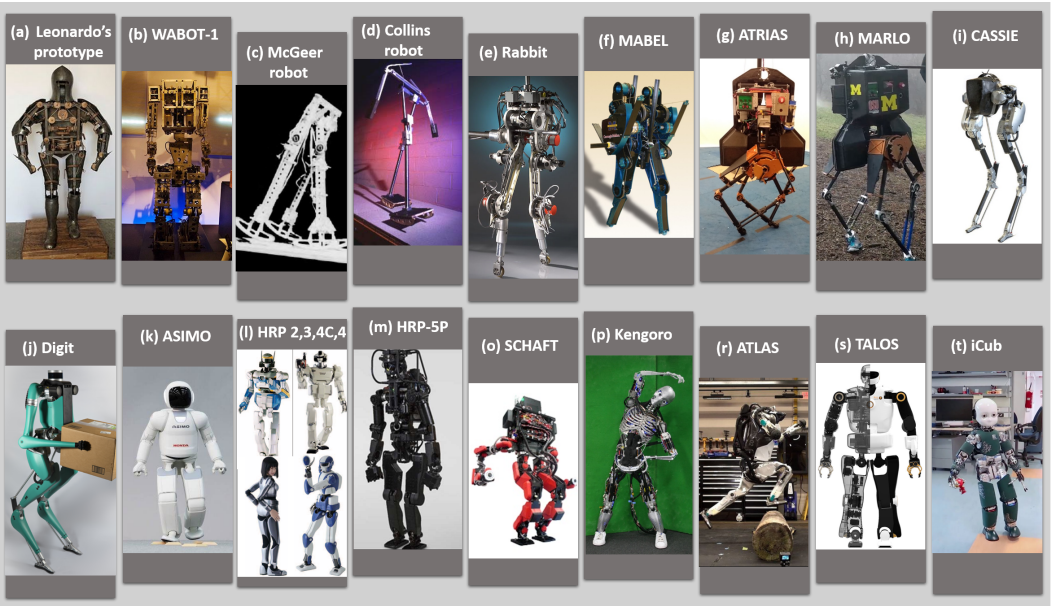

Figure 1.1 – Presentation of different robots.

Back in 1495, Leonardo da Vinci, one of the greatest geniuses of the Italian Renaissance, designed and constructed a mechanical knight, which cannot be called a 'robot' yet. In 1970s, Takanishi Laboratory of Waseda University developped the world's first full-scale anthropomorphic robot WABOT-1 [13]. This robot was able to perform static walking.

In 1990, McGeer [14] built the first planar passive robot with four links. It is able to walk down a slope with only the gravity. Passive robots have the advantage of very high walking efficiency. They have no static stability but only dynamic stability. Then Collins et al. [15] developped a passive robot in three dimensional (3D) space. By adding some actuators to control certain joints, the robot is able to walk in the flat ground. Initiated in 1997, a robot, named RABBIT [16] was developped and able to perform dynamic motions, such as high speed walking and running. It was a joint effort by several French research

laboratories and University of Michigan. RABBIT has point feet, and only 2D motion in the sagittal plane is considered. This project has contributed two major achievements: the concept of virtual constraints [6], and the concept of hybrid zero dynamics (HZD) [9,17]. Researchers from University of Michigan developped MABEL robot [18], which was the world's fastest bipedal robot with knees back then. From 2D to 3D, researchers from Oregon State University developped ATRIAS robot [19]. At the same time, researchers from University of Michigan were also working on the same prototype, and they named it MARLO [20]. Under their efforts, this prototype succeeded to conquer terrain with innovative control algorithms. In 2016, researchers built Cassie [21], which is the result of engineering optimization on the design principles of ATRIAS. Both ATRIAS and Cassie were licensed to Agility Robotics for commercialization. In 2019, Agility Robotics added the upper body and created a humanoid robot named Digit [22] which is able to navigate in complex environments and carry out tasks like package delivery. In January 2020, Agility Robotics has announced that Digit is now for sale.

The famous ASIMO robot [23] was shown to the public around 2000. Until now, after several major upgrades, it is capable of accomplishing a serial of highly difficult tasks, such as high speed running, jumping, walking on an uneven ground and climbing up and down stairways.

Another famous robotic platform from Japan is the HRP series, including HRP-1 [24], HRP-2 [25], HRP-3 [26], HRP-4 [27], HRP-4C [28] and the latest model HRP-5P [29]. In the development of the HRP series, AIST has collaborated with several private-sector companies, including Kawada Industries Inc. (now Kawada Robotics Corp.), and has developed basic technologies for practical application. HRP-2 was capable of bipedal walking, lying down, standing up, walking on narrow paths, overstepping large obstacles [30] and other actions [31, 32]. HRP-3 could walk on slippery surfaces and tighten bolts on bridges by remote control. HRP-4 has achieved the new, light-weighted and slim body while succeeding the concept of the conventional models HRP-2 or HRP-3, where the robots coexist with humans and assist or replace human operations or behavior. Within the series, HRP-5P has unsurpassed physical capabilities enabling it to substitute for people doing heavy labor.

In the DARPA Robotics Challenge held in 2013, SCHAFT robot [33], originally designed in Jouhou System Kougaku (JSK) robotic laboratory of the University of Tokyo and now owned by SCHAFT Inc., performed surprisingly well and won the championship. The JSK robotic laboratory also developped a bio-inspired musculoskeletal robot Kengoro [34].

What is special about this robot is that it imitates sweating to cool its high-torque motors. Until now, Kengoro is capable of doing push-ups and playing badminton, but not walking yet.

There is no doubt that the most amazing humanoid robot in 2019 is Atlas built by Boston Dynamics. In 2019, the successful backflip [35] and 'parkour' [36] demonstrated by Atlas have drawn attention from all over the world, especially that of researchers working in the field of humanoid robotics. Equipped with 28 hydraulically actuated joints, Atlas is capable of carrying objects and performing highly dynamic locomotion. Some European institutions have also developped some impressive humanoid robots, such as TALOS [37] by PAL Robotics and iCub [38] by Italian Institute of Technology (IIT). Figure 1.1 presents the robots mentioned above.

Starting late in the field of humanoid robotics, China is playing catch-up, and also has achieved some significant results. It is worth mentioning that the walker robot (shown in Figure 1.2) developped by Ubtech Robotics is now capable of accomplishing a range of indoor tasks, aiming to be 'an intelligent bipedal humanoid robot that is an indispensable part of your family' [39].

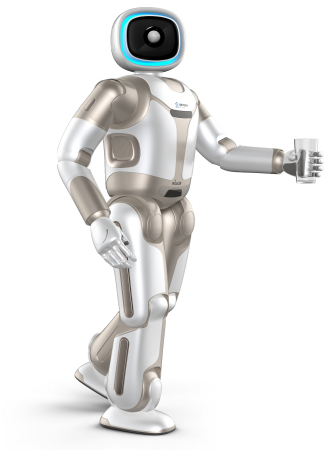

Figure 1.2 – The walker robot.

Over the last 50 years, humanoid robots have evolved a lot. From being barely able to walk, to 'parkour' and interacting with human beings. This great evolution is a joint effort of many generations of researchers who devoted themselves to the field of humanoid robots. We believe that in the near future, the combination of artificial intelligent (AI) and humanoid robots will create more miracles, and the dream of having robot partners

described in the films can be realized.

1.3 Gait patern generation

1.3.1 Control with Simplified model

As humanoid robots are very complex 3D systems with high numbers of degrees of freedom (DoF), many simplified models have been proposed to understand their dynamic behaviors better. One of the most used simplified models is the 3D linear inverted pendulum (LIP) model proposed by Kajita [1, 40]. This model assumes that the mass of the humanoid robot is concentrated in its center of gravity with a zero vertical acceleration. The 3D LIP model is interesting because an analytical expression to define the center of mass (CoM) evolution exists and its dynamics in sagittal and frontal planes are decoupled. In [41], authors assumed that the CoM moves along a slope by using the LIP model so that the robot can walk on a rugged terrain.

One of the main difficulties of walking studies is the equilibrium of the robot, i.e. to satisfy the contact hypothesis and in particular to avoid the rotation of the stance foot. Thus, the constraint on the Zero Moment Point (ZMP) is crucial (see [42]). The ZMP is a point where the horizontal ground reaction moment of the ground reaction force is zero. The tipping over of the support foot can be avoided as long as the ZMP is located inside the support polygon (the convex hull of the feet contact area). In this case, the ZMP is identical to the CoP (center of pressure) [43]. To deal with the ZMP error caused by the difference between a simple model and the precise multibody model, Kajita et al. [2] used model predictive control (MPC) with the LIP model to plan the CoM walking pattern. Wieber [44] improved this method by continuously taking into account the actual state of the robot to deal with strong perturbations. Similar work has been done by Nishiwaki et al. [45].

Englsberger et al. [3] proposed a capture point (CP) based controller, which decomposes the 3D LIP model into two cascaded first-order systems. The capture point proposed by Pratt et al. in 2006 [46] is a point on the ground where the robot can step to in order to bring itself to a complete stop. The CP based controller exploits the natural dynamics of the LIP in order to get a gait pattern generator. This result was then extended to 3D in [47].

In [4] an optimal control problem using an approximate value function derived from

the 3D LIP model while respecting the dynamic, input, and contact constraints of the full robot dynamics is solved. Recently, in [48] the 3D LIP model was used to design a biped walking pattern based on a new way of discretization named spatially quantized dynamics (SQD). In [49] the 3D LIP model is studied along with their energy-optimal gait planning based on geodesics in order to achieve a stable walking gait. As shown, the 3D LIP model is still largely used in the literature, however, as it is an approximate model, the resulting walking gaits cannot be directly implemented, since they do not have the same performance when they are realized by the complete model. Therefore, as shown in these works, complementary control techniques or adjustments must be taken into account.

1.3.2 Passive based control

Completely passive robots [14, 15, 50] have very high walking efficiency, but they can only walk down a slope and are very sensitive to the physical parameters and external environment. Many researches tried to focus on underactuated walking by adding some control methods based on passive walking, so that the robots can walk on a flat ground or up a slope.

Goswami et al. [51] developped an active control scheme that mimics a passive system by tracking a virtual energy field, assuming that the hip as well as the ankles are actuated. Asano et al. [52, 53] introduced virtual passive dynamic walking with a virtual gravity field using robot actuators, which mimics the gravity field observed in slope walkers. Then they proposed an energy-constraint control and a stable walking pattern can be generated [54, 55]. Spong et al. [56] proposed a method based on the so-called controlled symmetry independent of the particular ground slope.

For an underactuated system, the stability is studied for the hybrid dynamic model. The stability of an underactuated system is not ensured at each instant but for the complete cycle. The underactuated walking gait is usually periodic, and is represented by stable limit cycles [57] in the phase space of the robot. The Poincaré return map [6, 58], is the appropriate mathematical tool for analyzing the stability of periodic orbits for underactuated systems. In this context, the stability is the convergence toward an orbit or periodic motion.

1.3.3 Virtual constraints and hybrid zero dynamics (HZD)

When constraints are imposed on a system via feedback control, we call them virtual constraints [6, 59]. The virtual constraints are functional relations among the evolution of various links and an internal phasing variable based on the system's states instead of time. In many researches [6,60–64], the stance leg angle is used to be the phasing variable for defining the remaining states, while in some others like [65], the position of robot's hip along the sagittal axis is used. The notion of virtual constraints is combined with the concept of HZD proposed by Westervelt et al. [9,66], which is a low-dimensional submodel of the closed-loop hybrid robot model assuming that the control law zeroes the controlled output.

Many researchers [6, 67, 68] used the method of virtual constraints to transfer the problem of motion planning to the parameter optimization of the virtual constraints. Grizzle et al. [69,70] designed an event-based PI controller based on the restricted Poincaré map of the HZD to regulate the robot's average walking rate. Griffin and Grizzle [71] introduced a class of virtual nonholonomic constraints that depend on velocity through (generalized) angular momentum. Including angular momentum in the virtual constraints allows foot placement control to be designed on the basis of the full dynamic model of the biped. This method leads to a new class of control laws that are robust to a variety of common gait disturbances. Then the method of virtual constraints and HZD were extended to 3D underactuated walking in [72–75]. Westervelt et al. [66, 76] proposed a sample-based HZD control, which does not use a pre-chosen family of virtual constraints, to enlarge the basin of attraction of the gait of a passive dynamic walker.

The stability of a 3D walking system can be achieved depending of the chosen virtual constraints. The stability can be tested numerically via the Poincaré approach. The approach based on virtual constraints and HZD was chosen because it is a good compromise between the passive walking which has a good energetic performance and the ZMP based approach which ensures a good contact of the foot with the ground but does not necessarily take advantage of the role of gravity as the driving source of walking. And numerical approaches, like optimization [68], can be used to obtain stable and robust gaits. Different from the methods mentioned above, one objective of this thesis is to try to understand the physical condition that the gaits must satisfy to produce stable walking.

1.4 Overview and outlines of the dissertation

Our objective is to try to understand what are the physical conditions that the gaits must satisfy to produce stable walking and to produce a control strategy that does not require high-level control, since we assume that humans' walking on even grounds does not require attention [5, 77]. The high-level control represents the control approaches where several online adjustments must be defined in order to achieve stability. This includes methods based on prediction (or preview control), online optimization, and event-based control that updates the parameters of the controller to stabilize the walking. The terms of *self-synchronization* and *self-stabilization* are used when synchronization or stabilization of walking gaits can be achieved without high-level control. Razavi et al. first introduced the notion of synchronization for the 3D LIP model in 2015 [7], which refers to periods of the pendular motions in the sagittal and frontal planes tending to a common period.

After this short introduction, Chapter 2 proposes a walking algorithm with which self-synchronization and self-stabilization can be obtained for the robot modeled by the 3D LIP model. In [78], Razavi et al. introduced an ellipse-shaped switching manifold to achieve self-synchronization. Inspired by this work , this chapter proposed a new switching manifold that works for a more general choice of swing foot locations, and introduces a phasing variable to coordinate all the joint motions. Different conditions to switch the stance leg, based on time or on the internal state of the robot are studied first. At the same time, different landing positions of the swing foot are also studied. Besides synchronization, walking stability of robots is another dominant feature to be analyzed. In this chapter, a slight modification of the switching manifold is proposed to achieve self-stabilization. Different from [79], the step timing applied in this chapter is not explicitly but implicitly adapted by the transition between steps based on the CoM position. The MATLAB® code of the proposed walking algorithm can be found on GitHub [80].

The objective of Chapter 3 is to find some physical conditions that lead to self-stabilization based on a simplified model with vertical CoM oscillation. How the features of the switching surface and the vertical motion of the CoM affect the stability of the system has been analyzed. As an extension of Chapter 2, this chapter proves that for a variable length inverted pendulum (VLIP) model, self-stabilization can be obtained when the switching condition is based on a linear combination of the CoM positions along the sagittal and frontal axes. Moreover, it is proved that when the CoM velocity feedback in the sagittal plane is taken into account, the system is able to converge asymptotically to

a new periodic motion without the complex procedure of finding a periodic motion.

Chapter 4 proposes a new model of the same dimension as the 3D LIP model, i.e. of dimension four, that considers the whole dynamics of humanoid robots. The new model is called essential model. This model has been developed by taking into account the notion of HZD, which is a very useful tool to analyze the internal dynamics of a system [81]. Unlike the 3D LIP model, the essential model is not based on a mechanical approximation (concentrated mass) of the robot. Instead, the motion and dynamics of the whole robot body are taken into account. With this model, it is possible to impose a desired location for the ZMP during the whole step or make the ZMP follow a desired path while the robot performs its motion. Then the applications of this model to the humanoid robots Romeo and TALOS with different walking patterns are presented in the end of this chapter.

Chapter 5 discusses the stability of the HZD that considers the complete dynamics of the robots Romeo and TALOS with the walking algorithm proposed in Chapters 2 and 3. Different walking patterns are considered: different swing foot motion, different vertical CoM motion, the switching manifold configuration. A general conclusion can be deduced on the design of a gait that proper choices of virtual constraints will lead to a stable walking. The condition that the transition from one step to the following one should be based on the horizontal position of the CoM is one major criterion. One other very important characteristic is the choice of the foot position that must be designed in order to prepare the next step, because the relative position of the CoM with respect to the stance foot at the beginning of the step is an essential condition. Similar results are obtained while studying the cases of the robot Romeo and TALOS. This suggests that the conclusion can be extended to many humanoid robots.

Finally, several concluding remarks and perspectives are discussed in Chapter 6.

1.5 Contributions of the dissertation

The main contributions corresponding to this work are the followings:

C1. Analysis of the physical conditions that the gaits must satisfy to produce a stable walking;

C2. Design of a novel walking algorithm based on virtual constraints and HZD to imitate the intrinsic nature of human walking without using online optimization or predictive control methods;

C3. A phasing variable based on the internal state of the CoM has been proposed to

coordinate the evolution of joints instead of time;

C4. An essential model has been proposed, which is a novel dynamic model that has the same dimension as the 3D LIP model but considers the complete dynamics of the robot. This essential model is especially useful for fully actuated humanoid robots with feet, because it is able to generate walking gaits that ensures the ZMP to be kept in an expected position or trajectory;

C5. The proposed walking algorithm has been validated on simplified models (i.e. LIP model and VLIP model), and then extended to the study of humanoid robots considering the complete dynamics.

Chapter 2

Self-synchronization and self-stability of LIP model

2.1 Introduction

The linear inverted pendulum (LIP) model is often used to study walking gaits, but the transition from one step to the following step is often neglected, while it is really important for the walking stability. This chapter studies different landing positions of the swing foot, and different conditions to switch the stance leg, based on time or on the configuration of the robot. It is shown that self-synchronization of the motion in sagittal and frontal planes is dependent on different switching conditions. Neither self-synchronization nor self-stabilization is observed when the stance leg switching is based on time or when both the step length and width are fixed. On the other hand, self-synchronization can be obtained when the switching condition of the stance leg is based on a linear combination of the positions of the center of mass (CoM) along the sagittal and frontal axes. Moreover, self-stabilization can be obtained when the velocity of the CoM in the sagittal plane is taken into account. Finally, the robustness of a pendulum walking on uneven grounds is discussed.

This chapter is outlined as follows: Section 2.2 introduces the hybrid dynamic model for LIP; Section 2.3 introduces the vertical and horizontal trajectories of the swing foot; Section 2.4 introduces the Poincaré method; Section 2.5 presents the instability of the periodic motion in the case when the transition is based on time; Section 2.6 and Section 2.7, propose switching conditions that lead to self-synchronization and self-stabilization of the walking gait; In Section 2.8, walking on an uneven ground is simulated to show the robustness of the proposed method; Finally, several concluding remarks are discussed in Section 2.9.

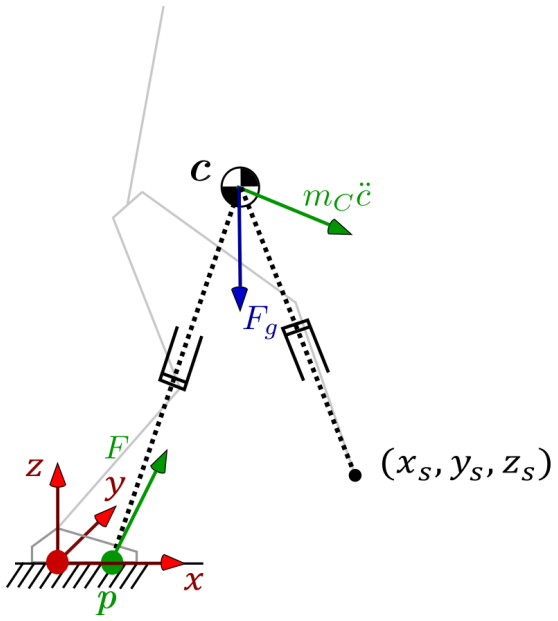

Figure 2.1 – A simplified model of a 3D biped robot.

2.2 Modeling of the walking gait via LIP model

2.2.1 General description.

In 3D LIP model, the robot is approximated as a point mass with point feet and the CoM trajectory is constrained to a plane for 3D walking. In this chapter, the CoM trajectory is constrained to a horizontal plane. The gait is composed of two phases: single support (SS) phase and double support (DS) phase. During the SS phase, while one foot is stationary on the ground, the other foot swings from the rear to the front. For the DS phase, the following hypotheses are imposed:

— The DS phase is instantaneous;
— The swing leg naturally lifts from the ground without interaction;
— The contact between the swing leg and the ground doesn't modify the velocity of CoM [40];
— The foot of the robot is considered as a point.

2.2.2 Model in SS phase.

In Figure 2.1, a simplified model of a 3D biped robot is illustrated. Each leg is massless and has variable length. The robot is assumed to have 6 DoFs : 4 rotations and 2 prismatic

joints. Among them, 4 DoFs are active: the 2 prismatic joints and the 2 rotational joints at the hip. The other 2 DoFs (i.e. the 2 rotations at the stance ankle) are passive. At the contact point, the stance leg rotates passively around x and y axes, the rotation around z axis is not considered since this rotation is usually inhibited by friction in normal biped locomotion. There are two degrees of freedom (DoFs) at the hip, allowing to control the positions of the swing foot along x and y axes. The rotation along the leg axis is not considered since it does not modify the positions of the swing foot. When the robot is considered as a whole, the two fundamental equations of dynamics, the equilibrium in translation and in rotation around the CoM, give a dynamic model that highlights the difficulty of walking, also called the Centroidal model [82] (see Figure 2.1). Here, the position of the CoM is denoted by $c = [x_c,\ y_c,\ z_c]^\top$, and the mass of the robot is denoted by m_c. The linear acceleration of the CoM is $\ddot{c}$ and its angular momentum around the CoM is denoted as $\mathcal{L}$ [1]. In this model, the external forces that act on the robot are emphasized, which are: the gravity force denoted as $F_g = [0, 0, -m_c g]^\top$ where g is the gravitational acceleration; the reaction force and moment applied by the ground is written as $F = [F_x, F_y, F_z]^\top$ and $M = [0,\ 0,\ M_z^*]^\top$. Thus, the dynamic equation can be written as

$$m_c \ddot{c} = F_g + F, \tag{2.1}$$

$$\dot{\mathcal{L}} = (p - c) \times F + M, \tag{2.2}$$

where $p = [p_x,\ p_y,\ p_z]^\top$ denotes the CoP point. The constraint of the contact wrench to avoid takeoff, sliding and rotation of the support foot can be expressed based on equations (2.1) and (2.2) for any humanoid robot.

— The constraint of no takeoff implies that $F_z > 0$, i.e. from the third row of (2.1), $\ddot{z} > -g$.

— The constraint of no slipping implies that $F_{tan} = \sqrt{F_x^2 + F_y^2} < \mu F_z = F_{fric}$, where μ is the friction coefficient between the sole of the support foot and the ground. This constraint can be also written in terms of the acceleration of the CoM, i.e. $\ddot{x_c}^2 + \ddot{y_c}^2 < \mu^2(\ddot{z_c} + g)^2$.

— The constraint of no tipping of the foot implies that the ZMP is always kept inside the convex hull of the support area, i.e. CoP = ZMP. This constraint cannot be

1. For a multi-body system, the angular momentum around the CoM is given by $\mathcal{L} = \sum_{i=1}^{N} [I_i \omega_i + m_i (c - c_i) \times v_i]$, where N is the number of bodies of the robot, I_i is the inertia tensor at the CoM$_i$, ω_i is the angular velocity and c_i and v_i are the position and velocity of the CoM$_i$

easily written in terms of $\ddot{c}$.

The last condition is the most constraining, therefore it is important to know the position of the CoP during all the walking gait. This position can be easily obtained from equations (2.1) and (2.2) as

$$p_x = x_c - \frac{z_c \ddot{x}_c}{\ddot{z}_c + g} - \frac{\dot{\mathcal{L}}_y}{m_c \ddot{z}_c + m_c g}, \tag{2.3}$$

$$p_y = y_c - \frac{z_c \ddot{y}_c}{\ddot{z}_c + g} + \frac{\dot{\mathcal{L}}_x}{m_c \ddot{z}_c + m_c g}. \tag{2.4}$$

By making the assumptions that the vertical acceleration of the CoM and the time derivative of the angular momentum are zero, the 3D LIP model arises. The last assumption implies two possibilities: 1) the total mass of the robot is constrained in one point; 2) the total angular momentum around the CoM is constant (this choice could restrict the motion of the CoM, that is why it is not often used). Thus, by using these assumptions in equations (2.3) and (2.4) we have

$$p_x = x_c - \frac{z_c \ddot{x}_c}{g}, \tag{2.5}$$

$$p_y = y_c - \frac{z_c \ddot{y}_c}{g}. \tag{2.6}$$

From these equations, the 3D LIP model proposed by Kajita [1] is obtained, which is given by

$$\ddot{x}_c = \frac{g}{z_c}(x - p_x), \tag{2.7}$$

$$\ddot{y}_c = \frac{g}{z_c}(y - p_y). \tag{2.8}$$

The 3D LIP model is often used to study walking gaits due to the fact it captures some essential properties of walking, such as the limit of the ZMP and the effect of gravity. This model is composed of two linear differential equations of second order that allow to define the evolution of the CoM when the position of the CoP is known. Moreover, its dynamics in the sagittal plane is decoupled from those in the frontal plane.

In order to explore simultaneously the dynamic characteristics of periodic orbits for many step lengths and widths, a dimensionless dynamic model of the pendulum will

be used. The normalized scaling factors applied along the x and y axes depend on the desired step length S and desired step width D. Thus, a new set of variables is defined as: $[X, Y, z_c, X_s, Y_s, z_s]^\top = [\frac{x_c}{S}, \frac{y_c}{D}, z_c, \frac{x_s}{S}, \frac{y_s}{D}, z_s]^\top$, where $[x_s, y_s, z_s]^\top$ represent the swing foot positions along x, y and z axes.

For a 3D LIP model with $p_x = 0; p_y = 0$, the equations of motion for a normalized 3D LIP with respect to the reference frame attached to the stance foot are:

$$\begin{aligned} \ddot{X} &= \omega^2 X, \\ \ddot{Y} &= \omega^2 Y, \end{aligned} \tag{2.9}$$

where $\omega = \sqrt{\frac{g}{z_c}}$ characterizes the LIP and varies with the height of the CoM. As the legs of the robot are assumed to be massless, the swing leg motions X_s, Y_s, z_s do not affect the equation of dynamics of the 3D LIP. The solution to this system is [1]:

$$\begin{aligned} X(t) &= X^+ \cosh(\omega t) + \frac{\dot{X}^+}{\omega} \sinh(\omega t), \\ Y(t) &= Y^+ \cosh(\omega t) + \frac{\dot{Y}^+}{\omega} \sinh(\omega t), \\ \dot{X}(t) &= \omega X^+ \sinh(\omega t) + \dot{X}^+ \cosh(\omega t), \\ \dot{Y}(t) &= \omega Y^+ \sinh(\omega t) + \dot{Y}^+ \cosh(\omega t), \end{aligned} \tag{2.10}$$

where X^+ and Y^+ denote the initial position of the CoM in x direction and y direction respectively during the SS phase, while $\dot{X}^+$ and $\dot{Y}^+$ denote the initial velocity of it.

The orbital energies [83]:

$$\begin{aligned} E_x &= \dot{X}^2 - \omega^2 X^2, \\ E_y &= \dot{Y}^2 - \omega^2 Y^2, \end{aligned} \tag{2.11}$$

and the synchronization measure

$$L = \dot{X}\dot{Y} - \omega^2 XY \tag{2.12}$$

are conserved during a SS phase [7]. We can say that the solution in one step is synchronized if and only if the synchronization measure is zero. The notion of self-synchronization refers to the periods of the pendular motions in the sagittal and frontal planes tending to a common period. In fact, this condition $L(X, Y, \dot{X}, \dot{Y}) = 0$ defines a one-dimensional submanifold. Any solution starting from this submanifold is synchronized and leads to periodic motion.

2.2.3 Transition between steps.

Due to the hypothesis that the contact between the swing foot and the ground does not affect the velocity of the CoM, the velocity of CoM will be conserved at each transition of stance leg. Since the reference frame is always attached to the stance foot and the y axis is directed toward the CoM, the sign of the velocity along y axis will be changed from positive to negative [78], i.e.

$$\begin{aligned} \dot{X}_{k+1}^{+} &= \dot{X}_{k}^{-}, \\ \dot{Y}_{k+1}^{+} &= -\dot{Y}_{k}^{-}. \end{aligned} \tag{2.13}$$

The state before the transition, i.e. at the end of a step, is expressed by superscript $^{-}$ and that after the transition, i.e. at the beginning of a step, is expressed by $^{+}$. The variables corresponding to the step k, are denoted with index k, while those of the next step are denoted with $k+1$.

After transition, the swing foot placement becomes the new stance foot placement. Thus the CoM position after transition along x axis equals the CoM position before transition minus the swing foot position. Similar result can be obtained for the CoM position along y axis:

$$\begin{aligned} X_{k+1}^{+} &= X_{k}^{-} - X_{s,k}^{-}, \\ Y_{k+1}^{+} &= -Y_{k}^{-} + Y_{s,k}^{-}. \end{aligned} \tag{2.14}$$

Knowing the final state of the SS phase, the transition models (2.13) and (2.14) determine the initial state of the ensuing SS phase.

2.2.4 Hybrid model.

An overall model of walking is obtained by combining the model in SS phase and the transition model to form a hybrid system. The transition is assumed to occur when the swing foot touches the ground, i.e. the height of the swing foot z_s is zero. A switching manifold is defined below:

$$\mathscr{S} := \{\mathbf{x} | z_s = 0, \dot{z}_s < 0\}, \tag{2.15}$$

where $\mathbf{x} := [X, Y, \dot{X}, \dot{Y}]^{\top}$ is the state of the robot. The transition models (2.13) and (2.14) can be rewritten as:

$$\mathbf{x}^{+} = \Delta_{lip}(\mathbf{x}^{-}), \tag{2.16}$$

where Δ_{lip} indicates the transition map of the LIP model.

Assuming a perfect tracking of the desired evolution of joints, a reduced order system,

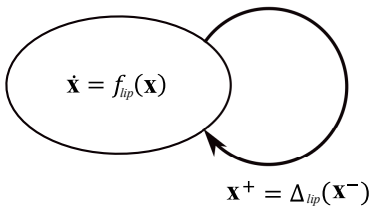

Figure 2.2 – The hybrid model of walking

called hybrid zero dynamics (HZD) can be obtained combining the dynamic equations (2.9) and the transition model (2.16):

$$\Sigma_{lip} : \begin{cases} \dot{\mathbf{x}} = f_{lip}(\mathbf{x}), & \mathbf{x}^- \notin \mathscr{S} \\ \mathbf{x}^+ = \Delta_{lip}(\mathbf{x}^-), & \mathbf{x}^- \in \mathscr{S} \end{cases} \tag{2.17}$$

A representation of the resulting model as a simple hybrid system is shown in Figure 2.2.

2.2.5 Periodic motion.

For a normalized system, periodic symmetric motion varies from

$$[X^{*+}; Y^{*+}] = [-\frac{1}{2}; \frac{1}{2}] \tag{2.18}$$

to

$$[X^{*-}; Y^{*-}] = [\frac{1}{2}; \frac{1}{2}], \tag{2.19}$$

where the superscript $*$ denotes the periodic motion. Since the orbital energy [83] is conserved during one step, the norm of the velocity at the beginning and end of a step is conserved, while the sign of it along y axis is changed due to the change of reference frame:

$$\begin{aligned} \dot{X}^{*-} &= \dot{X}^{*+}, \\ \dot{Y}^{*-} &= -\dot{Y}^{*+}. \end{aligned} \tag{2.20}$$

Thus, the initial velocity of the CoM for a periodic motion with duration T can be pointed out by solving equation (2.9):

$$\begin{aligned} \dot{X}^{*+} &= \omega \frac{1 + \cosh(\omega T)}{2 \sinh(\omega T)}, \\ \dot{Y}^{*+} &= \omega \frac{1 - \cosh(\omega T)}{2 \sinh(\omega T)}. \end{aligned} \tag{2.21}$$

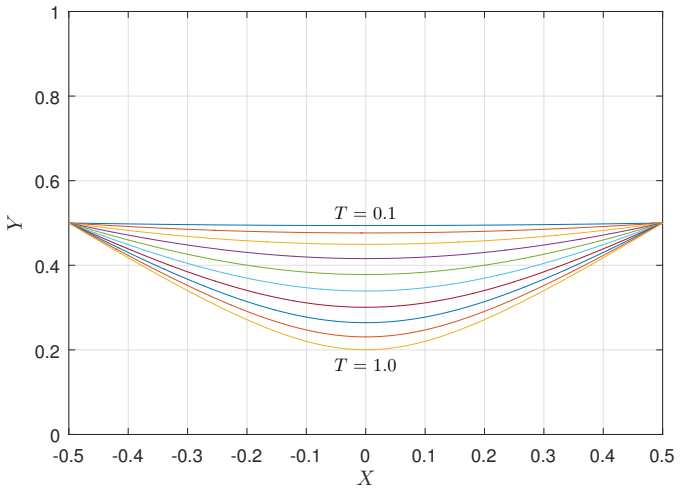

Figure 2.3 – Periodic motions in normalized variables for several values of T.

In normalized variables, the cyclic motion for different values of step duration T is presented in Figure 2.3. We characterize the orientation of the velocity at the end of the SS phase by

$$\alpha = \frac{\dot{Y}^{*-}}{\dot{X}^{*-}} = -\frac{\dot{Y}^{*+}}{\dot{X}^{*+}}. \tag{2.22}$$

For a periodic motion in normalized coordinates, $0 < \alpha < 1$.

2.3 The swing foot motion

In order to consider the general case, a normalized variable Φ monotonically increasing from 0 to 1 during one step, named phasing variable is defined to describe the desired trajectory of the controlled variables. For the case when transition is based on time, Φ is time normalized with respect to the desired step duration. And for the case when transition is based on the CoM position, Φ is a function of X and Y. The trajectories of the swing foot are defined as functions of Φ: $X_s = X_s(\Phi)$, $Y_s = Y_s(\Phi)$, $z_s = z_s(\Phi)$. The vertical evolution of the swing foot determines the condition of transition between steps, while the horizontal evolution determines the foot locations. The advantage of introducing a phasing variable is that this method can be extended to a complete model of robots by using the phasing variable to coordinate all the joint motions of the robot.

2.3.1 The vertical swing foot motion.

An intermediate value of the phasing variable $0 < \Phi_m < 1$ is defined, so that when $\Phi = \Phi_m$, $h_s = \max_{0<\Phi<1}\{z_s\}$. For the vertical motion of swing foot, the boundary conditions are:

$$\begin{aligned} z_s(0) = 0, \quad z_s(\Phi_m) = h_s, \quad z_s(1) = 0, \\ \dot{z}_s(0) = 0, \quad \dot{z}_s(\Phi_m) = 0, \quad \dot{z}_s(1) = v_s, \end{aligned} \tag{2.23}$$

where h_s is the desired height of the swing foot when $\Phi = \Phi_m$, and $v_s < 0$ denotes the desired downward velocity of the swing foot at the end of a step. In this chapter, $z_s(\Phi)$ is defined as a cubic spline function, which allows us to control both the height of the swing foot and its velocity.

$$z_s = \begin{cases} p_{11}\Phi^3 + p_{12}\Phi^2 + p_{13}\Phi + p_{14}, \ 0 \le \Phi < \Phi_m \\ p_{21}\Phi^3 + p_{22}\Phi^2 + p_{23}\Phi + p_{24}, \ \Phi_m \le \Phi \le 1 \end{cases} \tag{2.24}$$

where

$$\begin{aligned} p_{11} &= -\frac{2{h_s}^3}{\Phi_m}, p_{12} = \frac{3{h_s}^2}{\Phi_m}, p_{13} = p_{14} = 0, \\ p_{21} &= \frac{v_s - v_s\Phi_m + 2h_s}{(-1+\Phi_m)^3}, \\ p_{22} &= \frac{v_s(1+\Phi_m - 2\Phi_m^2) + 3(1+\Phi_m)h_s}{(-1+\Phi_m)^3}, \\ p_{23} &= \frac{\Phi_m(v_s(-2+\Phi_m+\Phi_m^2) - 6h_s)}{(-1+\Phi_m)^3}, \\ p_{24} &= \frac{-v_s(-1+\Phi_m)\Phi_m^2 + (-1+3\Phi_m)h_s}{(-1+\Phi_m)^3}. \end{aligned} \tag{2.25}$$

By using the cubic spline function, the swing foot will keep moving downward even when the ground is uneven. When Φ is bigger than one, the height of the swing foot is negative, as shown in Figure 2.4.

2.3.2 The horizontal swing foot motion.

The position where the swing foot lands must be chosen cautiously. In order to analyze several cases, the swing foot positions at the end of step k is expressed in a generalized form:

$$\begin{aligned} X_{s,k}^- &= (1-k_S)(X_k^- - X^{*-}) + 1, \\ Y_{s,k}^- &= (1-k_D)(Y_k^- - Y^{*-}) + 1, \end{aligned} \tag{2.26}$$

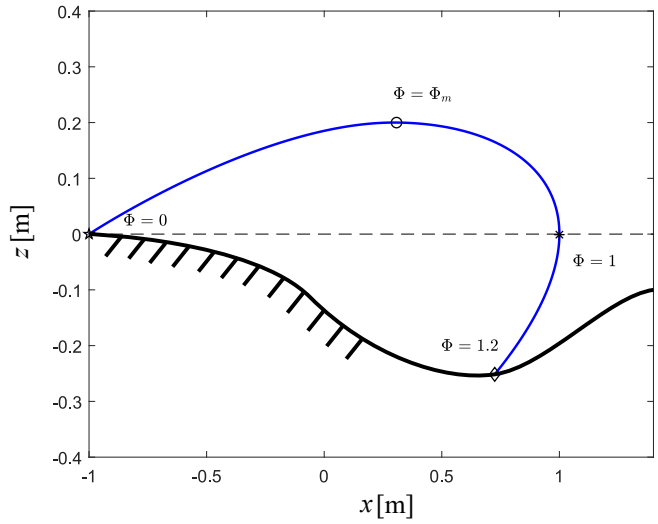

Figure 2.4 – The trajectory of the swing foot in sagittal plane is represented by the blue curve, and the black curve represents an uneven ground. In this figure, $\Phi_m = 0.6, h_s = 0.2$ m is taken as an example.

where $0 \leq k_S \leq 1$ and $0 \leq k_D \leq 1$. How the parameters k_S and k_D affect the foot locations is illustrated in Figure 2.5. The case $k_S = k_D = 0$ allows to nullify the CoM position error at the beginning of the next step, i.e.

$$\begin{aligned} \delta X^+_{k+1} = &\quad X^+_{k+1} - X^{*+} = 0, \\ \delta Y^+_{k+1} = &\quad Y^+_{k+1} - Y^{*+} = 0, \end{aligned} \tag{2.27}$$

while the case $k_S = k_D = 1$ corresponds to fixed step length and width.

The boundary conditions for the motion of the swing foot along x and y directions are:

$$\begin{aligned} X_s(0) = X^+_{s,k}, &\quad \dot{X}_s(0) = 0, \\ X_s(1) = X^-_{s,k}, &\quad \dot{X}_s(1) = 0, \\ Y_s(0) = Y^+_{s,k}, &\quad \dot{Y}_s(0) = 0, \\ Y_s(1) = Y^-_{s,k}, &\quad \dot{Y}_s(1) = 0, \end{aligned} \tag{2.28}$$

where $X^+_{s,k}$ and $Y^+_{s,k}$ are the swing foot positions at the beginning of step k, which can be known according to the information of the previous step. Since the swing leg is massless and the impact is not considered, the velocities of the swing foot after transition is zero. The horizontal velocities of the swing foot at the end of a step is taken to be zero to avoid

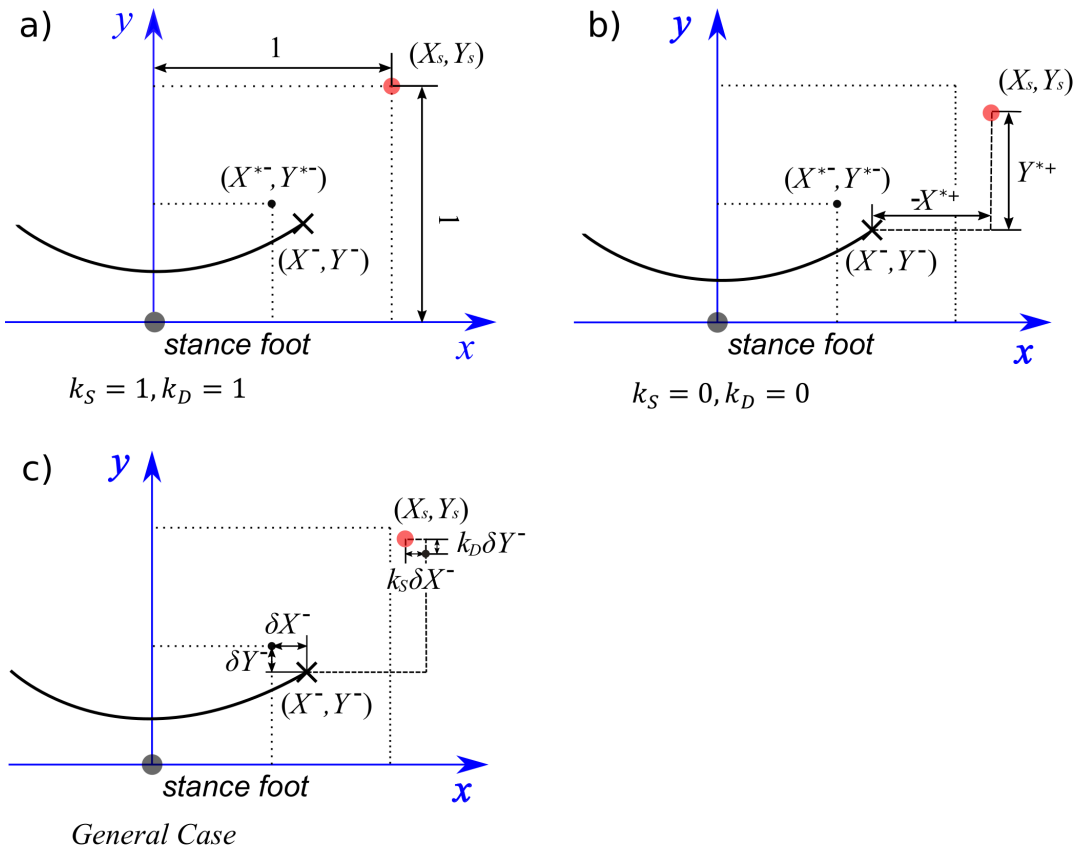

Figure 2.5 – Influence of k_S and k_D on the foot locations. a) Step length and width are fixed; b) The initial CoM position error is nullified; c) The general case. The black and the red dots represent respectively the stance feet during the current and the next steps. The curved line represents the CoM trajectory, and the cross the CoM position at the end of the current step.

the possible slide. For the case when the initial error is nullified:

$$\begin{aligned} X_{s,k}^{+} &= -(X_{k-1}^{-} + 0.5), \quad X_{s,k}^{-} = \quad X_{k}^{-} + 0.5, \\ Y_{s,k}^{+} &= Y_{k-1}^{-} + 0.5, \qquad\quad Y_{s,k}^{-} = \quad Y_{k}^{-} + 0.5. \end{aligned} \tag{2.29}$$

For the case when the stride is imposed at a fixed step size:

$$\begin{aligned} X_{s,k}^{+} &= -1, \quad X_{s,k}^{-} = 1, \\ Y_{s,k}^{+} &= 1, \qquad Y_{s,k}^{-} = 1. \end{aligned} \tag{2.30}$$

According to these boundary conditions, the trajectory in x and y directions can be defined as 3^{rd} order polynomial functions of Φ.

$$\begin{aligned} X_s &= -2(X_{s,k}^{-} - X_{s,k}^{+})\Phi^3 + 3(X_{s,k}^{-} - X_{s,k}^{+})\Phi^2 + X_{s,k}^{+}, \\ Y_s &= -2(Y_{s,k}^{-} - Y_{s,k}^{+})\Phi^3 + 3(Y_{s,k}^{-} - Y_{s,k}^{+})\Phi^2 + Y_{s,k}^{+}. \end{aligned} \tag{2.31}$$

2.4 The Poincaré return map

The classical technique for determining the existence and local stability properties of periodic orbits in nonlinear systems involves Poincaré return maps [84, 85], which is the intersection of a periodic orbit in the state space of a continuous dynamical system with a certain lower-dimensional subspace $\mathcal{S}$, called the Poincaré section, transversal to the flow of the system. The Poincaré return map transforms the problem of finding periodic orbits into one of finding fixed points of a map, which in turn can also be viewed as the problem of finding equilibrium points of a particular discrete-time nonlinear system. The method of Poincaré sections is rigorous: it provides necessary and sufficient conditions for the existence of stable, asymptotically stable, or exponentially stable periodic orbits [6]. The difficulty is that it is almost impossible to determine the return map analytically for a typical system, because it requires the closed-form solution of a nonlinear ordinary differential equation. Numerical schemes can be used to find fixed points of the return map and to estimate eigenvalues for determining exponential stability.

Usually for a bipedal locomotion system, the Poincaré section is defined just before the impact with the ground. The impact map yields new initial conditions for the swing phase differential equation when the switching manifold $\mathscr{S}$ is reached. Assume $\mathbf{x}^* \in \mathcal{S}$ is a state vector for a periodic motion of the hybrid system. $\mathbf{x}(0)$ is an initial state of the system in the neighbourhood of $\mathbf{x}^*$. The state of the system starts from $\mathbf{x}(0)$, follows the

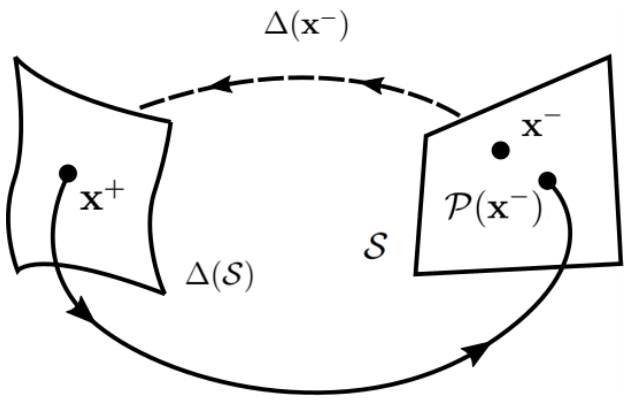

Figure 2.6 – The Poincaré return map

dynamic function, and intersects with the Poincaré section $\mathcal{S}$ again. The state at the k^{th} intersection with $\mathcal{S}$ is noted as $\mathbf{x}(k)$. Thus the Poincaré return map $\mathcal{P} : \mathcal{S} \mapsto \mathcal{S}$ (shown in Figure 2.6) is defined as:

$$\mathbf{x}(k+1) = \mathcal{P}(\mathbf{x}(k)). \tag{2.32}$$

A limit cycle corresponds to a fixed point of the Poincaré return map, i.e.

$$\mathbf{x}^* = \mathcal{P}(\mathbf{x}^*). \tag{2.33}$$

In the general case the Poincaré first return map is linearized around the fixed point by means of Taylor expansion,

$$\begin{aligned} \mathcal{P}(\mathbf{x}^* + \delta\mathbf{x}) &= \mathcal{P}(\mathbf{x}^*) + \frac{\mathrm{d}\mathcal{P}}{\mathrm{d}\mathbf{x}}(\mathbf{x}^*)\delta\mathbf{x} \\ &= \mathcal{P}(\mathbf{x}^*) + J(\mathbf{x}^*)\delta\mathbf{x}. \end{aligned} \tag{2.34}$$

Thus, for $\mathbf{x} = \mathbf{x}^* + \delta\mathbf{x}$, we have:

$$\mathbf{x}(k+1) - \mathbf{x}^* = \mathcal{P}(\mathbf{x}^* + \delta\mathbf{x}) - \mathbf{x}^* = J(\mathbf{x}^*)\delta\mathbf{x}. \tag{2.35}$$

Equations (2.34) and (2.35) formalize the fact that at step k the distance between $\mathbf{x}$ and the fixed point is $\delta\mathbf{x}$, then at step $k+1$ the distance will be $J(\mathbf{x}^*)\delta\mathbf{x}$. In order to ensure stability, the distance of the system state and the fixed point has to decrease, i.e. the norm of the eigenvalues of the Jacobian $J(\mathbf{x}^*)$ is strictly less than one.

One way to compute the fixed point is to find the numerical solution of (2.33). After the fixed point $\mathbf{x}^*$ is obtained, the Jacobian of the Poincaré first return map can be computed by add a perturbation e_i on the fixed point as below:

$$J_i = \frac{\mathcal{P}(\mathbf{x}^* + e_i) - \mathcal{P}(\mathbf{x}^* - e_i)}{2e_i}, \tag{2.36}$$

where i denotes the i^{th} column of the Jacobian.

The eigenvalues of J determine the stability of the Poincaré map $\mathcal{P}$, and hence the stability of the periodic motion. A fixed point of the Poincaré map is exponentially stable, if, and only if, the eigenvalues of J have magnitude strictly less than one [58].

2.5 Transition based on time

In this section, the phasing variable is defined as $\Phi = \frac{t}{T^*}$, where T^* is the desired step duration. With this phasing variable, the step timing of each step is strictly $T = T^*$. The control is assumed to be perfect so that the reference trajectories of the swing foot X_s, Y_s and z_s can be tracked precisely.

2.5.1 Stability study.

The Jacobian matrix of the Poincaré return map at the fixed point is calculated numerically in the state space $[X_k^-, Y_k^-, L_k^-, K_k^-]^\top$, where L_k^- is the synchronization measure defined by equation (2.12) and K_k^- is the kinetic energy at the end of step k.

The eigenvalues of several cases for different values of k_D and k_S have been studied, and two extreme cases $k_S = k_D = 0$ and $k_S = k_D = 1$ among them are illustrated in Figure 2.7. It can be seen clearly that for both cases, there always is more than one eigenvalue larger than or equal to one, which means that for the transition based on time, stability of walking is not obtained without using a high-level controller.

2.5.2 Simulation

One example of simulation for $k_S = k_D = 0$ starting slightly out of the periodic motion is analyzed here. The step length S and step width D are 0.4 m and 0.2 m respectively, and the height of the CoM z is 1 m. The desired step duration is set to be 0.6 s. Disturbance imposed on the initial state for the simulation is taken as $e_x = 10^{-3}$ m, $e_y = 10^{-3}$ m. The

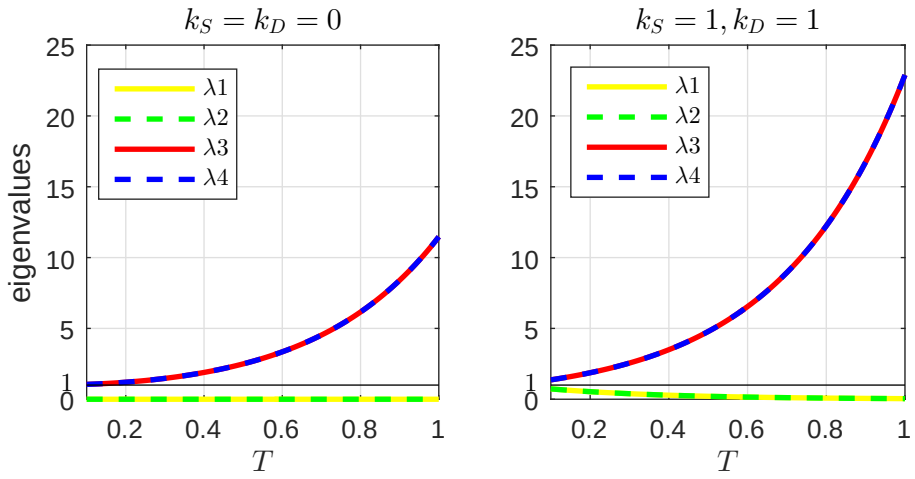

Figure 2.7 – Values of the four eigenvalues for different step durations T when transition is based on time.

eigenvalues calculated for the linearized restricted Poincaré map are:

$$\begin{aligned} |\lambda_1| &= |\lambda_2| = 0, \\ |\lambda_3| &= |\lambda_4| = 2.497. \end{aligned} \tag{2.37}$$

The stance foot position and the CoM evolution for both periodic and disturbed motions are illustrated in Figure 2.8, while the state evolutions are illustrated in Figure 2.9. The periodic motion is represented with the black curves and lines while the disturbed motion represented with the blue curves and lines in Figures 2.8 and 2.9. It can be seen clearly that the CoM position diverges quickly when disturbances exist. In this case, the effect of instability is that the walking is not along the expected path (here along x axis) but the direction of walking is perturbed along right or left direction depending on the perturbation. This kind of motion is often observed on the humanoid robots as Nao for example.

In consequence, this kind of control is not naturally synchronized and a high-level control must be added to produce a synchronized or stable walking gait. In the following sections, we will prove that by defining proper virtual constraints and a phasing variable depending on the state of the robot, self-synchronization and self-stabilization of the walking gait can be obtained.

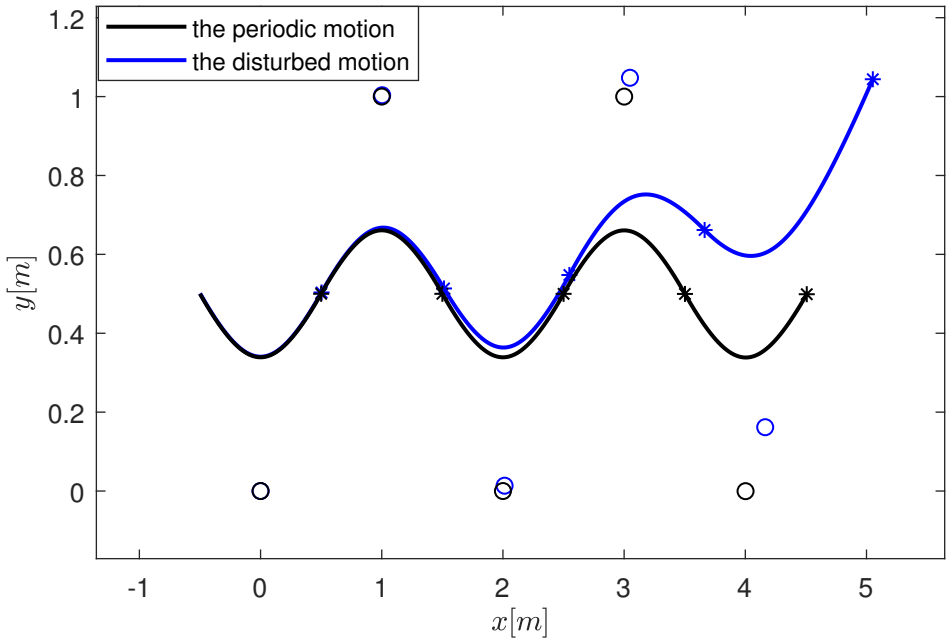

Figure 2.8 – Evolution of CoM of the LIP model when transition is based on time with $k_S = k_D = 0$ for 5 steps. The black and blue circles represent the stance feet and the asterisks the CoM positions at the end of each step.

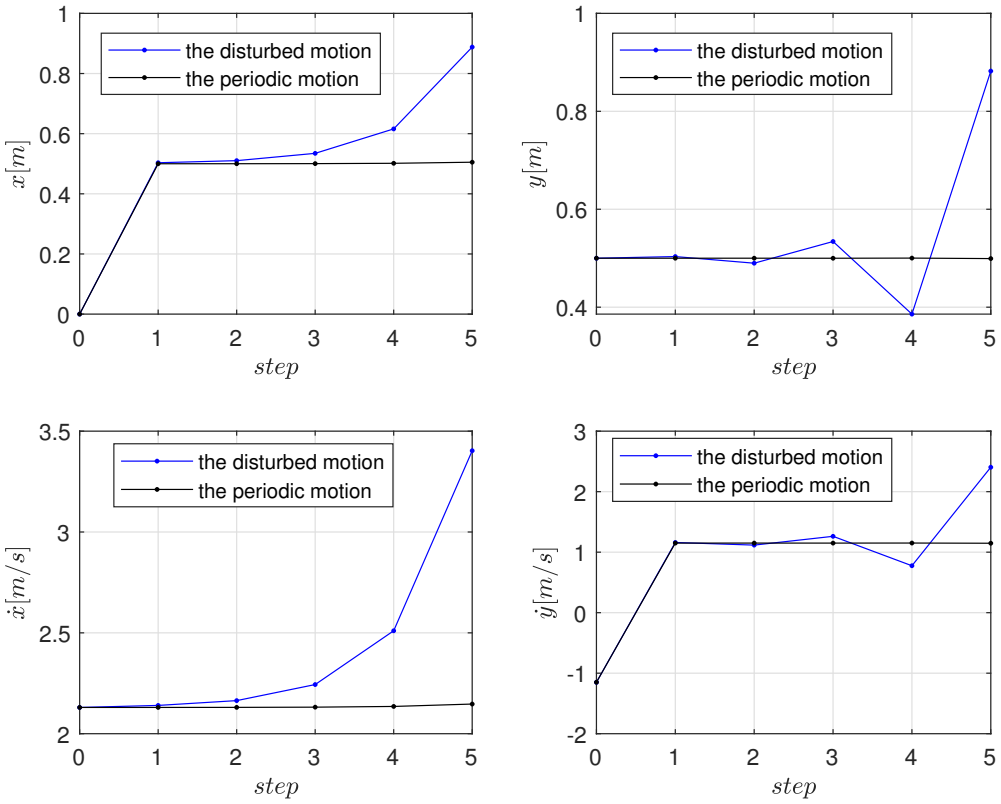

Figure 2.9 – Evolution of the states of the LIP model when transition is based on time for $k_S = k_D = 0$ for 5 steps.

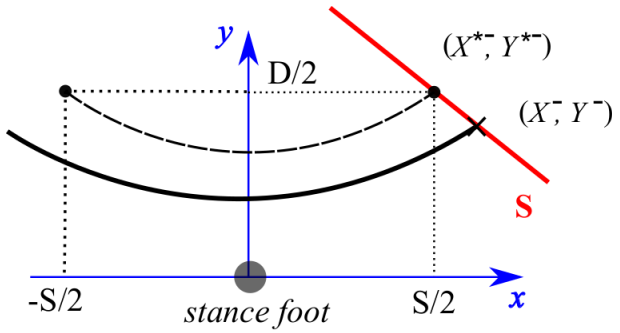

Figure 2.10 – The step finishes when the CoM crosses the switching manifold. The dashed line is the periodic motion of the CoM, and the solid line the CoM motion under an initial position perturbation.

2.6 Transition based on the horizontal CoM position

2.6.1 The virtual constraints

The vertical trajectory of the swing foot is defined as a function of a phasing variable based on the horizontal CoM position $\Phi(X, Y)$. The transition happens when the swing foot touches the ground, which defines a relationship between the two variables X and Y. An infinite number of CoM positions satisfy it. This set of positions are grouped in the switching configuration manifold defined by:

$$\mathbb{S} = \{(X, Y) | z_s(\Phi) = 0\}. \tag{2.38}$$

There will be infinite sets of positions of the CoM that satisfy this condition. In this chapter, we choose a phasing variable such that the robot switches its stance leg when the CoM crosses the switching manifold defined by

$$\mathbf{S} = \{(X, Y) | (X - X^{*-}) + C(Y - Y^{*-}) = 0\}. \tag{2.39}$$

The switching manifold **S** is defined as a line parameterized by C, represented by the red line in Figure 2.10. Many other sets of positions can be considered but since stability studied here is a local property, a straight line is a convenient choice. The choice of **S** directly affects the final CoM position for a step.

2.6.2 The phasing variable

In presence of error, the final CoM position of the robot is defined by equation (2.39), i.e the error on the final position of the CoM satisfies:

$$\delta X^- + C\delta Y^- = 0 \tag{2.40}$$

where δX^- and δY^- are the CoM position errors along x and y axes at the end of a step.

If Φ is expressed as a linear expression of X and Y, no monotonic evolution of Φ has been found numerically for a periodic gait of the 3D LIP. Therefore, a quadratic expression of X and Y is proposed, i.e.

$$\Phi = a_1 X + a_2 Y + a_3 XY + a_4 X^2 + a_5 Y^2 + a_6. \tag{2.41}$$

Since the phasing variable must be zero at the beginning of a step, we have

$$\Phi(X^+, Y^+) = 0, \tag{2.42}$$

where X^+ and Y^+ are known from equation (2.14). Besides, in order to make the switching manifold (2.38) and (2.39) equivalent, the phasing variable at the end of a step should equal one:

$$\Phi(X^-, Y^-) = 1. \tag{2.43}$$

In order to simplify the writing, δ is used here to replace δY^-, thus we have $X^- = X^{*-} - C\delta, Y^- = Y^{*-} + \delta$ according to equation (2.40). The expression of Φ at the end of a step can be written as a function of δ:

$$\begin{aligned}
\Phi(X^-, Y^-) =& a_1(X^{*-} - C\delta) + a_2(Y^{*-} + \delta) + a_3(X^{*-} - C\delta)(Y^{*-} + \delta) \\
&+ a_4(X^{*-} - C\delta)^2 + a_5(Y^{*-} + \delta)^2 + a_6 \\
=& (a_1 X^{*-} + a_2 Y^{*-} + a_3 X^{*-} Y^{*-} + a_4 (X^{*-})^2 + a_5 (Y^{*-})^2 + a_6) \\
&+ (-a_3 C + a_4 C^2 + a_5)\delta^2 \\
&+ (-a_1 C + a_2 - a_3 C Y^{*-} + a_3 X^{*-} - 2a_4 C X^{*-} + 2a_5 Y^{*-})\delta
\end{aligned} \tag{2.44}$$

Since all the above constraints given by equations (2.42) and (2.43) must be satisfied

for an arbitrary value of δ, three more equations can be obtained and we have:

$$\begin{cases} a_1X^+ + a_2Y^+ + a_3X^+Y^+ + a_4(X^+)^2 + a_5(Y^+)^2 + a_6 = 0, \\ a_1X^{*-} + a_2Y^{*-} + a_3X^{*-}Y^{*-} + a_4(X^{*-})^2 + a_5(Y^{*-})^2 + a_6 = 1, \\ -a_3C + a_4C^2 + a_5 = 0, \\ -a_1C + a_2 - a_3CY^{*-} + a_3X^{*-} - 2a_4CX^{*-} + 2a_5Y^{*-} = 0. \end{cases} \tag{2.45}$$

There are six variables $\{a_1, a_2, a_3, a_4, a_5, a_6\}$ while the number of equations is only four. For simplification, the value of a_3 is set to be 0, thus Φ is expressed as a function of a_4. After calculation, the phasing variable can be rearranged as:

$$\Phi = \frac{M_1}{M_2} + a_4M_3M_4 \tag{2.46}$$

$$\begin{aligned} M_1 &= X - X^+ + CY - CY^+ \\ M_2 &= X^{*-} - X^+ + CY^{*-} - CY^+ \\ M_3 &= X - X^{*-} + CY - CY^{*-} \\ M_4 &= X - X^+ - CY + CY^+. \end{aligned} \tag{2.47}$$

During a step, the phasing variable must be monotonic and increasing, thus the derivative of Φ with respect to time should always be positive.

$$\dot{\Phi} = a_1\dot{X} + a_2\dot{Y} + 2a_4X\dot{X} + 2a_5Y\dot{Y} > 0 \tag{2.48}$$

Monotonicity of Φ for the periodic motion, i.e. when $X^+ = X^{*+}, Y^+ = Y^{*+}$, is analyzed. A set of a_4 varying from -0.3 to -0.6 is chosen to satisfy the condition of monotonicity. The minimum values of $\dot{\Phi}$ for different values of C, T and a_4 are shown in Figure 2.11. Obviously, when the minimum value of $\dot{\Phi}$ is larger than zero, Φ is monotonically increasing. From the result shown in Figure 2.11, $a_4 = -0.4$ is taken for the following simulation because it allows a larger range of acceptable values of C with respect to different values of T.

2.6.3 Stability study.

To study the stability of the walking gait, the Poincaré return map is used. Since X^- and Y^- are coupled via the switching manifold (2.39), and the dynamic is autonomous

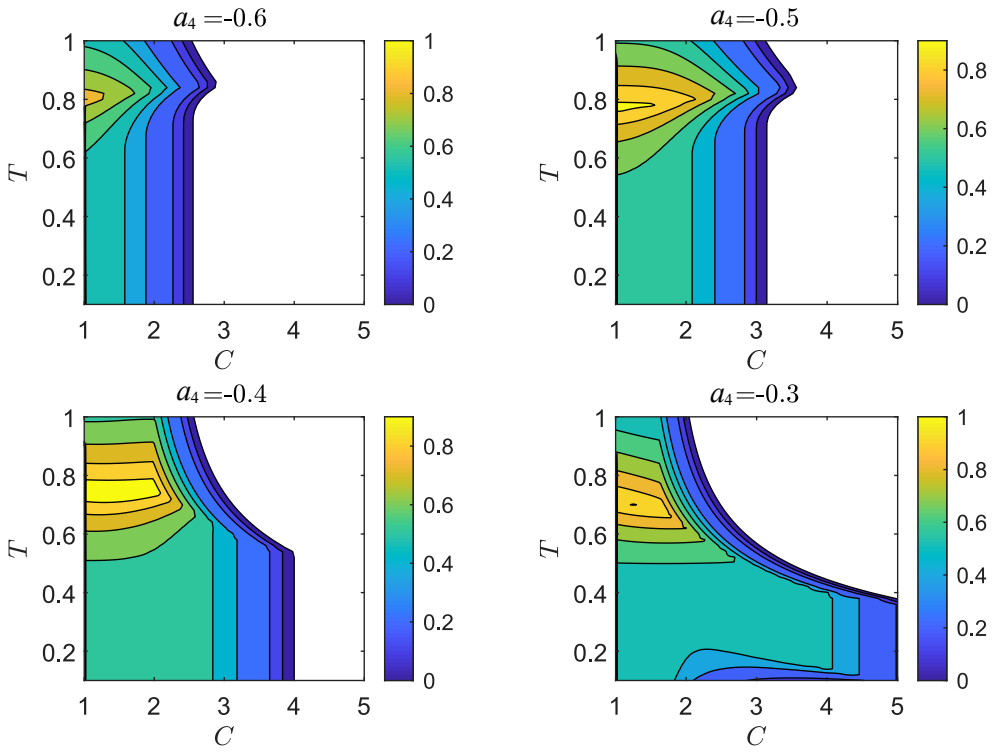

Figure 2.11 – The minimum value of $\dot{\Phi}$ as a function of C and T for different a_4. The colored areas, with respect to the white areas, indicate that the phasing variable is monotonic.

(time does not appear), Y^- can be deleted and the chosen independent state variables are $[X^-, L^-, K^-]^\top$. The Jacobian is defined for a given periodic motion, and is characterized by the direction of the velocity of the CoM α (as defined by equation (2.22)).

For the 3D LIP model, the eigenvalues of the Poincaré map at the fixed points are $\{\boldsymbol{\lambda}, 1\}$, where $\boldsymbol{\lambda}$ is the set of eigenvalues except for the one respect to kinetic energy. The eigenvalue 1 corresponds to neutral stability in kinetic energy. And if $\forall|\lambda_i| \in \boldsymbol{\lambda} < 1$, the symmetric periodic orbits are self-synchronized. This means that the period of oscillations in the x direction eventually matches that in the y direction, and the 3D LIP biped follows a periodic orbit. That is, if a small perturbation is applied to the 3D LIP, it will still become synchronized but will eventually follow a periodic orbit with a different level of kinetic energy.

General case: $\forall k_D, k_S \neq 0$

The expression of the Jacobian matrix of Poincaré return map in an analytical form can be deduced as follows (The procedure is detailed in Appendix A):

$$J = \begin{bmatrix} -\frac{k_D+\alpha C k_S}{(k_S+\alpha C)} & \frac{4\alpha C k_S}{\omega^2(1+\alpha C)(\alpha-1)} & 0 \\ J_{21} & \frac{2\alpha(k_D-Ck_S)+(1-\alpha C)(\alpha+1)}{(1+\alpha C)(\alpha-1)} & 0 \\ * & * & 1 \end{bmatrix}, \tag{2.49}$$

with

$$J_{21} = \frac{(k_D + \alpha C k_S)(C - 1 + Ck_S - k_D)\omega^2}{2(1 + \alpha C)Ck_S}. \tag{2.50}$$

Note that this calculation is general except for the case when $k_S = 0$. The characteristic equation of J does not depend on the two elements denoted by $*$. The eigenvalue associated with K^- is always 1, and this means that the walking velocity cannot be controlled. It is possible to find a proper set of parameters C, k_S and k_D to achieve self-synchronization. A numerical calculation of the largest norm of the eigenvalues associated to the 2×2 left-upper part of (2.49), for different values of k_D and k_S is shown in Figure 2.12. The main conclusion is that when k_D and k_S decrease, the norm of the eigenvalues is smaller for an appropriate choice of C, for any $T \in (0, 1]$s.

Particular case: $k_D = k_S = 0$

To nullify the error in pose for the CoM at the beginning of a step, k_D and k_S are supposed to be zero. Thus the Jacobian becomes

$$J = \begin{bmatrix} 0 & 0 & 0 \\ \frac{\alpha(-1+C)\omega^2}{2(1+\alpha C)} & \frac{(-1+\alpha C)(\alpha+1)}{(1+\alpha C)(1-\alpha)} & 0 \\ * & * & 1 \end{bmatrix} \tag{2.51}$$

It has to be noted that with the proposed control strategy (the initial error in position of CoM is null), the decrease of synchronization measure, at the first order, is independent of the direction of the velocity error.

The eigenvalues are $\lambda_1 = 0$, $\lambda_3 = 1$ and $\lambda_2 = \frac{(-1+\alpha C)(\alpha+1)}{(1+\alpha C)(1-\alpha)}$. The term $\frac{(1+\alpha)}{(1-\alpha)}$ is always greater than 1 for $0 < \alpha < 1$, its diverging effect increases when α increases. A condition on C to have synchronization can be easily deduced to meet the condition:

$$-1 < \frac{(-1+\alpha C)(\alpha+1)}{(1+\alpha C)(1-\alpha)} < 1 \tag{2.52}$$

which gives:

$$1 < C < \frac{1}{\alpha^2} \tag{2.53}$$

The condition $\lambda_2 < 1$ ensures convergence toward a synchronized motion, thus is a condition of self-synchronization. The case $k_S = k_D = 0$ is especially interesting since the eigenvalues of the Jacobian matrix can be very small for an appropriate choice of C. This case has been explored in [75]. One drawback of this choice is the lateral error that can appear on the walking path due to the variation of the step width to nullify the error along y direction.

Particular case: $k_D = k_S = 1$

In this case, the Jacobian matrix (2.49) becomes

$$J = \begin{bmatrix} -1 & \frac{4\alpha C}{\omega^2(1+\alpha C)(\alpha-1)} & 0 \\ \frac{(C-1)\omega^2}{C} & \frac{2\alpha(1-C)+(1-\alpha C)(\alpha+1)}{(1+\alpha C)(\alpha-1)} & 0 \\ * & * & 1 \end{bmatrix} \tag{2.54}$$

The eigenvalues of the Jacobian matrix are

$$\lambda_1, \lambda_2 = \frac{(1+\alpha)(1-\alpha C) \pm 2\sqrt{\alpha(C-1)(\alpha^2 C-1)}}{(1+\alpha C)(\alpha-1)} \qquad (2.55)$$
$$\lambda_3 = 1$$

When $\alpha(C-1)(\alpha^2 C-1) < 0$, it can be proven that all the norms of the eigenvalues are strictly equal to 1. In the other case at least one eigenvalue has a norm greater than 1. In both cases, no self-synchronization can be achieved.

Particular case : $k_D \leq 1$**,** $k_S = 0$

In this case, the error in x direction at the beginning of a step is nullified, there is no connection between X_k and X_{k+1}. The previous choice of Poincaré map cannot be applied in this case. Instead of $[X^-, L^-, K^-]^\top$, new coordinate system $[Y^-, L^-, K^-]^\top$ is chosen to be the coordinate system, and the Jacobian matrix needs to be calculated specifically:

$$J = \begin{bmatrix} -\frac{k_D(\omega^2+\alpha\omega^2)}{(-1+\alpha)(1+\alpha C)\omega^2} & \frac{4\alpha k_D}{(-1+\alpha)(1+\alpha C)\omega^2} & 0 \\ \frac{(-1+C-k_D)\omega^2}{2+2\alpha C} & \frac{1+\alpha-\alpha(1+\alpha)C+2\alpha k_D}{(1+\alpha C)(\alpha-1)} & 0 \\ * & * & 1 \end{bmatrix}. \qquad (2.56)$$

In the following part of this chapter, $k_S = 0, k_D = 1$ will be chosen, because $k_S = 0$ can contribute to achieve self-synchronization while $k_D = 1$ can prevent the robot from deviating from its original direction.

2.6.4 Choice of C.

The manifold of C and T that makes the walking gait self-synchronized is defined as

$$\mathcal{Q}_{syn} := \{(C,T) | \lambda_{1,2}(C,T) < 1, \lambda_3(C,T) = 1\}. \qquad (2.57)$$

Meanwhile, the manifold of C and T that makes the phasing variable Φ monotonic for the periodic gait is defined as

$$\mathcal{M} := \{(C,T) | \min_{0 \leq t \leq T} \{\dot{\Phi}(C,T)\} > 0\}. \qquad (2.58)$$

Thus, in order to accomplish a step, the values of C and T must be located inside of

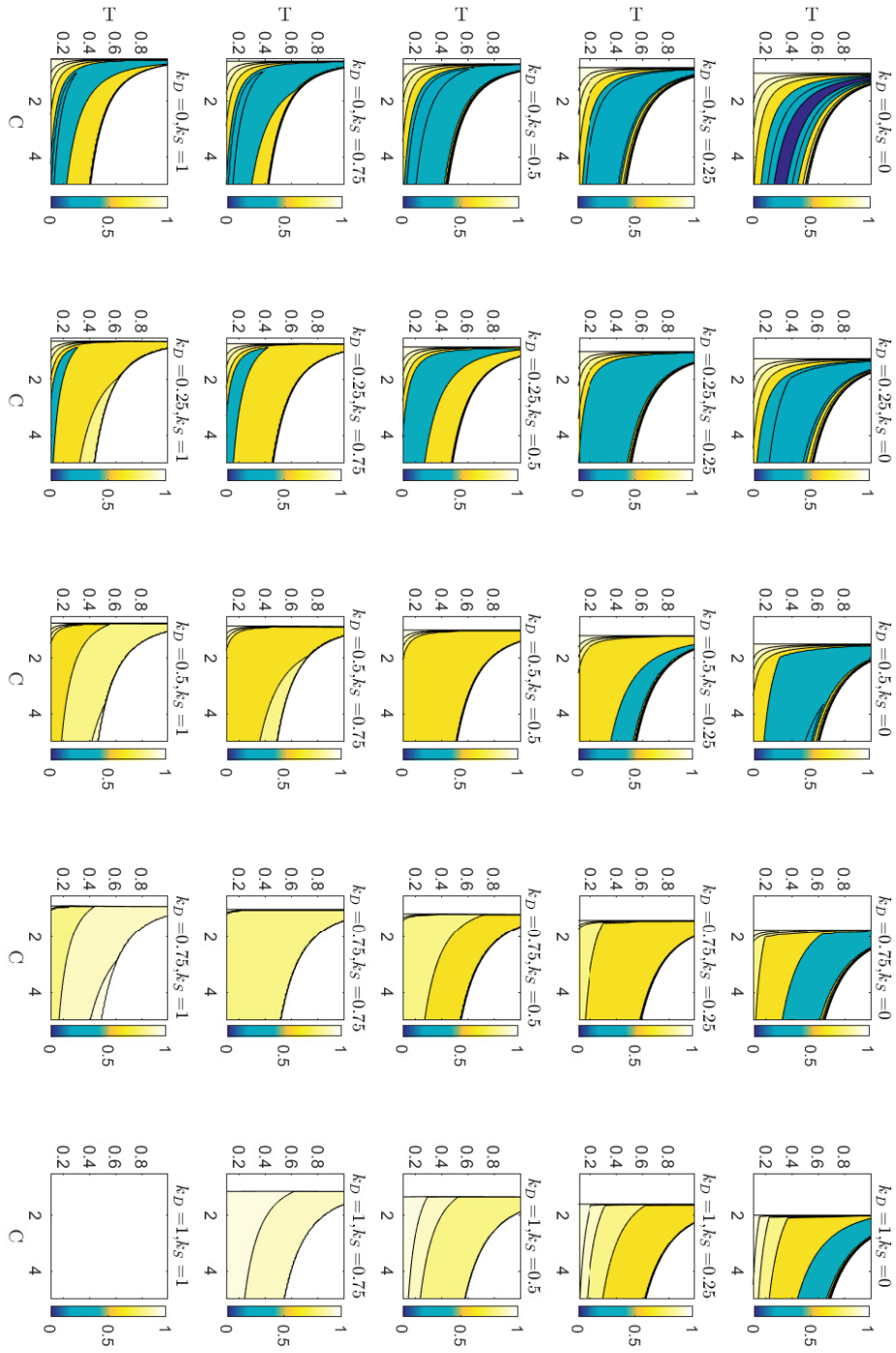

Figure 2.12 – Numerical calculation of the largest norm of the eigenvalues associated to the 2×2 left-upper part of (2.49) and (2.56), for different values of k_D and k_S

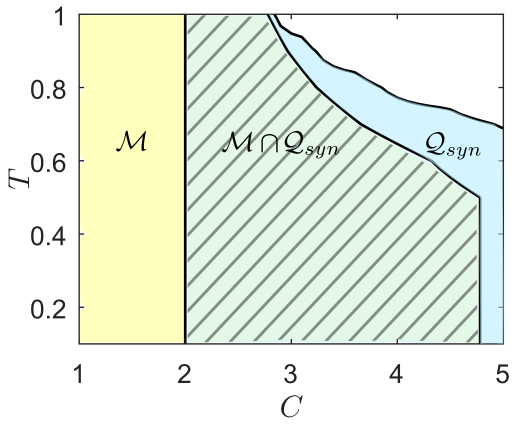

Figure 2.13 – Intersection of $\mathcal{Q}_{syn}$ and $\mathcal{M}$ for $k_S = 0, k_D = 1$

the intersection of $\mathcal{Q}_{syn}$ and $\mathcal{M}$, i.e. $(C, T) \in \mathcal{Q}_{syn} \cap \mathcal{M}$. Figure 2.13 shows the acceptable values of C and T for $k_S = 0, k_D = 1$.

2.6.5 Simulation

The step length S and step width D are 0.4 m and 0.2 m respectively, and the height of the CoM z_c is 1 m. The desired step duration is 0.6 s. According to Figure 2.13, the chosen value of C is 3. Note that C is defined for normalized step length and width. The proper value of C for real step length and width is proportional to the ratio of S and D, i.e. $C' = C \cdot \frac{S}{D}$. The walking algorithm proposed by Kajita in [1] is integrated in the simulation for the first and the last steps and is not explained in detail in this work, because it does not affect the self-synchronization or self-stabilization of the periodic motion.

Figure 2.14a shows the evolution of the CoM and the footprints for 15 steps, and the convergence to a periodic gait motion is observed. However, the actual step duration T does not converge to the desired one T^*, as shown in Figure 2.14b. It means that the walking velocity of the gait is not controlled in the sense that a perturbation of such a gait will result in the convergence of the gait to another periodic motion with a different gait velocity. At the first and the last steps, the step duration is 0.6 s due to the application of the walking algorithm proposed by Kajita. In Figure 2.15, the states of the CoM in the Poincaré section converge to constant values but not the fixed values, which means that the walking gait is self-synchronized but not self-stabilized.

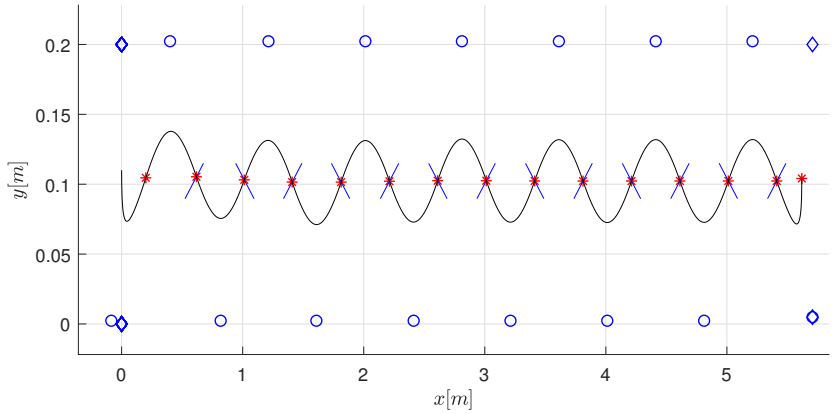

(a) Evolution of the CoM

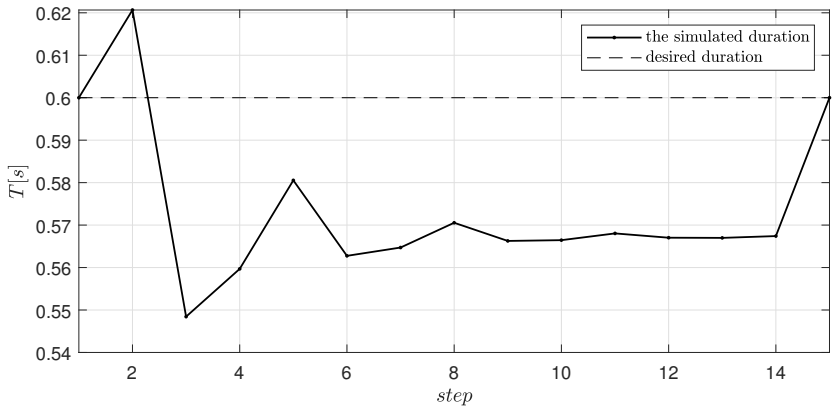

(b) Evolution of T

Figure 2.14 – 15 steps for the 3D LIP model when transition is based on the CoM position. The blue lines in (a) represent the switching manifolds, the blue dots and diamonds the stance feet during the SS phase, and starting and stopping phases, and the red asterisks the CoM positions at the end of each step.

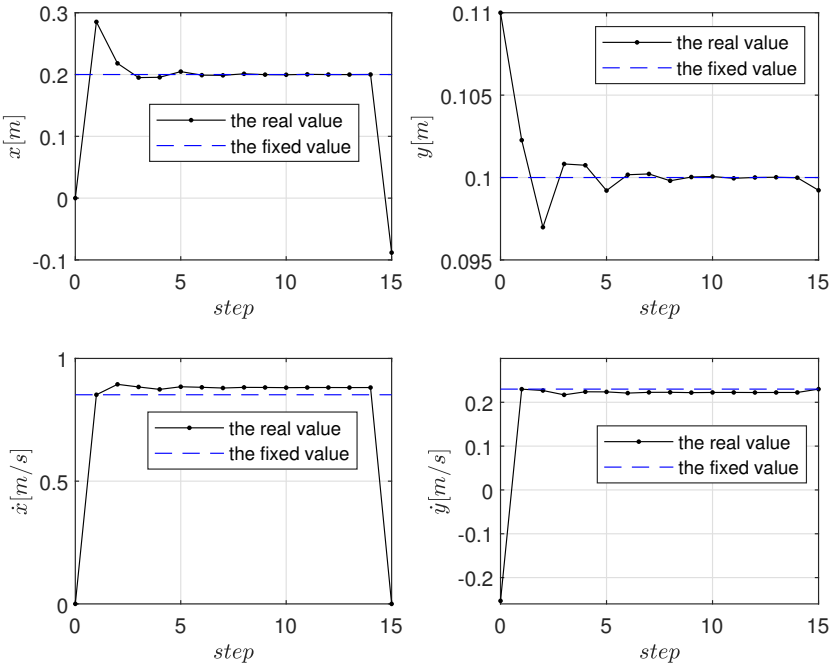

Figure 2.15 – Evolution of the states of the CoM when transition is based on the CoM position

2.7 Transition based on the CoM position and velocity feedback

For a self-synchronized walking gait, a perturbation on the state of the robot may cause a change of the walking velocity. Thus in order to control the walking velocity of the 3D LIP, a new method that leads to self-stabilization is proposed in this section.

2.7.1 The virtual constraints

The feedback of the velocity of CoM is introduced into the switching condition of the stance leg, and a new switching manifold is proposed:

$$\mathbf{S_v} = \{(X, Y) | (X - X^{*-} - l) + C(Y - Y^{*-}) = 0\} \tag{2.59}$$

As shown in Figure 2.16, the new switching manifold is a line with an offset l from the switching condition proposed in last section. The offset is defined as $l = k_v(\dot{X}^{*+} - \dot{X}^{+})$, where $\dot{X}^{+}$ is the velocity of the CoM along x axis at the beginning of a step, which is updated at each step [3], and k_v is a parameter that must be chosen carefully to satisfy the stability condition.

2.7.2 The phasing variable

With the CoM velocity feedback along x axis, the CoM position at the end of a step is modified, i.e. $X^{-} = X^{*-} - C\delta + l, Y^{-} = Y^{*-} + \delta$. Thus the phasing variable Φ can be deduced by applying X^{-} and Y^{-} into $\Phi(X^{-}, Y^{-}) = 1$:

$$\Phi = \frac{M_1 + a_4 M_2 M_3 M_4 - a_4 M_4 l + a_4 (M_3 - M_2) M_4 l^2}{M_2 + l}. \tag{2.60}$$

By adjusting the position of the switching manifold, the difference between the current velocity and the desired velocity along x direction can be controlled to obtain self-stabilization.

3. The correction can be based on the mean value of velocity during the previous step to increase robustness to the measurement noise

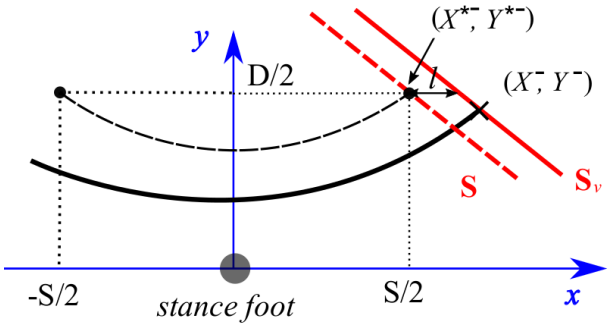

Figure 2.16 – The new switching condition is an offset from the one proposed in last section. The dashed line is the periodic motion, while the solid line is the CoM motion under an initial position perturbation.

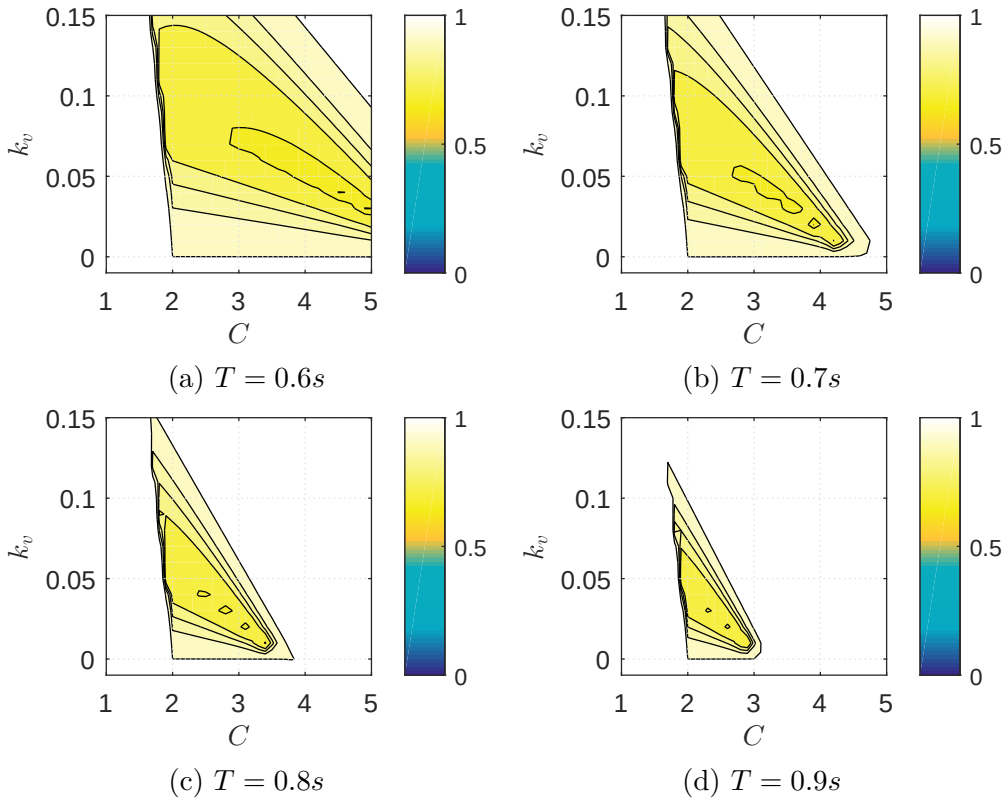

(a) $T = 0.6s$ (b) $T = 0.7s$

(c) $T = 0.8s$ (d) $T = 0.9s$

Figure 2.17 – The maximum norms of the eigenvalue as a function of C and k_v for different values of T. The colored areas, with respect to the white areas, indicate the self-stabilization condition.

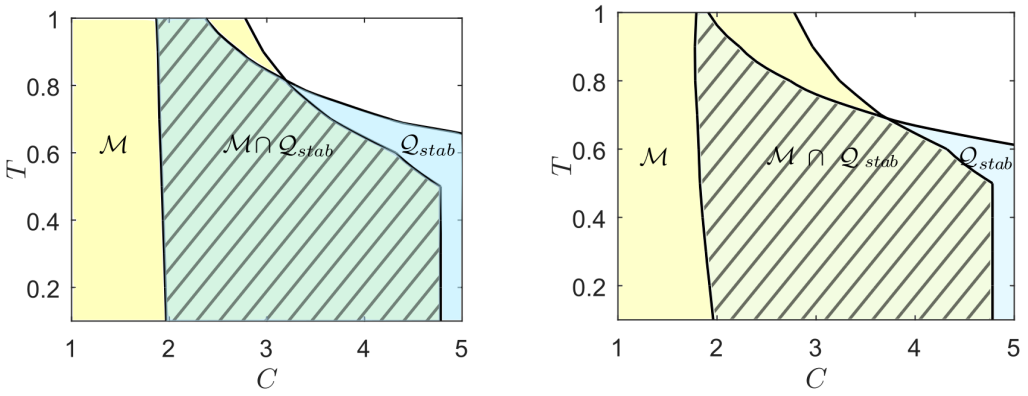

(a) $k_v = 0.04$ (b) $k_v = 0.08$

Figure 2.18 – Intersections of $\mathcal{Q}_{stab}$ and $\mathcal{M}$ that keep Φ monotonic and produces a stable walking gait for $k_v = 0.04$ and $k_v = 0.08$ respectively

2.7.3 Stability study

With this new phasing variable, the stability of the gait is analyzed through the numerical calculation of the eigenvalues of the Jacobian matrix for different values of C, k_v and T. The contour of the maximum norm of the eigenvalues is shown in Figure 2.17. It can be seen that when both the values of C and k_v are located inside the colored area, all the norms of the eigenvalues will be smaller than one. Under this situation, the self-stabilization of the system can be obtained. Whereas in the white area at least one eigenvalue is larger than one.

2.7.4 Choice of C.

In order to make the walking gait stable, the manifold of C and T is defined as:

$$\mathcal{Q}_{stab} := \{(C, T) | \lambda_i < 1 (i = 1, \cdots, n)\}, \tag{2.61}$$

where n is the number of eigenvalues. Considering the fact that C and T must also satisfy the constraint that Φ is monotonic, the values of C and T must be located inside of the intersection of $\mathcal{Q}_{stab}$ and $\mathcal{M}$, i.e. $(C, T) \in \mathcal{Q}_{stab} \cap \mathcal{M}$. Figures 2.18a and 2.18b show the acceptable values of C and T for $k_S = 0, k_D = 1$ when $k_v = 0.04$ and $k_v = 0.08$ respectively.

2.7.5 Simulation

The step length S and step width D are 0.4 m and 0.2 m respectively, and the height of the CoM z_c is 1 m. From the result shown in Figure 2.18, $C = 3$ is chosen. Based on the result shown in Figure 2.17, $k_v = 0.08$ when $T^* = 0.6$ s, and $k_v = 0.04$ when $T^* = 0.8$ s to ensure stability.

The same method proposed by Kajita as that in Section 2.6.3 is adopted for the first and last step. The desired step duration T^* is increased from 0.6 s to 0.8 s at the 15^{th} step, in order to show the convergence of the walking gait in velocity.

Figure 2.19a illustrates the evolution of the CoM and the placement of feet. Due to the increase of step duration, the amplitude of the motion of the CoM along y direction increases obviously after 15 steps. And Figure 2.19b indicates that the actual step duration T starts from 0.6 s, and increases to 0.8 s after 15 steps. In Figure 2.20, it can be seen that the introduction of the displacement l plays an important role during the motion. It permits that the velocity along x axis converges to a desired value, i.e. self-stabilization is obtained. Note that when an increase of step duration is expected, only $\dot{x}$ is constrained, and $\dot{y}$ converges automatically to a value that corresponds to the periodic motion determined by $\dot{x}$ with the proposed walking algorithm.

2.8 Robustness of walking on an uneven ground

In order to test the robustness of the walking gait, the humanoid robot is lead to an uneven ground after several steps of walking on a flat ground, and then back to the flat ground again. The variation of the height of the ground is unknown to the robot, thus it will follow the predetermined trajectory proposed in the previous sections until the swing foot touches the ground. A sinusoidal ground is considered:

$$z_G(x_G) = h_G \cos(\omega_G x_G) \tag{2.62}$$

where h_G denotes the magnitude of the sinusoidal ground and ω_G characterizes the frequency of the ground variation.

The simulation of a pendulum walking on a sinusoidal ground is given in this section. The magnitude of the sinusoidal ground $h_G = 0.035$ m, and the frequency $\omega_G = 2\pi$ is taken as an example. The height of the pendulum $z_c = 1$ m, the step length and width $S = 0.4$ m, $D = 0.2$ m. The ground and the pendulum are demonstrated in Figure 2.21.

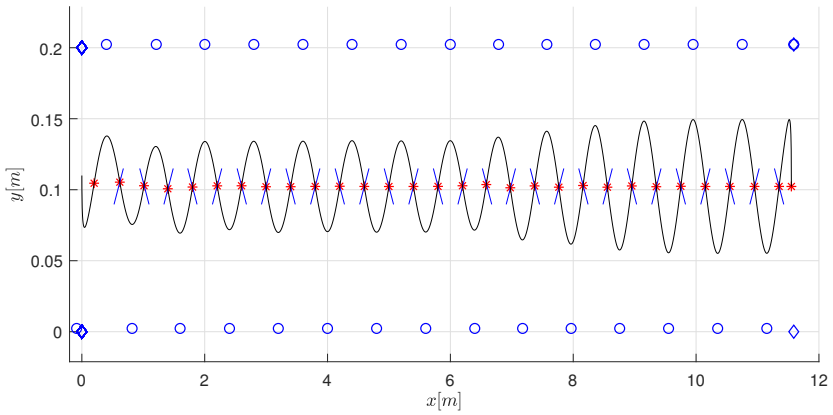

(a) Evolution of the CoM

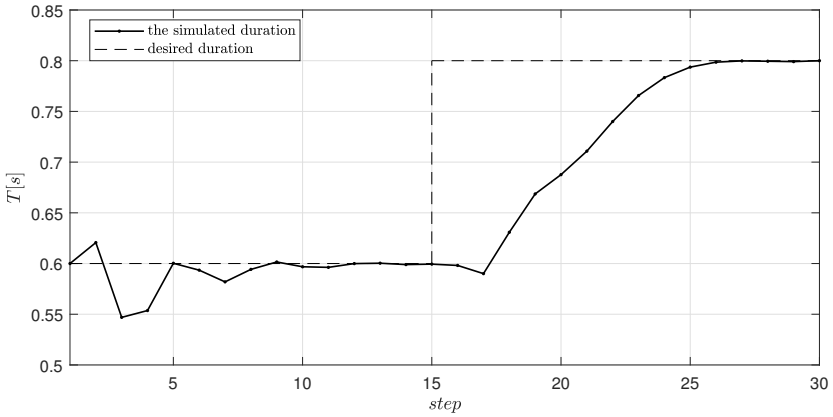

(b) Evolution of T

Figure 2.19 – Simulation of 30 steps for the LIP model when transition is based on the CoM position and velocity. The blue lines in figure (a) represent the switching manifolds, the blue dots and diamonds the stance feet during the SS phase, and starting and stopping phases, and the red asterisks the CoM positions at the end of each step.

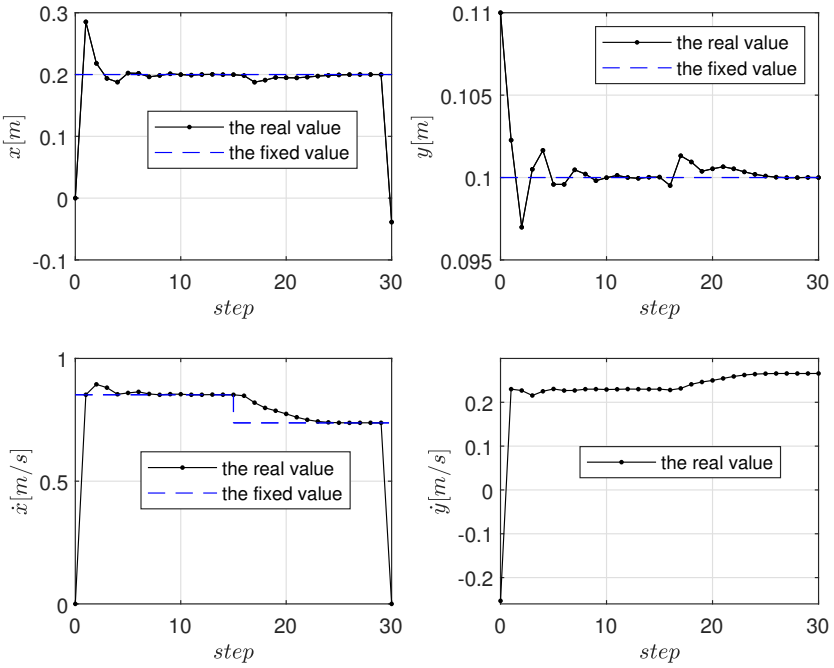

Figure 2.20 – Evolution of the states of the 3D LIP during 30 steps when transition is based on the CoM position and velocity. The fixed value is shown with the dash line.

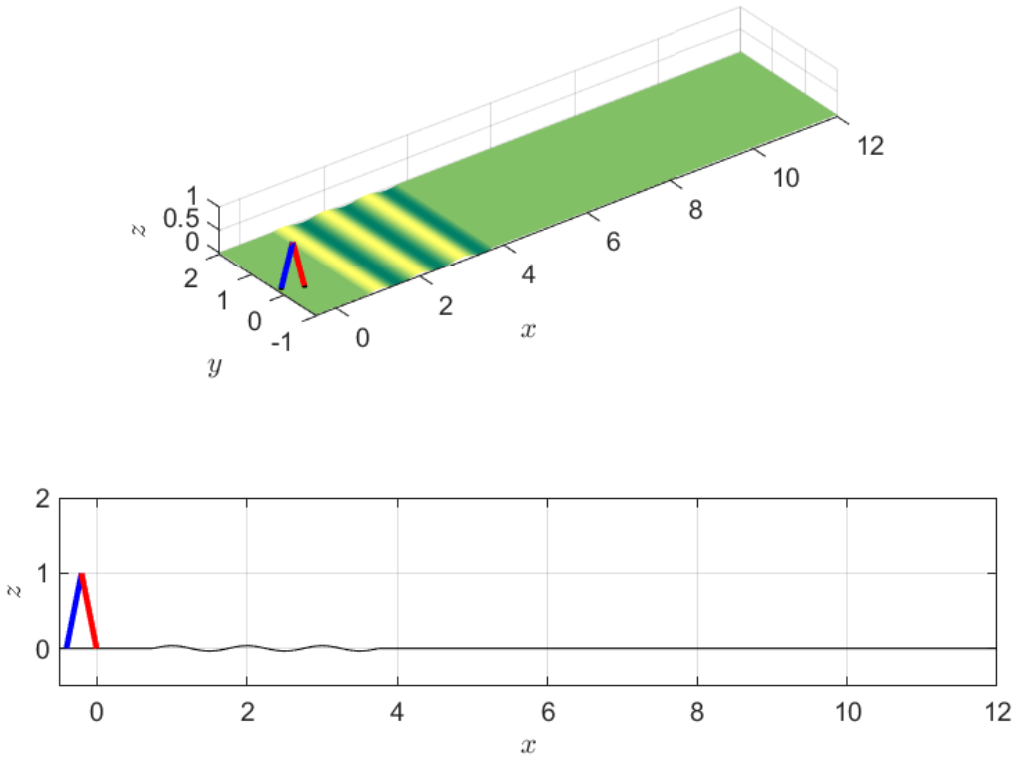

Figure 2.21 – Demonstration of a pendulum walking on a sinusoidal ground.

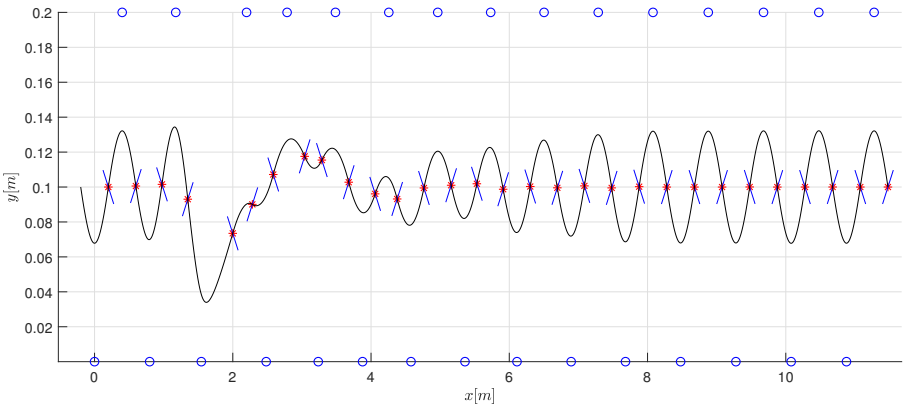

(a) Evolution of the CoM

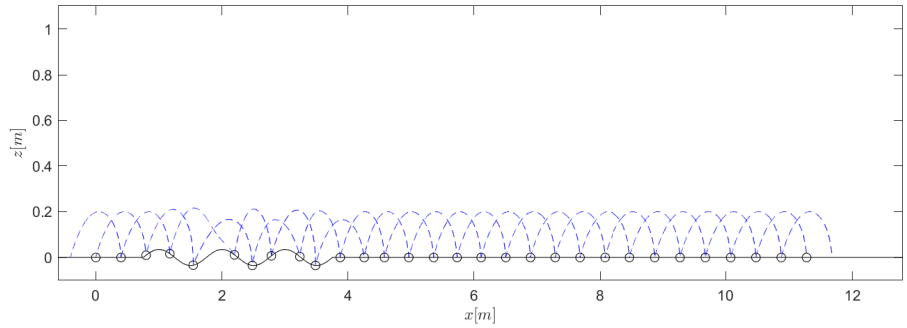

(b) Evolution of the swing foot

Figure 2.22 – Simulation of 30 steps for the pendulum walking on a sinusoidal ground. The dashed lines in subfigure (b) illustrate the trajectories of the swing foot, while the circles illustrate the stance foot of each step.

For a step timing $T^* = 0.6$ s, the parameters of the switching condition are $C = 3$, $k_v = 0.1$ to ensure stability. To consider the case with a fixed step width as an example, $k_D = 1$ is taken. The initial CoM position error along x axis is nullified to ensure stability. In the simulation, 30 steps are performed.

It can be seen from Figure 2.22a that CoM trajectory is perturbed when the pendulum walks on the sinusoidal ground, and converges to the periodic motion when it returns to the flat ground. Figure 2.22b illustrates the trajectories of the swing foot and positions of the stance foot for each step. The stance leg is switched as soon as the swing foot touches the ground. The trajectory proposed in Section 2.3.1 makes sures that the swing foot keeps going downward even when the ground is below the expected height. Figure 2.23 shows that the states of the system converge asymptotically to the periodic values,

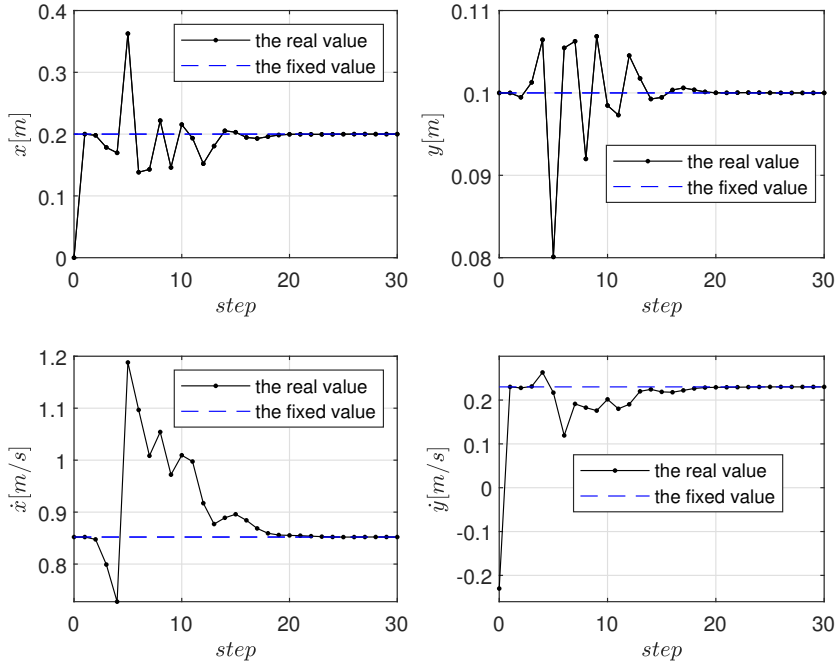

Figure 2.23 – Evolution of the states of the system.

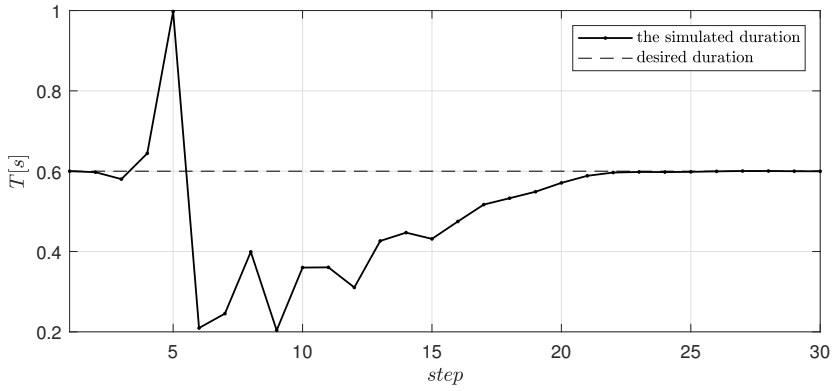

Figure 2.24 – Evolution of the step timing.

and Figure 2.24 shows that the step timing has a big variation to resist the perturbation, and converges to the expected value within serval steps after the perturbation disappears. The result shows that robustness can be observed when the robot walks on a non-flat floor with a height varying from -3.5% to $+3.5\%$ limited of the height of the CoM. The video showing this motion can be found on line [86]. For the case with $k_S = k_D = 0$, can could increase the magnitude of the sinusoidal ground to $\pm 4.2\%$.

2.9 Conclusion

In this chapter, the switching conditions for obtaining self-synchronization or self-stabilization for the periodic walking gait based on LIP model are discussed. It has been proven that self-synchronization cannot be achieved when the stance foot is switched based on time or when both the step length and width are fixed. In this case, synchronization and stabilization of walking gaits can be achieved only by using high-level control techniques. Thus this chapter proposes to define the switching condition based on the CoM position to achieve self-synchronization. This condition is expressed as a linear function of the CoM position in a switching manifold parameterized by a parameter denoted by C. It is shown that for an appropriate value of C, if the swing foot placement is chosen such that the initial CoM position error is reduced step by step at least in one direction, synchronization of the walking can be naturally obtained. Furthermore, it has been proven that the introduction of the CoM velocity feedback into the phasing variable permits to achieve self-stabilization of walking gaits. The last part of this chapter has shown that the robustness of a pendulum walking on an even ground can be obtained with the proposed walking algorithm.

Chapter 3

Self-stability of the 3D VLIP model

3.1 Introduction

In human walk, the height of the CoM is not constant [87], and the vertical oscillation of the CoM must be considered. Lee and Farley [88] observed that during walking the maximum vertical displacement increases from 0.013 ± 0.001 m (mean±S.E.M.) for a walking speed 0.5 m/s to 0.031 ± 0.007 m for a walking speed 2.5 m/s. Several approaches have been proposed to extend the LIP to have a more human-like behavior. Omran *et al.* [89] investigated the effect of vertical motion of the CoM during humanoid walking. Numerical tests show a consequent reduction of the robot torque solicitation when the CoM oscillates vertically. Garofalo *et al.* [90] mapped the simple dynamics of the bipedal spring loaded inverted pendulum (SLIP) model to multi-body robots to obtain a desired behavior for the CoM, yet an upper level controller is necessary to deal with the stabilization of the SLIP model. Harada *et al.* [91] captured the walking motion of a human, and applied the obtained information on real humanoid robot. Here the 3D variable length inverted pendulum (VLIP) model is used, which allows to control the vertical oscillations of CoM by the actuation of hip and knee joints. It has been proven by Chevallereau and Aoustin [10] that the vertical oscillation induces a self-stabilization of the walk for specific virtual constraints. The work in this chapter extends these preliminary results into a more systematic study of the virtual constraints by extending the results of self-synchronization obtained with a LIP model in Chapter 2. When the desired walking gait is defined as virtual constraints i.e. as functions of a phasing variable based on the internal state of the robot instead of on time, for the evolution of the swing foot and the vertical oscillation of the CoM, the walk will asymptotically converge to the periodic motion with proper choices of the virtual constraints, thus the self-stabilization is obtained. It is shown that the vertical CoM oscillation, positions of the swing foot and choice of the switching con-

dition play crucial roles in stability. Moreover, a proportional–integral (PI) controller of the CoM velocity along the sagittal axis is also proposed such that the walking speed of the robot can converge to another periodic motion with a different walking speed. This way, a natural walking gait is illustrated as well as the possibility of velocity adaptation as observed in human walking.

The chapter is structured as follows: Section 3.2 introduces the hybrid model of the VLIP; Section 3.3 introduces the virtual constraints and the phasing variable for the VLIP model; Section 3.4 introduces the cyclic motion of VLIP; Section 3.5 analyzes the stability of the VLIP model with the proposed switching conditions that leads to self-stabilization of the walking gait; Simulations illustrate the property of self-stabilization. Section 3.6 shows how a feedback on walking velocity can be used to adapt the periodic motion to a desired walking speed. Finally, several concluding remarks and perspectives are discussed in Section 3.7.

3.2 Modeling

The gait is composed of two phases: SS phase and DS phase. During the DS phase, the following hypotheses are recalled: 1) The double support phase is instantaneous; 2) Since the model is based on a concentrated mass, the contact between the swing foot and the ground does not modify the velocity of the CoM [40].

3.2.1 The 3D VLIP Model

During the SS phase, the 3D VLIP model is used. Compared with the 3D LIP model, the VLIP model is closer to the real human walking behavior, because the height of the CoM is not constant during walking.

The VLIP model consists of two massless legs with variable length and a concentrated mass at the hip, as shown in Figure 3.1. The stance leg is free to rotate about the axes x and y at the ground, while the rotation around the z axis is not considered as in the human walking because this rotation is avoided to inhibit the friction of the foot. The length of each leg can be modified through actuation, allowing a desired vertical motion of the pendulum to be obtained. We also assume that the actuation of the swing leg allows a controlled displacement of the swing leg end via the two degrees of actuation at the hip and knee actuators. There are four actuators, thus four variables can be controlled. In this

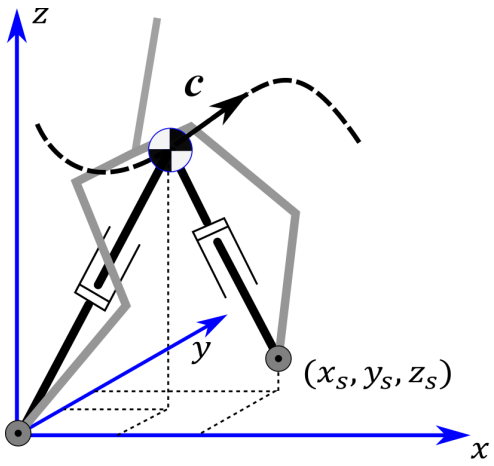

Figure 3.1 – The VLIP model.

chapter, the variables $[z_c, x_s, y_s, z_s]^\top$ i.e. the height of the CoM and the spatial position of the swing foot are chosen to be the controlled variables.

The configuration of the robot is defined via the position of the concentrated mass $\boldsymbol{c} = [x_c, y_c, z_c]^\top$ and the position of the swing foot $[x_s, y_s, z_s]^\top$ with respect to a reference frame attached to the stance foot. Since the legs are massless, the motion of the swing leg does not affect the dynamic model. Angular momenta is denoted by $\sigma = [\sigma_x, \sigma_y, \sigma_z]^\top$, and it can be expressed as:

$$\sigma = c \times (m\dot{c}), \tag{3.1}$$

thus

$$\begin{bmatrix} \sigma_x \\ \sigma_y \\ \sigma_z \end{bmatrix} = \begin{bmatrix} my\dot{z}_c - m\dot{y}_c z_c \\ mz\dot{x}_c - m\dot{z}_c x_c \\ mx\dot{y}_c - m\dot{x}_c y_c \end{bmatrix}. \tag{3.2}$$

The moment balance equation of the pendulum around the rotation axes x and y is:

$$\begin{cases} \dot{\sigma}_x = -mgy_c, \\ \dot{\sigma}_y = mgx_c. \end{cases} \tag{3.3}$$

In order to explore simultaneously the existence and stability of periodic orbits for robots with any step length and width, a dimensionless dynamic model is used [10]. The normalized scaling factors applied along x and y axes depend on the desired step length S, desired step width D, and the robot mass m. Thus, a new set of variables is defined: $[X, Y, z_c, X_s, Y_s, z_s, \sigma_X, \sigma_Y]^\top = [\frac{x_c}{S}, \frac{y_c}{D}, z_c, \frac{x_s}{S}, \frac{y_s}{D}, z_s, \frac{\sigma_x}{mD}, \frac{\sigma_y}{mS}]^\top$. Thus the normalized evolu-

tion of the angular momentum along x and y axes for a VLIP can be rewritten as:

$$\begin{cases} \sigma_X = \dot{z_c} Y - z_c \dot{Y}, \\ \sigma_Y = -\dot{z_c} X + z_c \dot{X}, \\ \dot{\sigma}_X = -gY, \\ \dot{\sigma}_Y = gX. \end{cases} \tag{3.4}$$

The controlled variables $[z_c, X_s, Y_s, z_s]^\top$ are determined by virtual constraints as functions of the phasing variable $\Phi(X, Y)$, where X and Y are defined as free variables or uncontrolled variables $q_f = (X, Y)$. The definition of the phasing variable will be discussed in detail in Section 3.3.2. The height of the CoM and its velocity can be expressed as:

$$\begin{aligned} z_c &= f_z(\Phi), \\ \dot{z_c} &= \frac{\partial f_z(\Phi)}{\partial \Phi}\left(\frac{\partial \Phi}{\partial X}\dot{X} + \frac{\partial \Phi}{\partial Y}\dot{Y}\right) = \frac{\partial f_z}{\partial X}\dot{X} + \frac{\partial f_z}{\partial Y}\dot{Y}. \end{aligned} \tag{3.5}$$

Assuming that the control law allows that the vertical motion of the CoM is perfectly tracked, equation (3.5) can be used to rewrite the zero dynamics [6] as :

$$\begin{cases} \dot{q}_f = M_{XY}^{-1} \cdot [\sigma_X; \sigma_Y]^\top, \\ \dot{\sigma}_X = -gY, \\ \dot{\sigma}_Y = gX, \end{cases} \tag{3.6}$$

where

$$M_{XY} = \begin{bmatrix} \frac{\partial f_z}{\partial X} Y & \frac{\partial f_z}{\partial Y} Y - f_z \\ f_z - \frac{\partial f_z}{\partial Y} Y & -\frac{\partial f_z}{\partial Y} X \end{bmatrix}. \tag{3.7}$$

3.2.2 Transition between steps

Due to the hypothesis of massless legs, the contact between the swing foot and the ground does not affect the velocity of the CoM, and the velocity of CoM is conserved at each transition of stance leg. Since the reference frame is always attached to the stance foot and the y axis is directed toward the CoM, the sign of the velocity along y axis will be

changed from positive to negative, i.e.

$$\begin{aligned} \dot{X}_{k+1}^{+} &= \dot{X}_{k}^{-}, \\ \dot{Y}_{k+1}^{+} &= -\dot{Y}_{k}^{-}, \\ \dot{z}_{c,k+1}^{+} &= \dot{z}_{c,k}^{-}. \end{aligned} \tag{3.8}$$

The state before the transition, i.e. at the end of a step, is expressed by superscript $^{-}$ and that after the transition, i.e. at the beginning of a step, is expressed by $^{+}$. The variables corresponding to the step k, are denoted with index k, while those of the next step are denoted with $k+1$.

After transition, the swing foot placement becomes the new stance foot placement, and the horizontal CoM position after the impact is given by:

$$\begin{aligned} X_{k+1}^{+} &= X_{k}^{-} - X_{s,k}^{-}, \\ Y_{k+1}^{+} &= -Y_{k}^{-} + Y_{s,k}^{-}, \\ z_{c,k+1}^{+} &= z_{c,k}^{+}. \end{aligned} \tag{3.9}$$

3.2.3 Hybrid model.

The transition occurs when the height of the swing foot z_s is zero. A switching manifold is defined below:

$$\mathscr{S} := \{\mathbf{x} | z_s = 0, \dot{z}_s < 0\} \tag{3.10}$$

where $\mathbf{x} := [X, Y, \dot{X}, \dot{Y}]^{\top}$ is the state of the robot. The transition model (3.8) and (3.9) can be rewritten as:

$$\mathbf{x}^{+} = \Delta_{vlip}(\mathbf{x}^{-}) \tag{3.11}$$

where Δ_{vlip} indicates the transition map of the VLIP model. Thus the combination of the dynamic equations (3.6) and the transition model (3.11) forms the hybrid dynamical system:

$$\Sigma_{vlip} : \begin{cases} \dot{\mathbf{x}} = f_{vlip}(\mathbf{x}), & \mathbf{x}^{-} \notin \mathscr{S} \\ \mathbf{x}^{+} = \Delta_{vlip}(\mathbf{x}^{-}), & \mathbf{x}^{-} \in \mathscr{S} \end{cases} \tag{3.12}$$

3.3 Virtual Constraints

A normalized variable Φ monotonically increasing from 0 to 1 during one step, named phasing variable is defined to describe the desired trajectories of the controlled variables.

The trajectories of the swing foot and the vertical oscillation of CoM are defined as a function of Φ: $X_s = X_s(\Phi)$, $Y_s = Y_s(\Phi)$, $z_s = z_s(\Phi)$, $z_c = z_c(\Phi)$. The vertical evolution of swing foot determines the step timing while the horizontal evolution determines foot locations.

3.3.1 Switching manifold

In Chapter 2, the switching manifold for a 3D LIP model is defined as a segment with a certain orientation inside of the plane at the same level as the CoM, as described by equation (2.39). For a VLIP model whose CoM does not stay in the same height, this switching manifold must be extended into the 3D space.

The phasing variable is chosen such that the robot switches its stance leg when the CoM crosses a vertical plane:

$$\mathbf{S} = \{(X, Y, z_c) | (X - X^{*-}) + C(Y - Y^{*-}) = 0\}. \tag{3.13}$$

Similar as in Chapter 2 The orientation of the switching manifold $\mathbf{S}$ is parameterized by C, represented by the gray surface in Figure 3.2. In this figure, z_0 is the desired CoM height at the end of a step for a periodic motion. Many other sets of positions can be considered but since stability studied here is a local property, a flat surface is a convenient choice. The choice of $\mathbf{S}$ directly affects the final CoM position of a step.

3.3.2 Phasing Variable

As introduced in Chapter 2, the phasing variable Φ is defined as a function of X and Y with six parameters:

$$\Phi = a_1 X + a_2 Y + a_3 XY + a_4 X^2 + a_5 Y^2 + a_6, \tag{3.14}$$

and the phasing variable must vary from 0 to 1 for a step and be monotonic.

According to the constraints introduced by equation (2.45), parameters a_1, a_2, a_5, and a_6 can be obtained as functions of a_3 and a_4. There are many standards to choose the values of a_3 and a_4. For example, in Chapter 2, the value of a_3 was taken to be zero, and only the value of a_4 needs to be analyzed. Also, the values of a_3 and a_4 can be chosen as optimization variables to ensure the monotony of Φ. Here, the criterion of this optimization is chosen to minimize the difference between $\Phi(t)$ and t at each sampling

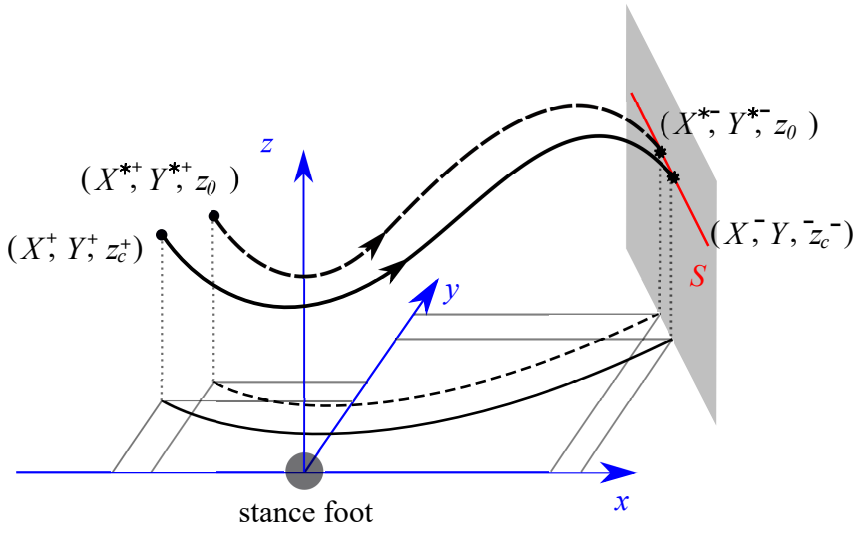

Figure 3.2 – The step finishes when the CoM crosses the switching manifold, which is represented by the gray surface. The curved dashed line is the periodic motion, and the curved solid line the CoM motion under an initial perturbation.

time as follows:

$$J = \Sigma(\Phi(t)_i - t_i)^2. \tag{3.15}$$

The matlab function *fmincon*® is used off-line when virtual constraint are designed.

3.3.3 The Motion of the swing foot

For the 3D VLIP model, the impact is ignored and the initial velocity of the swing foot at the beginning of each step is supposed to be zero. Thus, the motion of the swing foot along z axis is defined as the same cubic spline function as in Section 2.3.1.

For a periodic motion, the final CoM position along x and y axes at the end of a step is no longer $S/2$ and $D/2$. The swing foot position considering any final CoM position at the end of a step is expressed in a generalized form:

$$\begin{aligned} X_s^- &= (1 - k_S)(X^- - X^{*+}) + k_S S, \\ Y_s^- &= (1 - k_D)(Y^- + Y^{*+}) + k_D D. \end{aligned} \tag{3.16}$$

The same boundary conditions as in Section 2.3.2 are taken. Note that the expected final swing foot position proposed by equation (2.26) is a specific case of equation (3.16) when $X^{*-} = S/2$ and $Y^{*-} = D/2$. With the expected final swing foot position defined

by equation (3.16), the trajectories along x and y directions can be defined as 3^{rd} order polynomial functions of Φ.

3.3.4 Vertical Oscillation of the CoM

It has been proven by Chevallereau and Aoustin [10] that the vertical oscillation of the CoM can asymptotically stabilize a periodic walking gait. A polynomial function that keeps the motion of CoM continuous is used considering the following constraints:

$$\begin{aligned} z_c(0) &= z_c^+; \quad z_c(1) = z_0; \\ \dot{z_c}(0) &= \dot{z_c}^+; \quad \dot{z_c}(1) = v_m. \end{aligned} \tag{3.17}$$

where v_m represents the desired vertical CoM velocity before the transition of steps. The polynomial function is adapted at each step based on the measured values of z_c^+ and $\dot{z_c}^+$. The oscillations are chosen such that the final velocity for each step is downward i.e. $v_m < 0$.

3.4 Periodic gait of VLIP

For a 3D VLIP, the change of support is characterized by a change of the point where the angular momentum is calculated, thus we have [10]:

$$\begin{cases} \sigma_X^+ = \sigma_X^- - D\dot{z_c}^- \\ \sigma_Y^+ = -\sigma_Y^- + D\dot{z_c}^- \end{cases} \tag{3.18}$$

As the vertical velocity of the CoM right before the change of support is downward, it implies that the angular momenta σ_X and σ_Y decrease at the change of support. In order to obtain a periodic motion, these angular momenta must therefore increase during the stance phase, and thus it is necessary to slightly shift the relative position of the support leg and the CoM. The position of the CoM at the beginning of the step is then written as $X^+ = -1/2 + D_S$, $Y^+ = 1/2 - D_D$ and at the end of the step $X^- = 1/2 + D_S$, $Y^- = 1/2 + D_D$, where $D_S = \frac{X^+ + X^-}{2} \geq 0$ and $D_D = \frac{Y^- - Y^+}{2}$ are the shifts along x and y axes, as shown in Figure 3.3.

Since the model of walking is a hybrid model as shown in Section 3.2.3, a classical tool to define a periodic motion is to define the fixed point of the Poincaré return map. In this

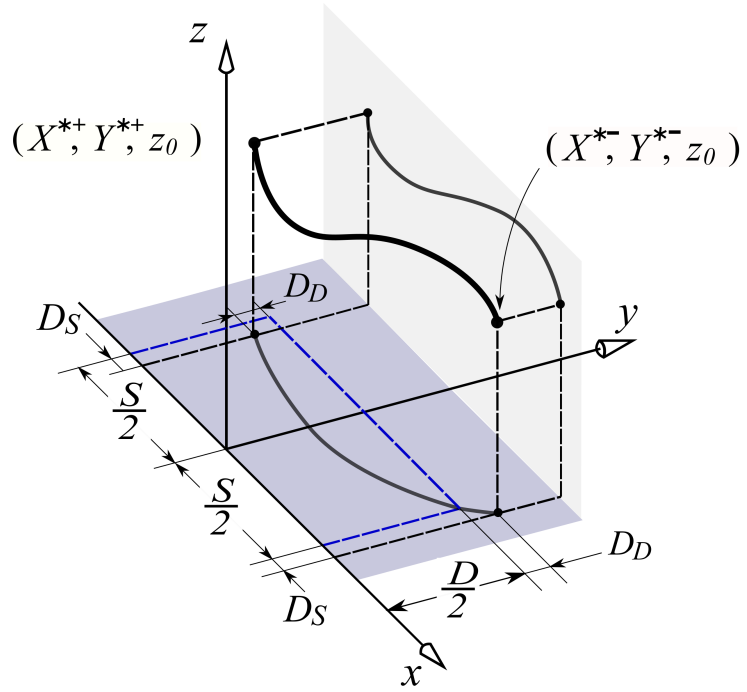

Figure 3.3 – The CoM trajectory of a periodic motion, and its projections in sagittal and horizontal planes.

study, we assume that a perfect tracking of the controlled variables is obtained, and the Poincaré section is defined by equation (3.13). In this context, since virtual constraints expressed as functions of $\Phi(X, Y)$ are used,the state of the robot in the Poincaré section is reduced to $[X^-, Y^-, \dot{X}^-, \dot{Y}^-]^\top$ and the Poincaré return map of steps k and $k+1$ can be written:

$$[X^-_{k+1}, Y^-_{k+1}, \dot{X}^-_{k+1}, \dot{Y}^-_{k+1}] = \mathcal{P}(X^-_k, Y^-_k, \dot{X}^-_k, \dot{Y}^-_k). \tag{3.19}$$

The periodic motion is characterized by the fixed point of the Poincaré return map and satisfies:

$$[X^-_k, Y^-_k, \dot{X}^-_k, \dot{Y}^-_k] - \mathcal{P}(X^-_k, Y^-_k, \dot{X}^-_k, \dot{Y}^-_k) = 0 \tag{3.20}$$

The elements $D_S = X^-_k - 1/2, D_D = Y^-_k - 1/2, \dot{X}^-_k, \dot{Y}^-_k$ are calculated by a given initial guess and MATLAB®function $fsolve$ with equation (3.20). As this optimization technique is applied for normalized parameters, the corresponding periodic steps for any step length and step width can be deduced.

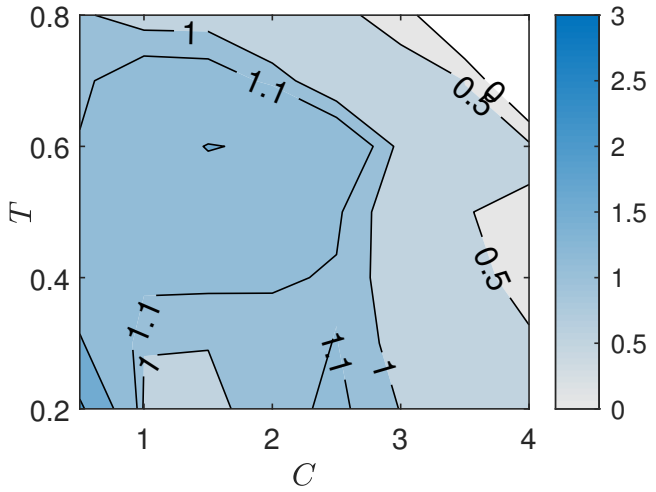

Figure 3.4 – The minimum value of $\dot{\Phi}$ as a function of C and T when $c = -0.8213, d = -0.6152$. The colored areas, with respect to the white areas, indicate that the phasing variable is monotonic.

3.4.1 Monotonicity analysis of the phasing variable

In this chapter, step timing varying between 0.2 s and 0.8 s and parameter C varying between 0.4 and 4 are analyzed for normalized step length and width. Considering the middle values of C and T, i.e. 0.5 s and 2.2 respectively, the derivative of Φ respect to time are calculated for any desired walking patterns. Here a walking pattern with parameters: $k_S = k_D = 0$, $z_0 = 0.7$ m, $v_m = -0.001$ m/s, $v_s = -0.1$ m/s is taken as an example. By using the optimization criterion give by equation (3.15), the values of c and d can be calculated:

$$a_3 = -0.8213;\ a_4 = -0.6152.$$

Thus, the other four parameters can be calculated:

$$a_1 = 1.4667;\ a_2 = 0.8992;\ a_5 = -0.2568;\ a_6 = 0.2179.$$

With these parameters, the minimum value of $\dot{\Phi}$ can be calculated for different values of C and T.

The values of C and T must be located inside the colored area shown in Figure 3.4 to make sure that the phasing variable is monotonic. The swing foot motion and the vertical CoM oscillation does not determine the monotonicity of the phasing variable. Since the

ratios of $\frac{D_S}{S}$ and $\frac{D_D}{S}$ are relatively small, the values of D_S and D_D do not determine the monotonicity either. To avoid calculating the values of phasing variable coefficient repeatedly, once the phasing variable coefficient is obtained, it can be used for walking gaits with different periodic motions and different virtual constraints.

3.4.2 The influence of C on the fixed point

The trajectory of the vertical CoM motion is a function of phasing variable Φ, whose value is affected by the value of C via solving the equation (2.45). Thus the solution of the periodic motion is affected by the value of C. How large the influence of C on the fixed point is studied here. The calculation is based on the parameters $v_m = -0.1$ m/s and $z_0 = 0.7$ m.

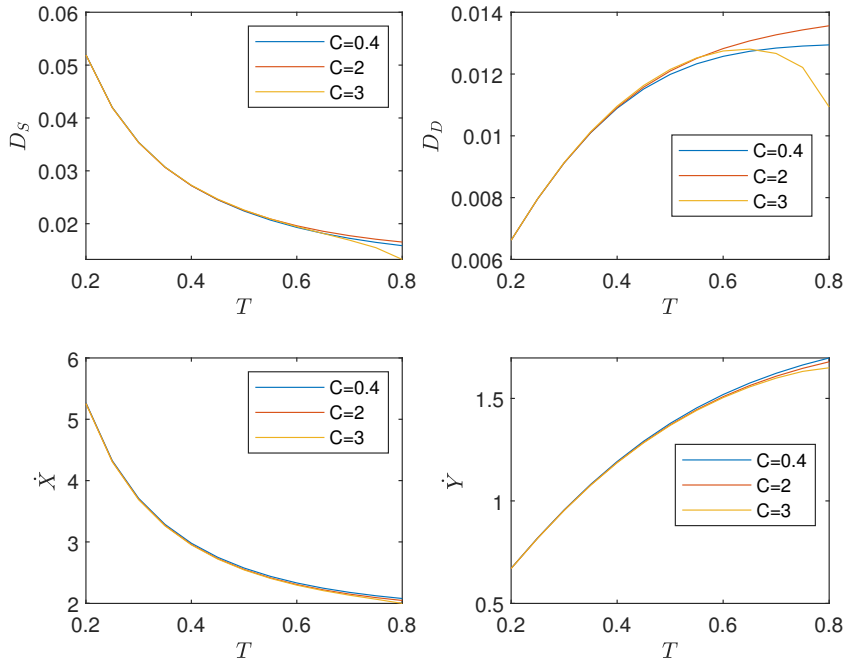

Figure 3.5 – Comparison of D_S, D_D, $\dot{X}$ and $\dot{Y}$ for $C = 0.4$, $C = 2$ and $C = 3$.

The characteristics of the cyclic motion as functions of T obtained for $C = 0.4$, $C = 2$ and $C = 3$ respectively are shown in Figure 3.5. It can be seen from Figure 3.5 that the influence of C on the fixed point is large but rather limited when the step duration increases. Figure 3.6 shows the influence of C on the CoM evolution when $T = 0.8$ s. The drawback is when the value of C changes, the periodic motion must be recalculated.

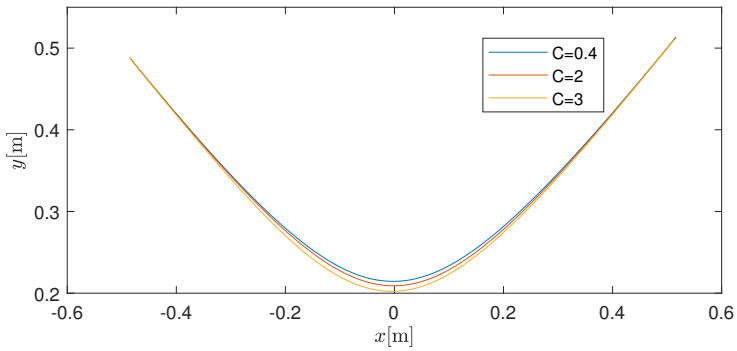

Figure 3.6 – The CoM trajectories for $T = 0.8$ s, $C = 0.4$, 2 and 3.

Since the influence is limited, the fixed point obtained for one value of C can be taken as a reference for finding the fixed point for another C.

3.5 The stability of control strategy applied to the 3D VLIP model

The stability of the walking gait based on the virtual constraints defined in Section 3.3 is now analyzed via the stability of the Poincaré return map. Since X^- and Y^- are coupled via the switching manifold, the Jacobian matrix of the Poincaré return map at the fixed point and its eigenvalues are calculated numerically in the coordinate system $[X, \dot{X}, \dot{Y}]^\top$.

3.5.1 Influence of C, T, k_S and k_D on the stability

The values of k_S and k_D determine the landing position of the swing foot, and consequently the initial CoM position for the next step. From the study with the 3D LIP model [92], we have observed that theses parameters are crucial for the stability of walking, thus the effect of these parameters is now considered in the case of the 3D VLIP model. Cases for different values of k_S and k_D are studied here. The other parameters are: $v_m = -0.1$ m/s, $z_0 = 0.7$ m. The value $v_m = -0.1$ m/s has been chosen according to the human vertical oscillations of the CoM. It has to be noted that in our study the DS phase is considered as instantaneous, while it is not instantaneous in human walk. This assumption of instantaneous phase is made to simplify the study and due to the fact that it increases the difficulty to have stable walking as the stability margin can be improved

using DS phase [93]. The evaluation of a pertinent choice of v_m to mimic human-like gait is not obvious since it varies with the placement of the instantaneous DS phase in the gait, thus we consider that a value $0 \leq v_m \leq -0.2\text{m/s}$ is convenient.

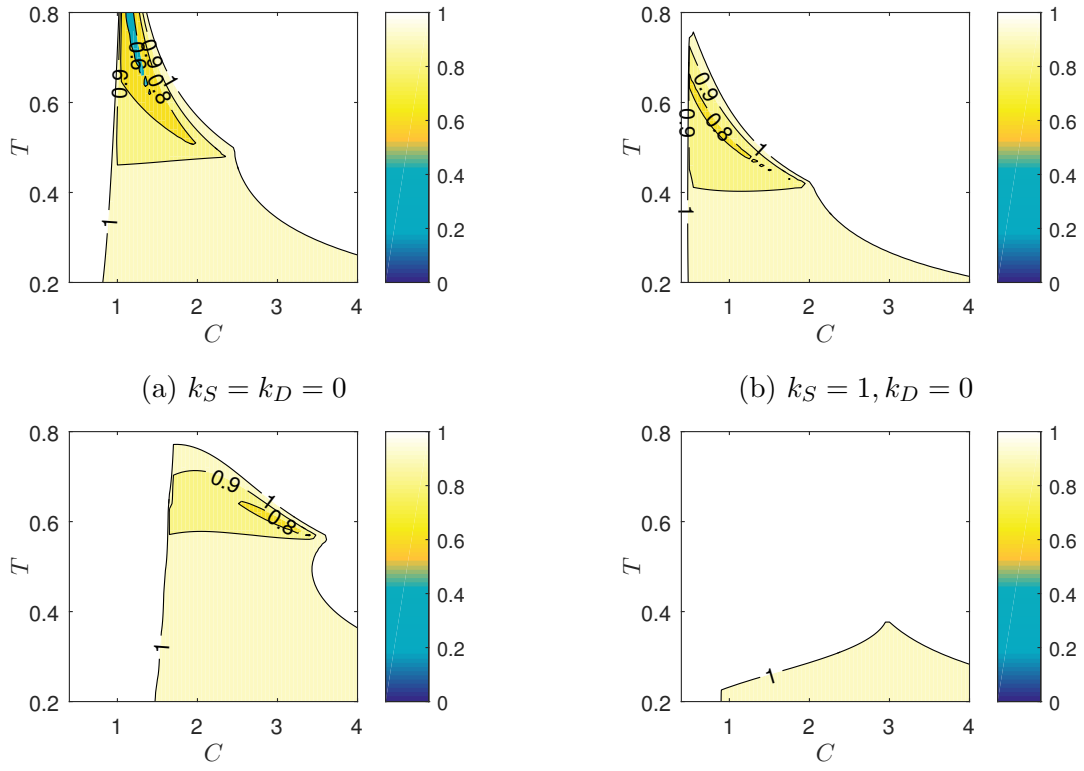

(a) $k_S = k_D = 0$

(b) $k_S = 1, k_D = 0$

(c) $k_S = 0, k_D = 1$

(d) $k_S = k_D = 1$

Figure 3.7 – Maximal norm of eigenvalues as functions of C and T for different k_S and k_D. Contrary to the white areas, the colored areas indicate self-stabilization condition.

From Figure 3.7, it can be seen that when k_S and k_D are smaller, that is when the initial CoM error in position is smaller, larger stability region can be obtained. When $k_S = 1, k_D = 1$, the proper value of T for stability is too small, only very fast steps can be achieved with stability. When T is relatively big, the range of C that satisfies the stability condition for $k_S = 0$ is larger than that for $k_S = 1$. Thus, $k_S = 0$ appears to be a good choice for stable walking. In the following we will consider the case $k_S = 0, k_D = 0$, that corresponds to placing the foot in order to nullify the initial error on the CoM position in horizontal plane for the next step. In presence of perturbation, this choice will induce some deviation in the lateral axis since $k_D = 0$ will prevent the robot from having a strict straight line motion [10]. In order to be able to avoid this lateral motion, the specific case

$k_S = 0, k_D = 1$ is also considered for the following sections where the influence of the choice of v_m is considered.

3.5.2 Influence of C, T and v_m on the stability

To study the influence of C, T and v_m on the eigenvalues, the values of z_0 is taken as constant: $z_0 = 0.7$ m. The results of the eigenvalues as a function of C and T for $v_m = -0.001$ m/s, $v_m = -0.01$ m/s, $v_m = -0.1$ m/s and $v_m = -0.2$ m/s are calculated for the cases $k_S = 0, k_D = 0$ (shown in Figure 3.8) and $k_S = 0, k_D = 1$ (shown in Figure 3.9).

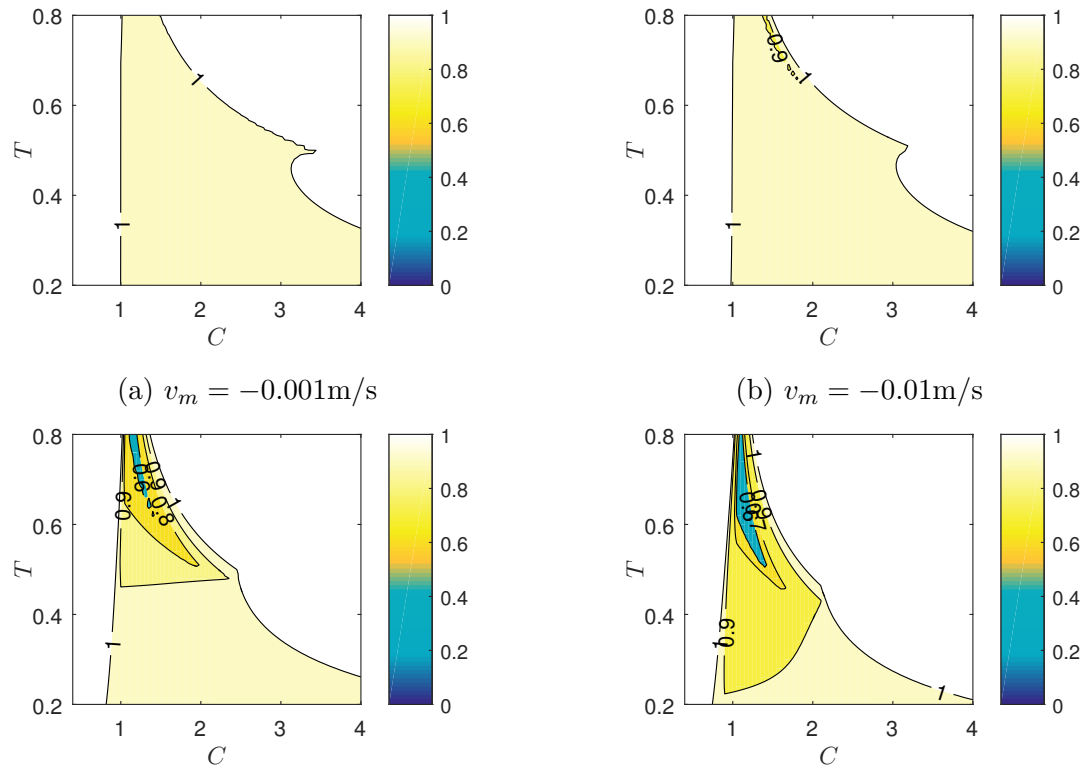

(a) $v_m = -0.001$m/s

(b) $v_m = -0.01$m/s

(c) $v_m = -0.1$m/s

(d) $v_m = -0.20$m/s

Figure 3.8 – Maximal norm of eigenvalues as functions of C and T for different v_m when $k_S = 0, k_D = 0$. Contrary to the white areas, the colored areas indicate self-stabilization condition.

It can be seen from Figures 3.8 and 3.9 that with a negative vertical CoM velocity at transition and proper choice of C and T, it is possible to obtain eigenvalues smaller

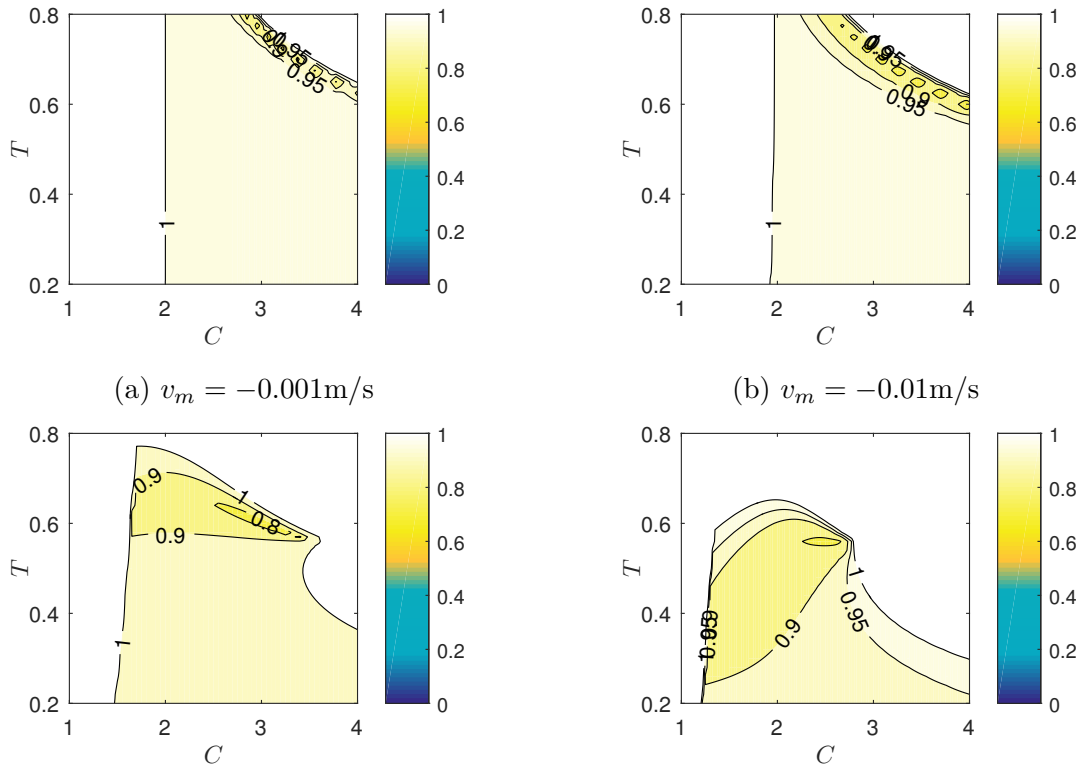

(a) $v_m = -0.001$m/s

(b) $v_m = -0.01$m/s

(c) $v_m = -0.1$m/s

(d) $v_m = -0.20$m/s

Figure 3.9 – Maximal norm of eigenvalues as functions of C and T for different v_m when $k_S = 0, k_D = 1$. Contrary to the white areas, the colored areas indicate self-stabilization condition.

than one, i.e. CoM oscillation can transfer a self-synchronized walking to a self-stabilized walking. The bigger the magnitude of v_m, the smaller the eigenvalue for a proper choice of C and T, which generally means faster convergence. For the case $k_S = 0, k_D = 1$, along with the increase of v_m, the area of proper T and C that satisfies the stability condition will decrease. When $k_S = 0, k_D = 0$, the eigenvalues are smaller than the case $k_S = 0, k_D = 1$, but the range of proper C is smaller when T is big. To obtain self-stabilization, the value of v_m must be chosen cautiously according to the desired step timing or walking velocity.

Note that C is defined for normalized step length and width. The proper value of C for real step length and width is proportional to the ratio of S and D, i.e.

$$C' = C \cdot \frac{S}{D}. \tag{3.21}$$

3.5.3 Simulations

To test the robustness and self-stabilization of the walking algorithm, simulations for $k_S = 0$, $k_D = 0$ and $k_S = 0$, $k_D = 1$ are made. The step length and width $S = 0.3$ m, $D = 0.15$ m are taken, while the desired height and vertical velocity of the CoM at the end of a step for a periodic motion are: $z_0 = 0.7$ m and $v_m = -0.1$ m/s respectively. When $T^* = 0.6$ s, according to the results shown in Figures 3.8c and 3.9c, $C_1 = 1.2$ and $C_2 = 2.5$ are proper values for obtaining self-stabilization when $k_S = 0$, $k_D = 0$ and $k_S = 0$, $k_D = 1$ respectively. Thus, $C_1' = 2.4$, $C_2' = 5$. When the key parameters describing the walking are chosen, the virtual constraints can be defined (see Section 3.3) and the periodic motion can be calculated (see Section 3.4).

In the simulations, we integrate a starting and stopping configuration where the robot is assumed to be in double support and to have a rest configuration. For the first step, the CoM of the VLIP starts from a position close to the future stance foot with a zero velocity, and for the last step, the CoM stops at a position close to the previous stance foot. As for the first and the last steps, the motion of the CoM is far from the periodic motion, the phasing variable based on the horizontal CoM position might not be monotonic. Thus for the starting and ending phase, controlled variables are chosen to be as functions of time. To obtain a CoM velocity of the VLIP in horizontal plane close to the periodic one at the end of the first step, the LIP model is used to estimate the initial CoM position for the first step [40]:

$$\begin{aligned} x_0 &= \frac{\dot{x}^*}{\sinh(\omega T^*)\omega}; \\ y_0 &= \frac{\dot{y}^*}{\sinh(\omega T^*)\omega} \end{aligned} \tag{3.22}$$

where $\omega = \sqrt{g/z_c}$ characterizes the LIP. With the same initial CoM position, at the end of the first step, the CoM of the VLIP will end up with smaller velocity along x axis than the LIP. When the velocity is too small and is outside of the basin of attraction, the robot will fall down after several steps. To increase the safety margin, the maximum CoM height of the VLIP is taken when calculating x_0 and y_0. Thus, the obtained initial position is $[x_0; y_0] = [0.0407; 0.0133]$ m. At the last step, an optimization method to minimize the CoM velocity is applied so that the CoM will stop to rest.

As shown in Figure 3.10, for the case when $k_S = 0$, $k_D = 0$, the CoM of the pendulum starts from a position close to the stance foot with a zero velocity. The red asterisks represent the CoM positions at transition. It can be seen in Figure 3.10 that these asterisks

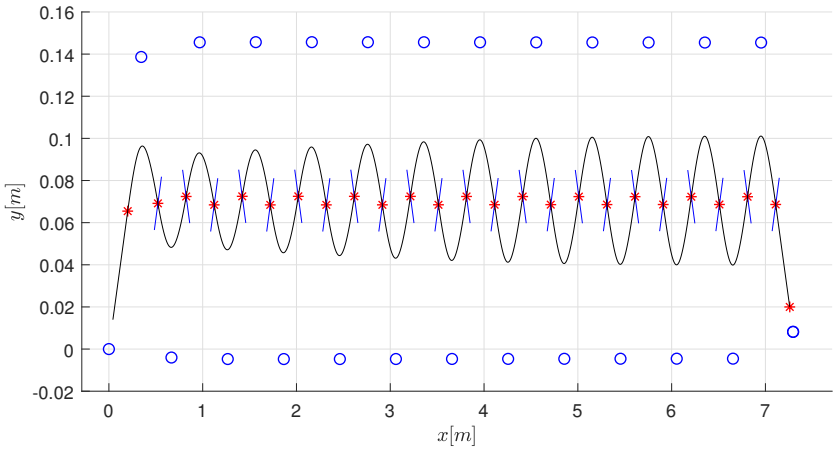

Figure 3.10 – The projection of the VLIP motion in horizontal plane for 25 steps when $k_S = 0, k_D = 0$. The black curves represent the CoM evolution, the blue circles represent the stance foot placements, and the blue lines represent the switching manifold.

do not have the same value of y at transition during the periodic motion due to the existence of D_D. A change of the landing position of the swing foot along y axis can be observed. This is due to the fact that the landing position strategy consists to nullify the initial CoM position error. From Figure 3.11, it can be seen that after the first step, the system has a state different from that of the periodic motion, and then converges asymptotically to the periodic motion for the following steps, thus self-stabilization is obtained. For the case when $k_S = 0$, $k_D = 1$, similar results are obtained, as shown in Figures 3.12 and 3.13. In this case, except for the first and the last steps which use a different landing strategy, the landing positions of the swing foot stay in a straight line i.e. the step width is constant. Faster convergence can be observed for the case $k_S = 0$, $k_D = 0$, which corresponds to the results shown in Figure 3.7. It can also be observed for both cases, the position converges faster than the velocity.

3.6 Change of the walking velocity

Due to the self-stabilization property of the control approach based on virtual constraints, different reference motions correspond to different walking velocities. When the humanoid has to adapt its walking velocity, the virtual constraints have to be changed. This can be done for example by inclining forward the torso to increase the walking veloc-

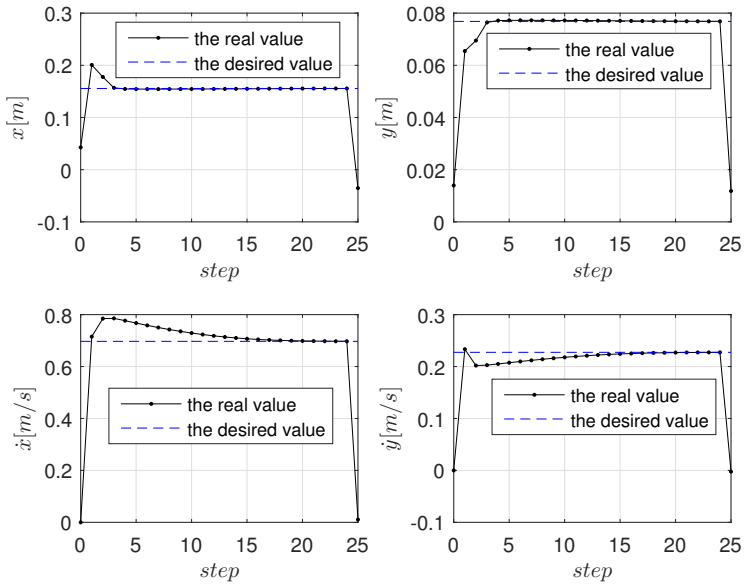

Figure 3.11 – CoM position and velocity evolutions for 25 steps when $k_S = 0, k_D = 0$ in the local reference frame.

ity [6]. In this section we explore the possibility to be able to adapt the walking velocity without recomputing new virtual constraints but only based on a feedback on the current walking speed. Different from the method proposed by Apostolopoulos *et el.* [94], the complex procedure of calculating the new periodic motion is unnecessary in this work.

It has been shown in Chapter 2 that the feedback of the CoM velocity along sagittal axis can provide self-stabilization for a LIP model. How this feedback affects the stability of a VLIP model is discussed here. By introducing the feedback of the walking speed, a new switching manifold was proposed:

$$\mathbf{S_v} = \{(X, Y, z) | (X - X^{*-} - l) + C(Y - Y^{*-}) = 0\}. \tag{3.23}$$

As shown in Figure 3.14, the new switching manifold $\mathbf{S_v}$ is a surface with an offset l from the switching manifold proposed in Section 3.3.1 along x axis. The offset is defined as $l = k_v(\dot{X}^{*+} - \dot{X}^{+})$, where $\dot{X}^{+}$ is the CoM velocity along x axis at the beginning of the current step. It allows to adjust the position of the switching manifold according to the velocity feedback of the CoM for each step. k_v is a parameter that must be chosen carefully to satisfy the stability condition.

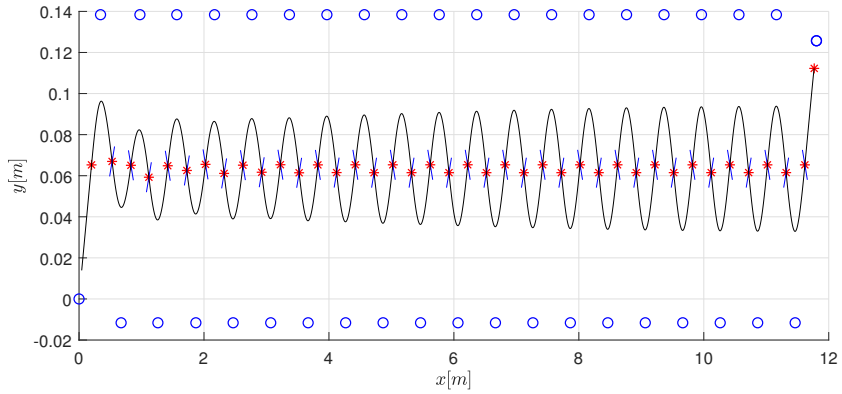

Figure 3.12 – The projection of the VLIP motion in horizontal plane for 40 steps when $k_S = 0, k_D = 1$. The black curves represent the CoM evolution, the blue circles represent the stance foot placements, and the blue lines represent the switching manifold.

3.6.1 Influence of C, k_v and v_m on the stability

Here, $T^* = 0.6$ s is taken and eigenvalues are calculated as functions of C and k_v for $v_m = 0$ m/s and $v_m = -0.1$ m/s. The results of two cases $k_S = 0, k_D = 0$ and $k_S = 0, k_D = 1$ are shown in Figures 3.15 and 3.16 respectively.

It can be seen from Figures 3.15a and 3.16a that for a LIP model (corresponding to the case $v_m = 0$), stability is obtained only for positive value of k_v. Contrary to this, it can been seen from Figures 3.15b and 3.16b that when $k_v = 0$, the eigenvalues are smaller than one, which means that the vertical oscillation of the CoM is enough to guarantee convergence to a periodic gait. From Figure 3.15b, it can be seen that a positive value of k_v helps to decrease the amplitude of the eigenvalue when $k_S = 0, k_D = 0$, while the effect is not so obvious when $k_S = 0, k_D = 1$ as shown in Figure 3.16b. However, for both cases, a feedback on the CoM velocity to define the switching manifold is useful if a specific walking velocity is desired.

3.6.2 Simulations

This section illustrates the change of switching manifold to control the walking velocity of the robot along the axis x. The same virtual constraints are used for all the simulations with desired velocities $\dot{X}^{*+}$ and $\dot{X}^{*+} + \Delta\dot{X}$, where $\Delta\dot{X}$ represents the desired increase of the CoM velocity along x axis.

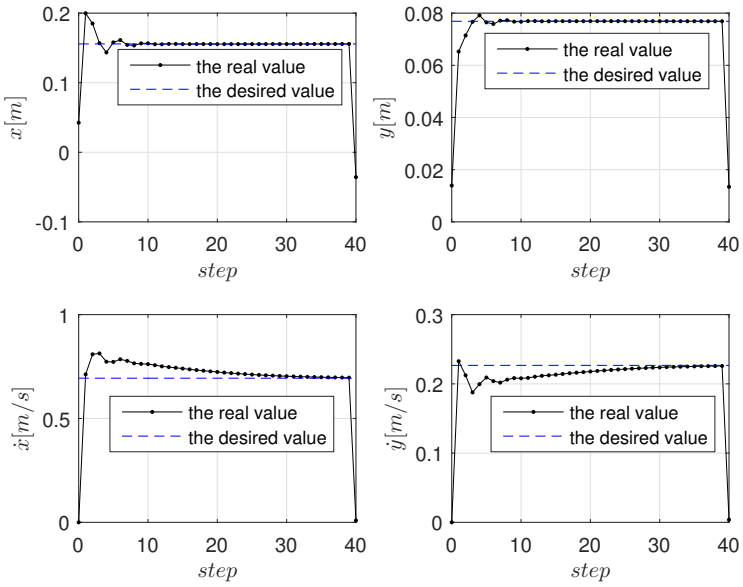

Figure 3.13 – CoM position and velocity evolutions for 40 steps when $k_S = 0, k_D = 1$ in the local reference frame.

Since the periodic motions for different velocities correspond to different X^{*-} and Y^{*-}, these values corresponding to $\dot{X}^{*+} + \Delta\dot{X}$ are unknown. The equation of the switching manifold (3.23) is conserved and not adapted to the desired velocity, thus the walk will not converge to the cyclic position nor to the desired velocity. In order to compensate the static error, an integration term of the velocity error is added into the offset l, which gives $l = k_v(\dot{X}^{*+} - \dot{X}^{+}) + k_I \sum_{i=1}^{k} (\dot{X}_i^{*+} - \dot{X}_i^{+})$, where k is number of the current step. The introduction of k_v and k_I allows the CoM to converge to a new periodic motion without defining explicitly the new periodic gait. While the desired CoM velocity along x axis increases (or decreases), its velocity along y axis will decrease (or increase) correspondingly.

The same parameters as in Section 3.5.3 are taken: $S = 0.3$ m, $D = 0.15$ m, $T^* = 0.6$ s, $z_0 = 0.7$ m and $v_m = -0.1$ m/s. The values of k_v and C are chosen to be $k_v = 0.08$, $C = 1.1$ for the case $k_S = 0, k_D = 0$ and $k_v = 0.03$, $C = 2.5$ for the case $k_S = 0, k_D = 1$ respectively based the results from Figures 3.15b and 3.16b. In order to show the convergence from one periodic motion to another one, an optimization method is used to determine the initial CoM position at the starting phase so that the state of the first step can be more close to the periodic motion. This is not discussed in detail because it does not affect the

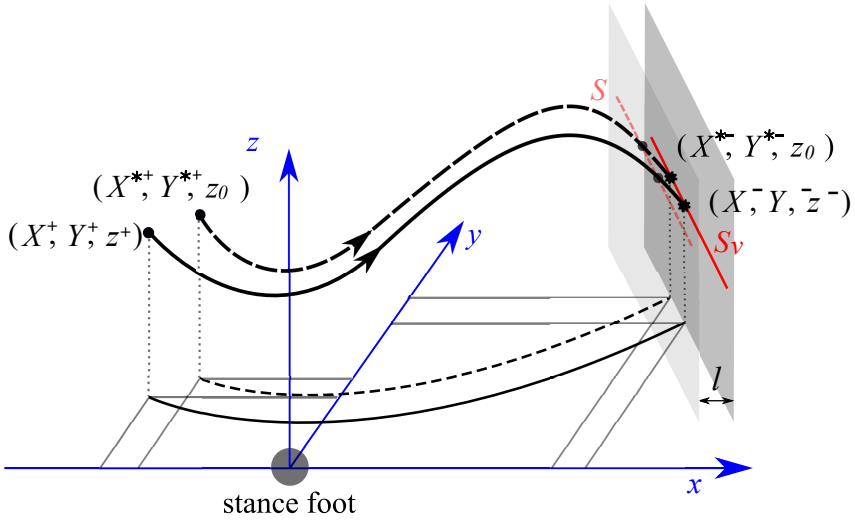

Figure 3.14 – The step finishes when the CoM crosses the switching manifold, which is represented by the darker gray surface. The curved dashed line is the periodic motion, and the curved solid line is the CoM motion under an initial position perturbation.

stability of the system. At the 10^{th} step, the desired CoM velocity along x axis $\dot{x}^{*+}$ is increased by 0.2 m/s.

It can be seen from Figures 3.17 and 3.19 that along with the increase of walking speed, the amplitude of the lateral CoM oscillations is reduced. For the case $k_S = 0$, $k_D = 0$ (shown in Figure 3.17), a large change of position along y axis can be also observed, while for the case $k_S = 0, k_D = 1$ (shown in Figure 3.19), the robot keeps walking along a straight line despite of the change of speed. From Figures 3.18 and 3.20, it can be observed that due to the change of the desired velocity from the 10^{th} step, the CoM velocity along x axis of the robot is drifted from its original velocity, and eventually converges to the desired velocity. Faster convergence can be observed for the case $k_S = 0$, $k_D = 0$, which corresponds to the results shown in Figures 3.15 and 3.16.

3.7 Conclusion

In this chapter, the model of the robot is simplified as a 3D VLIP model in order to describe a walking with a limited number of parameters and to highlight the parameters contributing to the stability of walking. The control law is based on virtual constraints. A switching manifold that decides when to switch the stance foot has been proposed. When

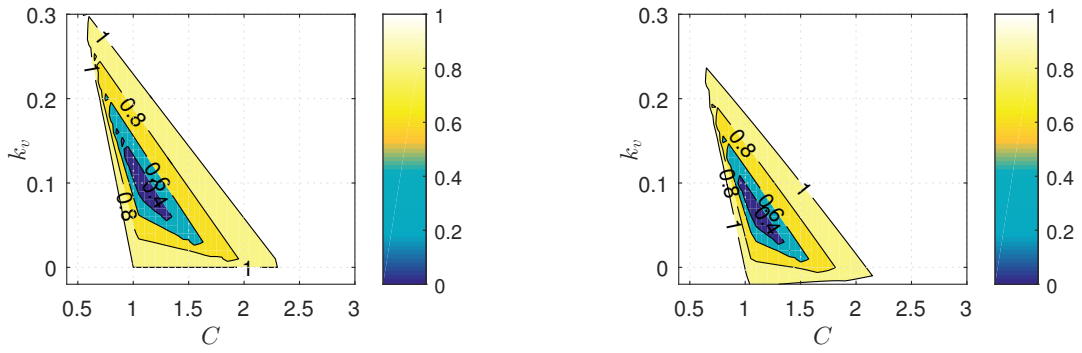

(a) $v_m = 0\text{m/s}$ (b) $v_m = -0.1\text{m/s}$

Figure 3.15 – Maximal norm of eigenvalues for different v_m as a function of C and k_v when $k_S = 0, k_D = 0$.

the switching manifold is a linear combination of the CoM position in horizontal plane, self-stabilization can be obtained when the vertical velocity of the CoM is negative, i.e. pointing downward. With proper choice of the values of the switching manifold parameters, the walk will asymptotically converge to the periodic motion, thus self-stabilization is obtained. The key parameters are : the vertical velocity of the CoM at the transition between steps that must be negative; the position of the foot at the transition that must reduce the position error of the CoM in the horizontal plane for the next step at least in sagittal plane; the orientation of the switching manifold that defines the position of the CoM in horizontal plane at transition between steps. Meanwhile, this chapter provided a simple way to define the trajectories of the controlled variables, such as the vertical CoM oscillation and the swing foot motion, by proposing a phasing variable that contains the free variables X and Y. Moreover, when a PI feedback of the CoM velocity along sagittal axis is taken into account, the walking speed of the robot can converge to another periodic motion with a different walking speed. This provides a novel approach for finding a periodic motion of bipedal robots without using an explicit method.

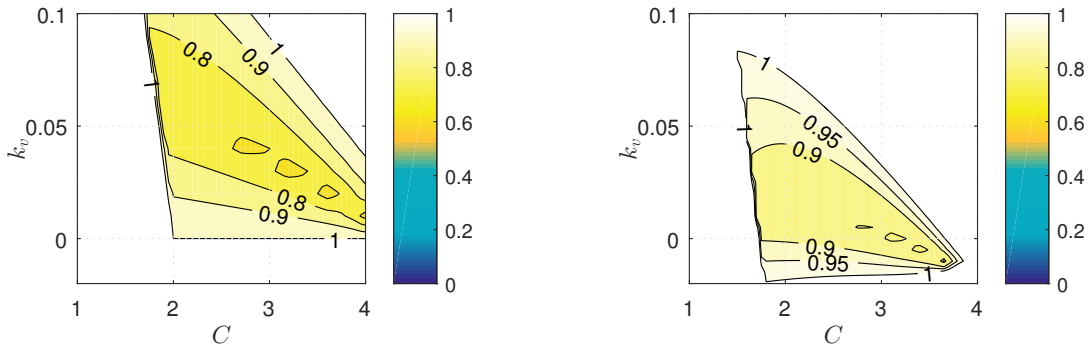

(a) $v_m = 0\text{m/s}$ (b) $v_m = -0.1\text{m/s}$

Figure 3.16 – Maximal norm of eigenvalues for different v_m as a function of C and k_v when $k_S = 0, k_D = 1$.

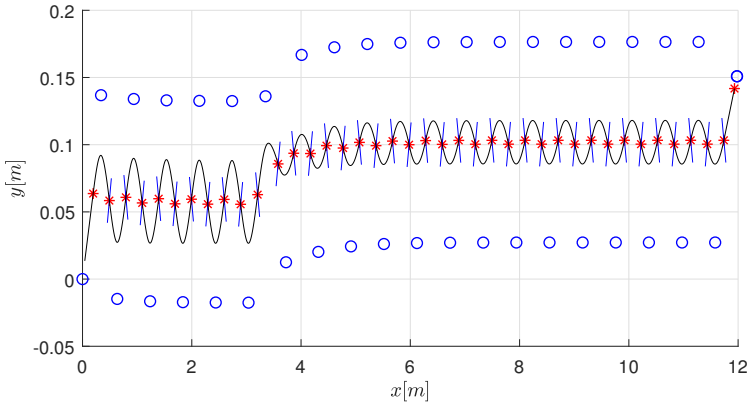

Figure 3.17 – The projection of the VLIP motion in horizontal plane for 40 steps when $k_S = 0, k_D = 0$. The black curves represent the CoM evolution, the blue circles represent the stance foot placements, and the blue lines represent the switching manifold.

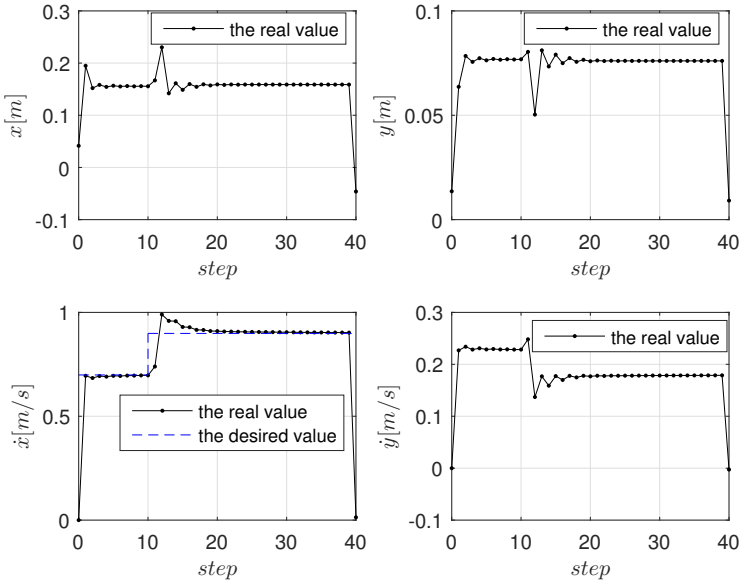

Figure 3.18 – CoM position and velocity evolutions for 40 steps when $k_S = 0, k_D = 0$ in the local reference frame.

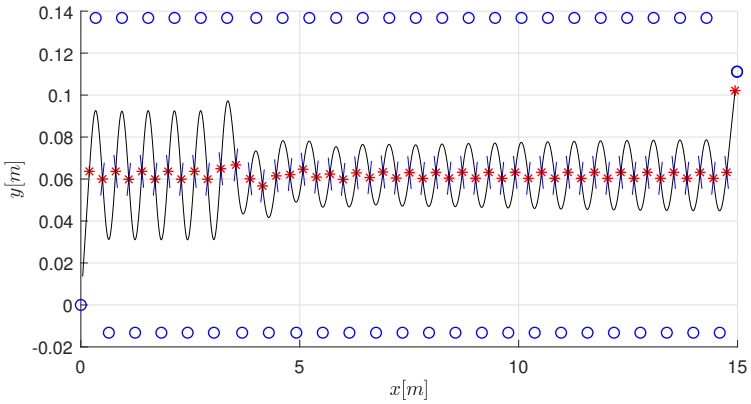

Figure 3.19 – The projection of the VLIP motion in horizontal plane for 50 steps when $k_S = 0, k_D = 1$. The black curves represent the CoM evolution, the blue circles represent the stance foot placements, and the blue lines represent the switching manifold.

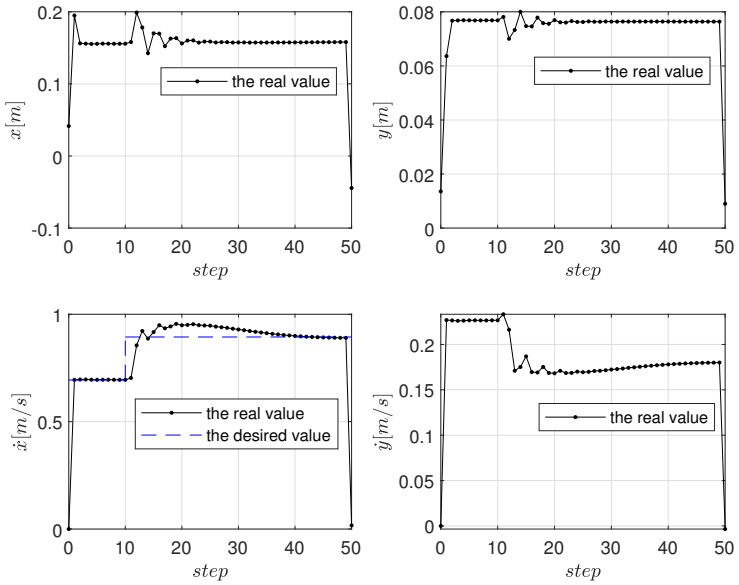

Figure 3.20 – CoM position and velocity evolutions for 50 steps when $k_S = 0, k_D = 1$ in the local reference frame.

Chapter 4

The Essential Model

4.1 Introduction

In the previous chapters, simplified models are used, because they show some essential factors of the walking, i.e. the equilibrium of the robot. However, with simplified models, some important dynamical effects are neglected. When replicating the walking gaits obtained for simplified models on the complete model of humanoid robots, the assumption that the ZMP stays inside of the convex hull of support may not be ensured for a fully actuated robot. In this chapter, the Essential Model is proposed, which is a novel model for walking that has the same dimension as the 3D LIP model but considers the complete dynamics of the humanoid. It can be written based on the internal states of the robot and possible external information, thereby generating models for different purposes. A particular case is when the motions of the robot are expressed as functions of a phasing variable based on the horizontal CoM position. This case is especially interesting in the context of this thesis. By considering this case, the Essential Model is then compared with the 3D LIP model by performing the same motion task. The proposed Essential Model is able to generate walking gaits which ensure that the ZMP is kept in an expected position or trajectory. Moreover, impacts between the swing foot and the ground can be considered to compute the periodic walking gaits. In the end of this chapter, the virtual constraints based walking algorithm proposed in the previous chapters is applied on this Essential Model to show the advantages of this model by performing numerical simulations of walking gaits for the humanoid robots Romeo and TALOS.

This chapter is structured as below: Section 4.2 introduces the hybrid dynamic model; Section 4.3 presents the procedure of obtaining the proposed Essential Model in detail. The connection between the Essential Model and the complete model in order to deduce the desired joint motions and the corresponding torques is also detailed in this section; Section 4.4 presents a brief discussion on generation of periodic walking patterns; Different cases showing the application of Essential Model on humanoid robots Romeo and TALOS

are shown in Section 4.5 and Section 4.6. Finally, conclusions of this chapter is discussed in Section 4.7.

4.2 The hybrid dynamic model

One step of the humanoid robot's walk contains two phases: the SS phase and the DS phase. This DS phase is assumed to be instantaneous. Continuous differential equations and discrete components are used to describe the motion of the robot and the transition between steps during the SS phase and the DS phase.

4.2.1 The continuous phase

The motion of biped walking during the single support phase is governed by nonlinear functions. For a robot with N joints, the dynamic model during the SS phase can be defined as follows:

$$D(q)\ddot{q} + H(q, \dot{q}) = Bu \tag{4.1}$$

where $q \in \mathbb{R}^N$ denotes the joint coordinates for a humanoid robot. For Romeo, $N = 31$ and for TALOS, $N = 30$. $D(q) \in \mathbb{R}^{N \times N}$ is the inertia matrix, $H(q, \dot{q}) \in \mathbb{R}^N$ groups the centrifugal, Coriolis and gravity terms, $B \in \mathbb{R}^{N \times r}$ is the input matrix and $u \in \mathbb{R}^r$ is the vector of torques applied by actuators at each joint, where r represents the number of actuators. For a fully actuated humanoid robot, we have $r = N$ and $B = I_{N \times N}$.

Let $\mathbf{x} = [q^\mathsf{T}, \dot{q}^\mathsf{T}]^\mathsf{T}$ represent the states of the robot, and the state-variable model can be written as:

$$\dot{\mathbf{x}} = f(\mathbf{x}) + g(\mathbf{x})u \tag{4.2}$$

This modeling assumes that the robot has a full contact between the sole of the foot and a rigid floor. The joints are defined assuming that the reference frame is fixed at the stance foot and thus the reaction force applied by the ground on the stance foot does not produce work and does not appear in the model.

4.2.2 Transition between steps

It is assumed that the local frame is always attached at the stance foot pointing towards the CoM of the robot, and the stance foot changes its role instantaneously when the swing foot touches the ground. Along with the change of the stance foot, the position

and direction of the local frame is changed in the world frame. The transition contains two phases: 1) the change of the joint rate caused by the impact between the swing foot and the ground; 2) the relabeling of joints due to the change of the local frame.

Impact model

Different from the previous chapters, the dynamic characteristics of the swing leg must be considered in the complete model of the robot, thus the impact model presented in Ref. [6] is discussed when the landing velocity of the swing foot is not zero. The impact is modeled as a contact between two rigid bodies, and the following hypotheses are made:

— HI1) an impact results from the contact between the swing foot and the ground;
— HI2) the impact is instantaneous;
— HI3) the impact results in no rebound and no slipping of the swing leg;
— HI4) at the moment of impact, the stance leg lifts from the ground without interaction;
— HI5) the externally applied forces during the impact can be represented by impulses;
— HI6) the actuators cannot generate impulses and hence can be ignored during impact;
— HI7) the impulsive forces may result in an instantaneous change in the robot's velocities, but there is no instantaneous change in the configuration.

Considering the reaction forces at the swing foot, the development of the impact model requires $(N+6)$-DoF model of the robot. A generalized set of coordinates $q_g = [q; \mathbf{x}_s; \phi_s]$ is considered, $\mathbf{x}_s = [x_s; y_s; z_s]$ and $\phi_e = [\psi_s; \theta_s; \varphi_s]$ are the position and orientation of the swing foot. Using q_g in the method of Lagrange results in:

$$D_g(q_g)\ddot{q}_g + H(q_g, \dot{q}_g) = B_g u + \delta F_{ext} \tag{4.3}$$

where δF_{ext} represents the vector of the external forces acting on the robot due to the contact between the foot and the ground, and D_g is the inertia matrix associated to the generalized coordinates.

Here we use '$-$' to denote the moment just before impact and '$+*$' to denote the moment just after impact but before the relabeling. Integrating equation (4.3) from the instant right before and after the impact obtains [95]:

$$D_g(q_g^{+*})\dot{q}_g^{+*} - D_g(q_g^{-})\dot{q}_g^{-} = F_{ext}, \tag{4.4}$$

where $F_{ext} := \int_{t^-}^{t^+} \delta F_{ext}(\tau) d\tau$ represents the integration of the impulsive contact force over the impact duration. According to hypothesis HI7, the impact does not change the robot's position. Since the walking gait is supposed to be symmetric, we have $q_g^{+*} = q_g^-$, thus $D_g(q_g^{+*}) = D_g(q_g^-)$.

The external force can be calculated as:

$$F_{ext} = J_s(q_g)^\top F_{imp} \tag{4.5}$$

where $J_s(q_g)$ is the Jacobian of the swing foot. F_{imp} is the impact intensity and remains unknown. The hypothesis HI3 gives:

$$J_s(q_g^{+*})\dot{q}_g^{+*} = 0 \tag{4.6}$$

Combining equation (4.4) and (4.6) yields:

$$\begin{bmatrix} D_g(q_g^{+*}) & (-J_s(q_g^{+*}))^\top \\ J_s(q_g^{+*}) & \mathbf{0}_{6\times 6} \end{bmatrix} \begin{bmatrix} \dot{q}_g^{+*} \\ F_{imp} \end{bmatrix} = \begin{bmatrix} D_g(q_g^-)\dot{q}_g^- \\ \mathbf{0}_{6\times 1} \end{bmatrix} \tag{4.7}$$

Equation (4.7) can be solved using the Schur complement [96], giving the expression of the joint velocities after the impact as function of the joint velocities before the impact

$$\dot{q}_g^{+*} = (I_{(N+6)\times(N+6)} - D_g^{-1} J_s^\top (J_s D_g^\top J_s^\top)^{-1}) J_s \dot{q}_g^- \tag{4.8}$$

The first N rows of equation (4.8) give the post impact map of the joint velocities:

$$\dot{q}^{+*} = \Delta(q)\dot{q}^- \tag{4.9}$$

where $\Delta(q)$ is a matrix that relates the joint velocities after and before the impact. Notice that if there is no impact at transition, i.e. when the landing velocity of the swing foot is zero, $\Delta(q) = I_{N\times N}$.

Relabeling

Since the y axis of the local frame is inverted and the numbering of the joints starts from the local frame, the sign conventions for all angles that are not in the sagittal plane are flipped and the joints need to be relabeled. Define the robot joints for the new

coordinates by:

$$q^+ = Eq^-. \tag{4.10}$$

The superscripts + and − represent the instants just after and just before the transition, and the matrix E defines the interchange of joint positions. With equation (4.9), the impact map of the joint velocities is given by:

$$\dot{q}^+ = E\Delta(q)\dot{q}^- \tag{4.11}$$

4.2.3 The hybrid model

At transition, the height of the swing foot is zero. Thus, a switching manifold can be defined:

$$\mathscr{S} := \{\mathbf{x} | z_s = 0\} \tag{4.12}$$

where z_s represents the height of the swing foot.

By combining the continuous model (4.2) and the transition models (4.10) and (4.11), the hybrid dynamic model of the robot can be obtained:

$$\Sigma : \begin{cases} \dot{\mathbf{x}} = f(\mathbf{x}) + g(\mathbf{x})u, & \mathbf{x}^- \notin \mathscr{S} \\ \mathbf{x}^+ = \Delta_x(\mathbf{x}^-), & \mathbf{x}^- \in \mathscr{S} \end{cases} \tag{4.13}$$

where $\Delta_x(\mathbf{x}^-) = [(Eq^-)^\intercal, (E\Delta(q)\dot{q}^-)^\intercal]^\intercal$.

4.2.4 The complete dynamic model

The dynamic model (4.1) considers the inertial frame linked to the stance foot. The ground reaction force does not appear in this equation since parametrization with implicit contact is used. Combining the ground reaction wrench $[F_0^\top, M_0^\top]^\top$ with the dynamic equation (4.1) yields the dynamic model in SS phase [65]:

$$\begin{bmatrix} F_0 \\ M_0 \\ u \end{bmatrix} = \begin{bmatrix} D_F(q) \\ D_M(q) \\ D(q) \end{bmatrix} \ddot{q} + \begin{bmatrix} H_F(q, \dot{q}) \\ H_M(q, \dot{q}) \\ H(q, \dot{q}) \end{bmatrix} := NE(q, \dot{q}, \ddot{q}) \tag{4.14}$$

where $F_0 = [F_x, F_y, F_z]^\top$ is a force vector generated in world frame Σ_0; $M_0 = [M_x, M_y, M_z]^\top$ is a torque vector generated in world frame Σ_0; $D_F \in \mathbb{R}^{3\times N}$, $D_M \in \mathbb{R}^{3\times N}$, $H_F \in \mathbb{R}^{3\times 1}$, and

$H_M \in \mathbb{R}^{3\times 1}$ are matrices and vectors used to compute the reaction wrench. The first six lines correspond to the global equilibrium of the robot, thus the centroidal equation [40]. The last N lines of the model correspond to equation (4.1), while the first six lines give the reaction force acting on the stance foot. Rearranging equation (4.14) yields:

$$\begin{bmatrix} F_0 \\ M_0 \\ u \end{bmatrix} = D_e(q)\ddot{q} + H_e(q,\dot{q}) \tag{4.15}$$

where $D_e = [D_F^\top, D_M^\top, D^\top]^\top \in \mathbb{R}^{(N+6)\times N}$, and $H_e = [H_F^\top, H_M^\top, H^\top]^\top \in \mathbb{R}^{(N+6)\times 1}$.

4.3 The proposed Essential Model

The main objective of the proposed Essential Model is to link the horizontal position of the CoM and ZMP or more precisely second derivative of the horizontal position of the CoM and ZMP as for the 3D LIP model. It has the same dimension as the 3D LIP model but considers the complete dynamics of the humanoid robot, and no approximation is made. The motion of the robot is coordinated based on some internal and/or external information. Furthermore, this Essential Model can be used to generate walking gaits that consider impacts with the ground and still keep the ZMP in a desired location as will be shown in further sections.

4.3.1 Development of the Essential Model

In this chapter, the horizontal CoM position x_c and y_c are chosen as free variables or internal variables, i.e. $q_f = [x_c, y_c]^\top$. With the Essential Model, it is desired to obtain the dynamics of the CoM in the horizontal plane by imposing the ZMP location. A fully-actuated robot model is considered here. At the ZMP, the reaction force does not produce any moment in the horizontal direction, i.e.

$$\begin{aligned} p_x^d F_z + M_y &= 0 \\ p_y^d F_z - M_x &= 0 \end{aligned} \tag{4.16}$$

where p_x^d and p_y^d are the expected coordinates of the ZMP.

Usually, it is difficult to directly propose some trajectories for the joints that produce a

desired evolution of the ZMP, i.e. fulfil the conditions (4.16). Therefore, *points of interest* of the robot can be chosen as controlled variables q_c in order to define the desired trajectories for them. These points of interest can be the robot's extremities such as the hands or the swing foot, or directly the joints.

A generalized variable $\xi \in \mathbb{R}^N$ is defined here, which is a vector that has the same dimension as q, containing all the coordinates of the chosen points of interest, such as the position and orientation of the swing foot, the orientation of the torso, the joints of the arms, etc. Since the values of the internal states q_f are crucial to develop the Essential Model, they must be included as points of interest. Therefore, only $N-2$ controlled outputs $q_c(q)$ can be chosen. Thus, vector ξ will be composed of the controlled variables $q_c(q)$ and the two internal non-controlled variables q_f, i.e.

$$\xi = \begin{bmatrix} q_c(q) \\ q_f(q) \end{bmatrix} = \begin{bmatrix} q_c(q) \\ x_c(q) \\ y_c(q) \end{bmatrix} := f_\xi(q). \tag{4.17}$$

Roughly speaking, this model can be viewed as a geometric model for the robot that gives the positions of points of interest and horizontal position of the CoM as functions of the joint coordinates.

On the other hand, a desired trajectory for the $N-2$ controlled variables is defined as functions of Φ i.e. $q_c^d(\Phi)$, where Φ is a phasing variable based on q_f or possible external information. When trajectories $q_c^d(\Phi)$ are defined, the output vector is created

$$y_{out} = q_c(q) - q_c^d(\Phi). \tag{4.18}$$

Let us call ξ_d the vector of desired generalized variables defined by

$$\xi_d = \begin{bmatrix} q_c^d(\Phi) \\ q_f \end{bmatrix} = \begin{bmatrix} q_c^d(\Phi) \\ x_c \\ y_c \end{bmatrix} := f_d(\vartheta), \tag{4.19}$$

where $\vartheta = [x_c,\ y_c,\ \phi]^\top \in \mathbb{R}^{m+2}$ is a generalized vector. Here, $\phi \in \mathbb{R}^m$ is a possible external variable vector with $m \geq 0$. For example, when the external variable is time, i.e. $\phi = t$, then $m = 1$. If the external variable vector ϕ is used for modifying the evolution of the joints, the time derivatives, i.e. $\dot{\phi}$ and $\ddot{\phi}$ must be known.

When the system achieves the desired trajectory $q_c^d(\Phi)$, i.e. $y_{out} \equiv 0$, the internal

dynamics due to the non-controlled variables is the only dynamics that remains and the system is said to evolve on the zero dynamics [97]. Recalling that the simplification of the *Essential Model* is based on the assumption of a perfect tracking, we have $\xi \equiv \xi_d$, thus the position of the controlled variables $q_c(q)$ can be deduced by just knowing the states ϑ.

In order to compute the joint motions, the first and second time derivatives of equation (4.17) are needed, i.e

$$\dot{\xi} = J_\xi(q)\dot{q} \tag{4.20}$$

and

$$\ddot{\xi} = J_\xi(q)\ddot{q} + \dot{J}_\xi(q)\dot{q} \tag{4.21}$$

where $J_\xi(q) = \frac{\partial f(q)}{\partial q} \in \mathbb{R}^{N\times N}$.

From the first and second time derivatives of equation (4.19) we have

$$\dot{\xi}_d = \frac{\partial f_d(\vartheta)}{\partial \vartheta}\dot{\vartheta} = J_d(\vartheta)\dot{\vartheta} \tag{4.22}$$

and

$$\ddot{\xi}_d = J_d(\vartheta)\ddot{\vartheta} + \dot{J}_d(\vartheta)\dot{\vartheta} \tag{4.23}$$

where $J_d(\vartheta) \in \mathbb{R}^{N\times(m+2)}$ is defined as

$$J_d(\vartheta) = \begin{bmatrix} \frac{\partial \boldsymbol{q}_c^d(\Phi)}{\partial x} & \frac{\partial \boldsymbol{q}_c^d(\Phi)}{\partial y} & \frac{\partial \boldsymbol{q}_c^d(\Phi)}{\partial \phi_1} & \cdots & \frac{\partial \boldsymbol{q}_c^d(\Phi)}{\partial \phi_m} \\ 1 & 0 & 0 & \cdots & 0 \\ 0 & 1 & 0 & \cdots & 0 \end{bmatrix}.$$

It is assumed that $y_{out} \equiv 0$, $\dot{y}_{out} \equiv 0$ and $\ddot{y}_{out} \equiv 0$. So, by relating equations (4.17) and (4.19), (4.20) and (4.22), and (4.21) and (4.23) we have

$$f_{xi}(q) = f_d(\vartheta) \tag{4.24}$$

$$J_\xi(q_d(\vartheta))\dot{q} = J_d(\vartheta)\dot{\vartheta} \tag{4.25}$$

$$J_\xi(q_d(\vartheta))\ddot{q} + \dot{J}_\xi(q_d(\vartheta))\dot{q} = J_d(\vartheta)\ddot{\vartheta} + \dot{J}_d(\vartheta)\dot{\vartheta} \tag{4.26}$$

Thus, joint variables q, $\dot{q}$ and $\ddot{q}$ can be deduced from the state ϑ and its time derivatives $\dot{\vartheta}$ and $\ddot{\vartheta}$, as

$$q = f_\xi^{-1}\left(f_d(\vartheta)\right) \tag{4.27}$$
$$\dot{q} = J_\xi^{-1}(\vartheta) J_d(\vartheta)\dot{\vartheta} \tag{4.28}$$
$$\ddot{q} = J_\xi^{-1}(\vartheta)\left[J_d(\vartheta)\ddot{\vartheta} + \dot{J}_d(\vartheta,\dot{\vartheta})\dot{\vartheta} - \dot{J}_\xi(\vartheta,\dot{\vartheta})J_\xi^{-1}(\vartheta)J_d(\vartheta)\dot{\vartheta}\right] \tag{4.29}$$

where J_ξ is invertible by assuming a convenient choice of q_c^d, and (4.29) comes from solving $\ddot{q}$ in (4.26) and using (4.28).

Thus, by substituting (4.29) into (4.15) we have:

$$NE = D_e J_\xi^{-1}(\vartheta)\left[J_d(\vartheta)\ddot{\vartheta} + \dot{J}_d(\vartheta,\dot{\vartheta})\dot{\vartheta} - \dot{J}_\xi(\vartheta,\dot{\vartheta})J_\xi^{-1}(\vartheta)J_d(\vartheta)\dot{\vartheta}\right] + H_e \tag{4.30}$$

where $NE = [F_0,\ M_0,\ u]^\top$, and then rearrange equation (4.30), we have:

$$NE = D_\vartheta \ddot{\vartheta} + H_\vartheta \tag{4.31}$$

where $D_\vartheta(\vartheta) \in \mathbb{R}^{(N+6)\times(m+2)}$ and $H_\vartheta(\vartheta,\dot{\vartheta}) \in \mathbb{R}^{N+6}$ are given by

$$\begin{aligned} D_\vartheta &= D_e J_\xi^{-1} J_d \\ H_\vartheta &= D_e[J_\xi^{-1}\dot{J}_d\dot{\vartheta} - J_\xi^{-1}\dot{J}_\xi J_\xi^{-1} J_d\dot{\vartheta}] + H_e. \end{aligned}$$

Notice that $-J_\xi^{-1}\dot{J}_\xi J_\xi^{-1} = \frac{\mathrm{d}}{\mathrm{d}t}\left(J_\xi^{-1}\right)$ [1].

Equation (4.31) can be split into

$$NE = D_\vartheta(:,1)\ddot{x}_c + D_\vartheta(:,2)\ddot{y}_c + D_\vartheta(:,3)\ddot{\phi}_1 + \ldots + D_\vartheta(:,m)\ddot{\phi}_m + H_\vartheta. \tag{4.32}$$

1. From the fact that $\frac{\mathrm{d}}{\mathrm{d}t}\left(J_\xi J_\xi^{-1}\right) = 0_{N\times N}$, it can be expanded it as $\dot{J}_\xi J_\xi^{-1} + J_\xi \frac{\mathrm{d}}{\mathrm{d}t}\left(J_\xi^{-1}\right) = 0$ and the equivalence is obtained.

By taking into account rows 3 to 5 of equation (4.32) we have that

$$\begin{aligned} F_z =& D_\vartheta(3,1)\ddot{x}_c + D_\vartheta(3,2)\ddot{y}_c + D_\vartheta(3,3)\ddot{\phi}_1 \\ &+ \ldots + D_\vartheta(3,m)\ddot{\phi}_m + H_\vartheta(3) \\ M_x =& D_\vartheta(4,1)\ddot{x}_c + D_\vartheta(4,2)\ddot{y}_c + D_\vartheta(4,3)\ddot{\phi}_1 \\ &+ \ldots + D_\vartheta(4,m)\ddot{\phi}_m + H_\vartheta(4) \\ M_y =& D_\vartheta(5,1)\ddot{x}_c + D_\vartheta(5,2)\ddot{y}_c + D_\vartheta(5,3)\ddot{\phi}_1 \\ &+ \ldots + D_\vartheta(5,m)\ddot{\phi}_m + H_\vartheta(5) \end{aligned} \tag{4.33}$$

In order to obtain the desired position of the ZMP, equations (4.16) must be satisfied. Then, by using (4.33) into (4.16) we get

$$\begin{aligned} &p_x^d \left[D_\vartheta(3,1)\ddot{x}_c + D_\vartheta(3,2)\ddot{y}_c + D_\vartheta(3,3)\ddot{\phi}_1 + \cdots + D_\vartheta(3,m)\ddot{\phi}_m + H_\vartheta(3) \right] + \\ &\left[D_\vartheta(5,1)\ddot{x}_c + D_\vartheta(5,2)\ddot{y}_c + D_\vartheta(5,3)\ddot{\phi}_1 + \cdots + D_\vartheta(5,m)\ddot{\phi}_m + H_\vartheta(5) \right] = 0 \end{aligned} \tag{4.34}$$

$$\begin{aligned} &p_y^d \left[D_\vartheta(3,1)\ddot{x}_c + D_\vartheta(3,2)\ddot{y}_c + D_\vartheta(3,3)\ddot{\phi}_1 + \cdots + D_\vartheta(3,m)\ddot{\phi}_m + H_\vartheta(3) \right] - \\ &\left[D_\vartheta(4,1)\ddot{x}_c + D_\vartheta(4,2)\ddot{y}_c + D_\vartheta(4,3)\ddot{\phi}_1 + \cdots + D_\vartheta(4,m)\ddot{\phi}_m + H_\vartheta(4) \right] = 0. \end{aligned} \tag{4.35}$$

Equations (4.34) and (4.35) can be arranged by splitting the internal states and external variables, such as

$$D_f(\vartheta, p)\ddot{q_f} + D_\phi(\vartheta, p)\ddot{\boldsymbol{\phi}} + H_R(\vartheta, \dot{\vartheta}) = 0, \tag{4.36}$$

where $D_f(\vartheta, p) \in \mathbb{R}^{2\times 2}$, $D_\phi(\vartheta, p) \in \mathbb{R}^{2\times m}$ and $H_R(\vartheta, \dot{\vartheta}) \in \mathbb{R}^2$ are given by

$$\begin{aligned} D_f &= \begin{bmatrix} p_x^d D_\vartheta(3,1) + D_\vartheta(5,1) & p_{x,d} D_\vartheta(3,2) + D_\vartheta(5,2) \\ p_y^d D_\vartheta(3,1) + D_\vartheta(4,1) & p_y^d A_\vartheta(3,2) + D_\vartheta(4,2) \end{bmatrix} \\ D_\phi &= \begin{bmatrix} p_x^d D_\vartheta(3,3) + D_\vartheta(5,3) & \cdots & p_x^d D_\vartheta(3,m) + D_\vartheta(5,m) \\ p_y^d D_\vartheta(3,3) + D_\vartheta(4,3) & \cdots & p_y^d D_\vartheta(3,m) + D_\vartheta(4,m) \end{bmatrix} \\ H_R &= \begin{bmatrix} p_x^d H_\vartheta(3) + H_\vartheta(5) \\ p_y^d H_\vartheta(3) + H_\vartheta(4) \end{bmatrix}. \end{aligned}$$

It has been checked numerically that matrix D_f is invertible, and from equation (4.36)

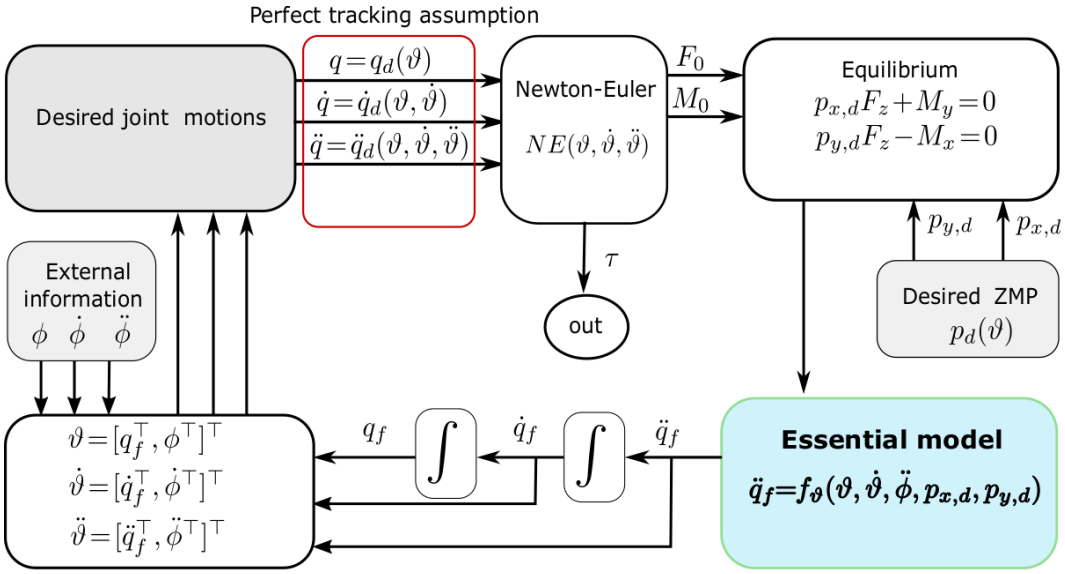

Figure 4.1 – A summary of the development of the Essential Model.

the Essential Model is computed as

$$\ddot{q_f} = -D_f^{-1}\left(D_\phi\ddot{\boldsymbol{\phi}} + H_R\right) \tag{4.37}$$

or well

$$\begin{bmatrix} \ddot{x}_c \\ \ddot{y}_c \end{bmatrix} = f_\vartheta(\vartheta,\dot{\vartheta},\ddot{\phi},p_x^d,p_y^d). \tag{4.38}$$

In this way, the dynamic behavior of the humanoid robot with given $q_c^d(\vartheta)$ that keeps the ZMP in a desired position $(p_x^d,\ p_y^d)$ during all the gait is described by the Essential Model (4.38), which gives the convenient evolution of the horizontal acceleration of the CoM, and by integration its horizontal velocity and position. A summary of this procedure is shown in Figure 4.1. Note that in the Essential Model, the simplification of the model is not based on any approximation of the dynamics, but on the assumption that the reference trajectories of the joints are perfectly tracked. This model can be designed as a function of internal states and possible external variables. In all cases, the Essential Model defines the acceleration of the non-controlled variables (in this chapter, the horizontal position of the CoM), as a function of the desired position of the ZMP and the desired configuration of the robot. Thus, the dimension of the system is four, i.e. the internal variables q_f and $\dot{q}_f$. In the following sections, simple cases of the application of this Essential Model will

be shown, namely, for virtual constraints defined as a phasing variable based on q_f (the horizontal CoM position) and when the time is included as external information ($\phi = t$). Let us remark that not only time but other kinds of external variables can be used as external information, such as the CoM of another biped robot, the CoM of a human, etc. However, this study is out of the scope here but it can be performed in the future.

4.3.2 Essential model based only on virtual constraints.

The hypothesis for the development of this model is the assumption that the motion of the joints is defined as a function of a phasing variable based on the internal information $\Phi = \Phi(q_f)$, thus we have $\vartheta = [x_c; y_c]$. Since ϕ is not considered the term $D_\phi \ddot{\boldsymbol{\phi}}$ on the Essential Model (4.37) vanishes and the model is reduced to

$$\begin{bmatrix} \ddot{x}_c \\ \ddot{y}_c \end{bmatrix} = -D_f^{-1} H_R = f_{x,y}(x_c, y_c, \dot{x}_c, \dot{y}_c, p_x^d, p_y^d) \tag{4.39}$$

This particular model can be used to perform walking gaits by making the robot walk only by considering its state. This description of the gait is based on virtual constraints and it has been efficiently used in numerous studies such as [8,10,68,98,99], among others. Notice that, trajectories based on the internal states of the robot are more natural since the robot will not try to catch a time varying function after some perturbation. Nevertheless, the desired step time lapse is not ensured.

4.3.3 Essential model based on its CoM and time

The hypothesis for the development of this model is the assumption that the motion of the controlled variable q_c is defined as a function of a phasing variable based on time i.e. $\Phi = \Phi(t)$, thus we have $\vartheta = [x_c; y_c; t]$. Notice that by only including the time, $\dot{\boldsymbol{\phi}} = 1$ and $\ddot{\boldsymbol{\phi}} = 0$. Thus as the previous case, term $D_\phi \ddot{\boldsymbol{\phi}}$ on the Essential Model (4.37) vanishes and the model is reduced to

$$\begin{bmatrix} \ddot{x}_c \\ \ddot{y}_c \end{bmatrix} = -D_f^{-1} H_R = f_{x,y,t}(t, x_c, y_c, \dot{x}_c, \dot{y}_c, p_x^d, p_y^d) \tag{4.40}$$

This particular model can be used to develop walking gaits that ensure that each step is performed at the desired step time lapse, as it is done in many works such as in [2,100–102].

In the following section this model will be compared with the 3D LIP model to highlight its performance and effectiveness.

4.4 Generation of periodic walking patterns

In this section, the generation of periodic walking patterns is studied. The studied gaits are composed of a SS phase and an instantaneous DS phase.

4.4.1 The evolution of the CoM

Due to the mass distribution, and to the eventual loss of angular momentum at impact, a periodic motion of the CoM by considering the complete model is not necessarily a symmetric motion along the sagittal and frontal planes [10]. Therefore, the periodic motion characterized by the state of the CoM at the end of a step is defined as

$$x_c^{*-} = [x_c^{*-},\ y_c^{*-},\ \dot{x}_c^{*-},\ \dot{y}_c^{*-}]^\top \tag{4.41}$$

with

$$x_c^{*-} = \frac{S}{2} + D_x,$$
$$y_c^{*-} = \frac{D}{2} + D_y,$$

where S is the step length, D the step width, and D_x and D_y are small displacements of the CoM in X and Y directions.

By knowing the states of the CoM before impact x_c^{*-}, the joint velocities $\dot{q}^{*-}$ are computed by using (4.28), with $\vartheta^{*-} = [x_c^{*-},\ y_c^{*-},\ \phi^{*-\top}]^\top$ and $\dot{\vartheta}^{*-} = [\dot{x}_c^{*-},\ \dot{y}_c^{*-},\ \dot{\phi}^{*-\top}]^\top$ where ϕ^{*-} and $\dot{\phi}^{*-}$ are the external information at the end of the step. For instance for the case when $\phi = t$, $\phi^{*-} = T$ and $\dot{\phi}^{*-} = 1$. Later, by using the transition model (4.11) the joint velocities after impact $\dot{q}^+$ are obtained. Then, the initial velocities of the generalized variables after the transition $\dot{\xi}(q^+, \dot{q}^+)$ are deduced by means of (4.20), namely, the initial velocities of the controlled variables and the CoM are obtained, i.e. $\dot{q}_c(q^+, \dot{q}^+)$ and $(\dot{x}_c^{*+},\ \dot{y}_c^{*+})$. Combined with the transition model (4.10) the initial states of the CoM at the beginning of a periodic step $x_c^{*+}(q^+, \dot{q}^+) = [x_c^{*+},\ y_c^{*+},\ \dot{x}_c^{*+},\ \dot{y}_c^{*+}]^\top$ are deduced. During the transition, the configuration of the robot is constant but the stance

leg changes, therefore the initial position of the CoM w.r.t the new stance leg is given by

$$x_c^{*+} = -\frac{S}{2} + D_x,$$
$$y_c^{*+} = \frac{D}{2} - D_y.$$

Notice that, without impact, the velocities of the CoM before and after the transition are the same (by taking into account the change in Y direction in the new frame), i.e. $\dot{x}_c^{*+} = \dot{x}_c^{*-}$, $\dot{y}_c^{*+} = -\dot{y}_c^{*-}$. In the simulations the periodic state is obtained numerically such that after one cycle (i.e. an instantaneous DS phase plus a SS phase) the same state is obtained in the case of symmetric motion on right and left legs.

4.4.2 The desired motion of the swing foot and upper body

The motion of the swing foot and upper body is defined by the desired controlled coordinates $q_c^d(\Phi)$. Since the Essential Model is developed under the assumption that the reference trajectories (4.18) are fulfilled for all the time, i.e.

$$y_{out} \equiv 0, \quad \dot{y}_{out} \equiv 0, \quad \ddot{y}_{out} \equiv 0, \tag{4.42}$$

achievable desired trajectories for $q_c^d(\Phi)$ must be generated in so that any well-suited control law can accomplish (4.42). Therefore, the change of velocity of the controlled variables after impact must be taken into account to compute the desired trajectories $q_c^d(\Phi)$.

The motion of the swing foot can be split in two parts: the vertical motion and the horizontal motion. The design of the vertical trajectory is based on the goal of producing or not an impact of the landing foot with the ground. For the horizontal motion, the landing place to step the foot is an important issue on which the performance of the walking gait will largely depend (see [99]).

On the other hand, several research works, as in [103, 104], have proven that the motions of the trunk and arms help to improve the walking efficiency and stability. Furthermore, some tasks that allow the robot to interact with the environment can be performed by the arms while the robot walks. Therefore, depending on the complexity of the task the desired upper-body motion trajectories can be defined by simple polynomials or more complex functions.

4.5 Case study: the humanoid robot Romeo

4.5.1 Introduction of Romeo

In this section, the complete model of the humanoid robot Romeo is considered. Figure 4.2 presents the photo, the numbers of joints and the numbers of frames of Romeo. The height of Romeo is 1.46m and weight is 40.8kg. This robot has 31 joints, i.e. 31 DoF. In the complete model, the mass and inertia of each link is modeled, and the actuator inertias are also included. The reference frame is situated at the projection of the ankle on the sole. The robot is composed of four kinematic chains:

— The left leg: frame 0 to 14;
— The head: frame 0 to 7, frame 15 to 20;
— The right arm: frame 0 to 7, frame 15, frame 21 to 28;
— The left arm: frame 0 to 7, frame 15, frame 29 to 36

For the robot Romeo, the vertical CoM motion, the swing foot, the torso and the upper-body joints are chosen as controlled variables, i.e.

$$q_c = [z_c, x_s, y_s, z_s, \psi_s, \theta_s, \varphi_s, \psi_t, \theta_t, \varphi_t, q_{13}, ..., q_{31}]^\top,$$

where z_c is the height of the CoM of the robot, $x_s, y_s, z_s, \psi_s, \theta_s, \varphi_s$ are the position and orientation of the swing foot (roll, pitch and yaw) [1], $\psi_t, \theta_t, \varphi_t$ are the orientation of the lower torso (the orientation of the hip), and q_{13} to q_{31} are the upper-body joints.

Three cases under different scenarios are simulated with the Essential Model to show its effectiveness and advantages:

— The trajectories of the controlled variables are defined as functions of time. The vertical velocity of the swing foot before landing is zero, thus no impact is involved in this case. Fixed location of the ZMP is desired for all the steps. i.e. $(p_x^d, p_y^d) = (0, 0)$ with respect to Σ_0. By considering a constant vertical CoM position, a comparison with the 3D LIP model is carried out.
— Virtual constraints define the trajectories of the controlled variables q_c^d and an impact of the swing foot with the ground is considered to build an Essential Model where the ZMP is kept in the same fixed desired position as in the previous case.
— Virtual constraints define the trajectories of the controlled variables q_c^d and an impact of the swing foot with the ground is considered. A different upper body

1. Roll: turn around x axis. Pitch: turn around y axis. Yaw: turn around z axis.

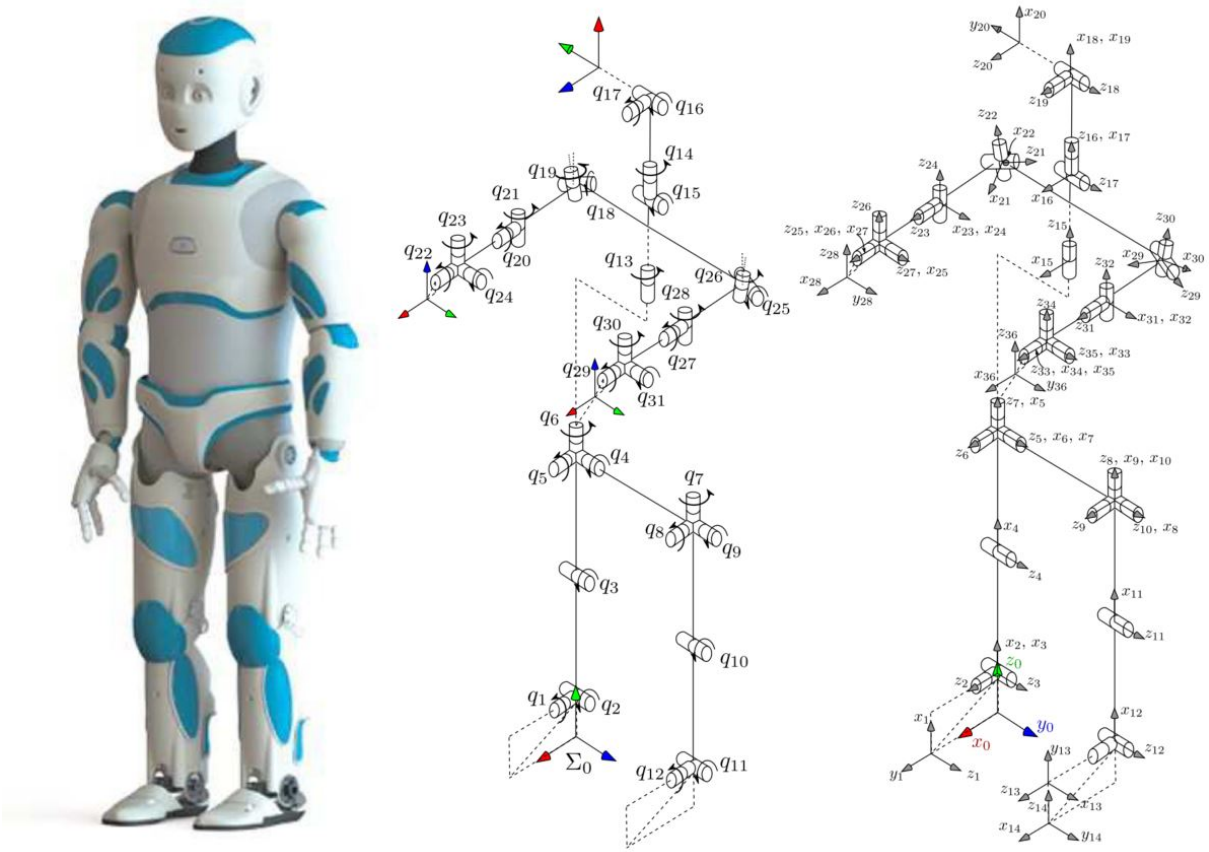

Figure 4.2 – The model of humanoid robot Romeo.

motion and a desired trajectory for the ZMP are considered.

4.5.2 Relabeling of Romeo

For the humanoid robot Romeo, the leg joints for the new coordinate system are defined by:

$$q^+(1:12) = E_{r1}q^-(1:12) \tag{4.43}$$

where

$$E_{r1} = \begin{bmatrix} 0 & 0 & 0 & 0 & 0 & 0 & 0 & 0 & 0 & 0 & 0 & 1 \\ 0 & 0 & 0 & 0 & 0 & 0 & 0 & 0 & 0 & 0 & -1 & 0 \\ 0 & 0 & 0 & 0 & 0 & 0 & 0 & 0 & 0 & -1 & 0 & 0 \\ 0 & 0 & 0 & 0 & 0 & 0 & 0 & 0 & -1 & 0 & 0 & 0 \\ 0 & 0 & 0 & 0 & 0 & 0 & 0 & 1 & 0 & 0 & 0 & 0 \\ 0 & 0 & 0 & 0 & 0 & 0 & 1 & 0 & 0 & 0 & 0 & 0 \\ 0 & 0 & 0 & 0 & 0 & 1 & 0 & 0 & 0 & 0 & 0 & 0 \\ 0 & 0 & 0 & 0 & 1 & 0 & 0 & 0 & 0 & 0 & 0 & 0 \\ 0 & 0 & 0 & -1 & 0 & 0 & 0 & 0 & 0 & 0 & 0 & 0 \\ 0 & 0 & -1 & 0 & 0 & 0 & 0 & 0 & 0 & 0 & 0 & 0 \\ 0 & -1 & 0 & 0 & 0 & 0 & 0 & 0 & 0 & 0 & 0 & 0 \\ 1 & 0 & 0 & 0 & 0 & 0 & 0 & 0 & 0 & 0 & 0 & 0 \end{bmatrix} \tag{4.44}$$

The torso, neck and head joints for the new coordinate system are defined by:

$$q^+(13:17) = E_{r2} q^-(13:17) \tag{4.45}$$

where

$$E_{r2} = \begin{bmatrix} -1 & 0 & 0 & 0 & 0 \\ 0 & -1 & 0 & 0 & 0 \\ 0 & 0 & 1 & 0 & 0 \\ 0 & 0 & 0 & 1 & 0 \\ 0 & 0 & 0 & 0 & 1 \end{bmatrix} \tag{4.46}$$

The arm joints for the new coordinate system are defined by:

$$q^+(18:31) = E_{r3} q^-(18:31) \tag{4.47}$$

where

$$E_{r3} = \begin{bmatrix} 0 & 0 & 0 & 0 & 0 & 0 & 0 & 1 & 0 & 0 & 0 & 0 & 0 & 0 \\ 0 & 0 & 0 & 0 & 0 & 0 & 0 & 0 & -1 & 0 & 0 & 0 & 0 & 0 \\ 0 & 0 & 0 & 0 & 0 & 0 & 0 & 0 & 0 & -1 & 0 & 0 & 0 & 0 \\ 0 & 0 & 0 & 0 & 0 & 0 & 0 & 0 & 0 & 0 & -1 & 0 & 0 & 0 \\ 0 & 0 & 0 & 0 & 0 & 0 & 0 & 0 & 0 & 0 & 0 & -1 & 0 & 0 \\ 0 & 0 & 0 & 0 & 0 & 0 & 0 & 0 & 0 & 0 & 0 & 0 & -1 & 0 \\ 0 & 0 & 0 & 0 & 0 & 0 & 0 & 0 & 0 & 0 & 0 & 0 & 0 & 1 \\ 1 & 0 & 0 & 0 & 0 & 0 & 0 & 0 & 0 & 0 & 0 & 0 & 0 & 0 \\ 0 & -1 & 0 & 0 & 0 & 0 & 0 & 0 & 0 & 0 & 0 & 0 & 0 & 0 \\ 0 & 0 & -1 & 0 & 0 & 0 & 0 & 0 & 0 & 0 & 0 & 0 & 0 & 0 \\ 0 & 0 & 0 & -1 & 0 & 0 & 0 & 0 & 0 & 0 & 0 & 0 & 0 & 0 \\ 0 & 0 & 0 & 0 & -1 & 0 & 0 & 0 & 0 & 0 & 0 & 0 & 0 & 0 \\ 0 & 0 & 0 & 0 & 0 & -1 & 0 & 0 & 0 & 0 & 0 & 0 & 0 & 0 \\ 0 & 0 & 0 & 0 & 0 & 0 & 1 & 0 & 0 & 0 & 0 & 0 & 0 & 0 \end{bmatrix} \tag{4.48}$$

Thus the relabeling of joints is given by:

$$q^+ = E_r q^- \tag{4.49}$$

where

$$E_r = \begin{bmatrix} E_{r1} & 0_{12\times5} & 0_{12\times14} \\ 0_{5\times12} & E_{r2} & 0_{5\times14} \\ 0_{14\times12} & 0_{14\times5} & E_{r3} \end{bmatrix} \tag{4.50}$$

4.5.3 The desired trajectories of the controlled variables

The desired evolutions of the controlled variables are defined as functions of a phasing variable Φ based on the internal states of the robot or time. The phasing variable Φ varies from 0 to 1 during one step.

The motion of CoM

The desired vertical motion of the CoM is defined by using a 5^{th} order polynomial function with the following boundary conditions

$$\begin{aligned} z_c^d(\Phi_0) &= z_0, & z_c^d(\Phi_m) &= z_0 + \alpha_z, & z_c^d(\Phi_f) &= z_0 \\ \dot{z}_c^d(\Phi_0) &= \dot{q}_{c,1} & \dot{z}_c^d(\Phi_m) &= 0 & \dot{z}_c^d(\Phi_f) &= v_m \end{aligned} \tag{4.51}$$

where $\dot{q}_{c,1}(q^+, \dot{q}^+)$ is the vertical velocity of the CoM after the transition of stance foot [2], and $\Phi_0 < \Phi_m < \Phi_f$ is an intermediate value which in this case is chosen as $\Phi_m = 0.6$. The values of z_0, α_z and v_m chosen for different cases are shown in Table 4.3. Note that when the height of the CoM is constant (Case I), the coefficients of the elements containing the phasing variable are zero, and the polynomial function for the motion of the CoM becomes constant.

Table 4.1 – Gait parameters for the 3D LIP and Essential models for robot Romeo

Parameter		Romeo			Description
[unit]		Case I	Case II	Case III	
S	[m]	0.3	0.3	0.3	Step length
D	[m]	0.15	0.15	0.15	Step width
v_s	[m/s]	0	-0.05	-0.05	Desired landing velocity
T	[s]	0.5	0.6	0.6	Step time
h_s	[m]	0.03	0.05	0.05	Max. swing foot amplitude
$\varphi_{f,0}$	[deg]	0	0	0	Free foot initial rotation
$\varphi_{f,f}$	[deg]	0	0	0	Free foot final rotation
g	[m/s^2]	9.81	9.81	9.81	Gravity acceleration
z_0	[m]	0.65	0.6	0.6	Height of the CoM
α_z	[m]	0	0.03	0.03	Max. CoM amplitude
v_m	[m/s]	0	-0.1	-0.1	Desired vertical CoM velocity at transition

The desired motion of the swing foot

It is desired that the swing foot lands on the ground with a zero velocity or a negative velocity. When the vertical velocity of the swing foot at landing is negative, the contact with the ground is ensured when the swing foot touches it. A 5^{th} order polynomial function is used to define the vertical evolution of the swing foot, by accomplishing the following

2. $\dot{q}_{c,i}$ is the i-element of the time derivative of q_c which is defined at the beginning of Section 4.5.

boundary conditions

$$\begin{aligned} z_s^d(\Phi_0) &= 0 & z_s^d(\Phi_m) &= h_s & z_s^d(\Phi_f) &= 0 \\ \dot{z}_s^d(\Phi_0) &= \dot{q}_{c,4} & \dot{z}_s^d(\Phi_m) &= 0 & \dot{z}_s^d(\Phi_f) &= v_s \end{aligned} \tag{4.52}$$

where $\dot{q}_{c,4}(q^+, \dot{q}^+)$ is the vertical velocity of the swing foot after impact [3].

For the horizontal motion of the swing foot, 3^{rd} order polynomials are used with following boundary conditions:

$$\begin{aligned} x_s^d(\Phi_0) &= x_{s0} & x_s^d(\Phi_f) &= x_{sf} \\ \dot{x}_s^d(\Phi_0) &= \dot{q}_{c,2} & \dot{x}_s^d(\Phi_f) &= 0 \\ y_s^d(\Phi_0) &= y_{s0} & y_s^d(\Phi_f) &= y_{sf} \\ \dot{y}_s^d(\Phi_0) &= \dot{q}_{c,3} & \dot{y}_s^d(\Phi_f) &= 0 \end{aligned} \tag{4.53}$$

where $\dot{q}_{c,2}(q^+, \dot{q}^+)$ and $\dot{q}_{c,3}(q^+, \dot{q}^+)$ are the horizontal velocities in X and Y direction of the swing foot respectively. The initial and final values of the swing foot $[x_{s0}; y_{s0}]$ and $[x_{sf}; y_{sf}]$ are always measured with respect to the support foot, i.e. $[x_{s0}; y_{s0}] = [-S; D]$ and $[x_{sf}; y_{sf}] = [S; D]$ respectively. The swing foot orientation is kept constant and parallel to the ground all the time. The parameters for the swing foot motion are shown in Table 4.3.

The upper body motion

For the desired trajectories of the controlled variables for the upper body $q_{c,i}^d$ with $i = 8, \ldots, 29$, 3^{rd} order polynomial functions are used with the following boundary conditions:

$$\begin{aligned} q_{c,i}^d(\Phi_0) &= k_i & q_{c,i}^d(\Phi_f) &= k_i \\ \dot{q}_{c,i}^d(\Phi_0) &= \dot{q}_{c,i} & \dot{q}_{c,i}^d(\Phi_f) &= 0 \end{aligned} \tag{4.54}$$

where $\dot{q}_{c,i}(q^+, \dot{q}^+)$ is the velocity of the controlled variable i after impact, and k_i is the i-element of k whose elements are zero except for the ones defined in Table 4.4.

When the upper body is kept constant, the polynomial functions for the upper body become constant values, as shown in Table 4.4.

3. Since there is a change of support, this velocity corresponds to the foot that was used as support in the previous step

Table 4.2 – Upper-body parameters for Romeo (Unit: rad)

Description	Romeo			
		Cases I & II	Case III	
	label	$k_{0,i}$	$k_{0,i}$	$k_{f,i}$
Torso yaw	$q^d_{c,10}$	0	0.1745	-0.1745
Torso pitch	$q^d_{c,9}$	0.08	0.08	0.08
R. shoulder pitch	$q^d_{c,16}$	1.8	1.9199	1.4835
R. shoulder yaw	$q^d_{c,17}$	0.2	0.2	0.2
R. elbow roll	$q^d_{c,18}$	1.9	1.9	1.9
R. elbow yaw	$q^d_{c,19}$	0.3	0.3491	0.7854
L. shoulder pitch	$q^d_{c,23}$	1.8	1.9199	1.4835
L. shoulder yaw	$q^d_{c,24}$	-0.2	-0.2	-0.2
L. elbow roll	$q^d_{c,25}$	-1.9	-1.9	-1.9
L. elbow yaw	$q^d_{c,26}$	-0.3	-0.7854	-0.3491

4.5.4 Case I: The Essential Model closest to the 3D LIP model

In order to show the efficiency of the Essential Model with respect to the 3D LIP model to generate walking gaits, in this section two walking gaits obtained by using these two models are compared. As known, the 3D LIP model only considers the global CoM position of the robot, not its mass distribution and inertias. On the other hand, the Essential Model takes into account the dynamic characteristics of the robot. Consequently, in order to compare the 3D LIP model and the Essential Model under the same conditions, it has been chosen:

— To consider a constant height of the CoM. Therefore, the gait parameters chosen for both models are shown in Table 4.3 (Case I).

— To consider a fixed step length, fixed step width and fixed step time to perform the gait.

— The evolution of the swing foot as a function of time, i.e. $\Phi = t/T$, in order to ensure the step is performed at a fixed step time.

— To define the trajectories of the swing foot with a zero vertical velocity before landing in order to avoid impacts since the 3D LIP model does not consider them.

— To test the obtained periodic motions of both models in the complete model of Romeo by considering the same swing foot motion and fixed upper body.

In this case only time is used to define the desired trajectories for the controlled variables i.e. $q^d_c(t) = [z_0,\ x^d_s(t),\ y^d_s(t),\ z^d_s(t),\ k^\top]^\top$, where the elements of $k \in \mathbb{R}^{25}$ are zero

except for the ones in Table 4.4. Therefore, $\vartheta = [x_c,\ y_c,\ t]^\top$. The desired position of the ZMP is $(p_x^d, p_y^d) = (0, 0)$ with respect to Σ_0. Then, the evolution of the joints can be found as a function of x_c, y_c and t. Later, by using the procedure in Section 4.3.3 the Essential Model is computed.

Numerical comparison

By using the gait parameters described previously, the fixed value for the 3D LIP model is:

$$\begin{aligned} x_c^{*-} &= [\frac{S}{2},\ \frac{D}{2},\ \dot{x}_c^{*-},\ \dot{y}_c^{*-}]^\top \\ &= [0.15 \text{ m},\ 0.075 \text{ m},\ 0.777764 \text{ m/s},\ 0.218303 \text{ m/s}]^\top, \end{aligned}$$

while the fixed value for the Essential Model is:

$$\begin{aligned} x_c^{*-} &= [\frac{S}{2} + D_x,\ \frac{D}{2} + Dy,\ \dot{x}_c^{*-},\ \dot{y}_c^{*-}]^\top \\ &= [0.153232 \text{ m},\ 0.075386 \text{ m},\ 0.730056 \text{ m/s},\ 0.189840 \text{ m/s}]^\top, \end{aligned}$$

The fixed values are slightly different between the 3D LIP model and the Essential Model because the motion of the swing foot and upper body will affect the periodic motion.

For this case, the motion performed by the robot Romeo for both models is visually similar and it is illustrated in Figure 4.3 where a simulation of three steps is shown. A video of the walking gait performed by Romeo in simulation for Case I is found in [105]. In order to see the difference between the two produced gaits Figs. 4.4 and 4.5 are plotted. Figure 4.4 shows that the spatial evolutions of the CoM of both models are close, but the amplitude along y of the 3D LIP Model is larger than that of the Essential Model for a same step duration. On the other hand, the velocity of the CoM is plotted in Figure 4.5. It can be noticed that the variation of the velocity for the Essential Model is smaller than the 3D LIP model. Finally, Figure 4.6 shows a comparison of the evolution of the ZMP by using the walking gaits obtained by each model. This plot clearly shows the advantage of the Essential Model. For a motion used in this case, the 3D LIP model produces walking gaits where the ZMP evolves outside of the convex hull of support when they are replicated by the complete model of the humanoid robot. Therefore, some

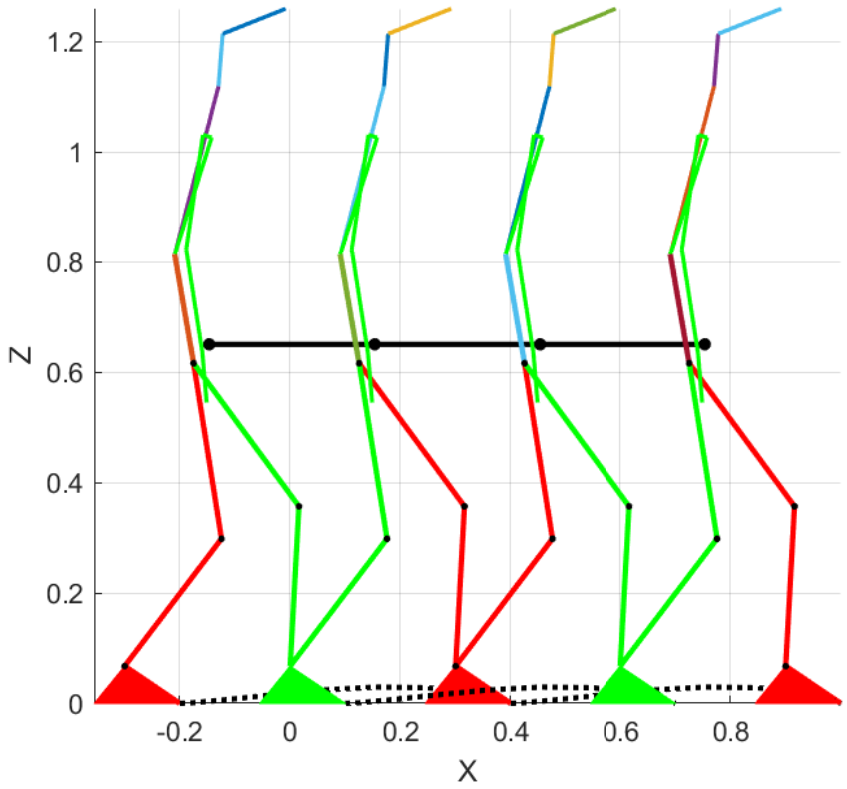

Figure 4.3 – Sequence of steps performed by the robot Romeo for Case I

complementary techniques [2, 4] must be taken into account to adjust the evolution of the joints of the robot, in order to at least keep the ZMP into a place inside the convex hull of support. Instead, by using the Essential Model, since the dynamics of the robot is taken into account the produced walking gaits will be always not only inside the support area, but in the desired location. These results suggest that by using a feedback control to track q_c^d the experimental tests can have good performance if the dynamic model of the robot describes accurately the real prototype.

4.5.5 Case II: As function of phasing variable with a constant ZMP

In order to have a motion that is more close to the walking gait of human beings, in this case, the vertical oscillation of the CoM is considered. The swing foot landing velocity is no longer null, thus the impact must be integrated into the Essential Model.

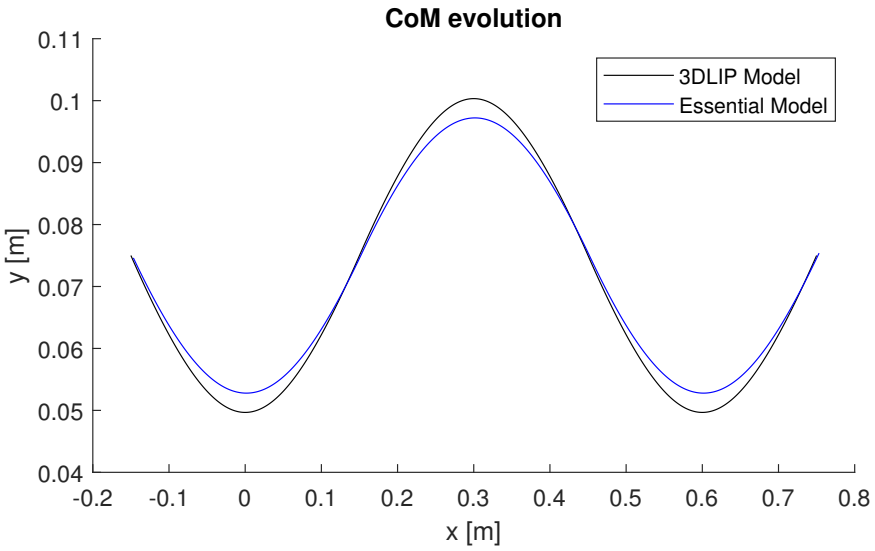

Figure 4.4 – Comparison of two steps of the evolution of the CoM for the gaits obtained with the 3D LIP model and the Essential Model, respectively.

The gait parameters for this case is shown in Table 4.3. The upper body is kept upright as shown in Table 4.4. Here, the performance of Essential Model that depends on the internal states of the robot is analyzed, i.e. the controlled variables are defined by virtual constraints based on the internal states instead of time. It has been proven that when the trajectories of controlled variables are defined as functions of the quadratic combination of the horizontal CoM position x and y, self-stabilized or self-synchronized walking gaits can be achieved. The same phasing variable

$$\Phi = a_1 x_c + a_2 y_c + a_3 x_c y_c + a_4 x_c^2 + a_5 y_c^2 + a_6 \tag{4.55}$$

is used such that the robot switches its stance leg when the CoM crosses the switching manifold

$$\mathbf{S} = \{(x_c, y_c, z_c) | (x_c - x_c^{*-}) + C(y_c - y_c^{*-}) = 0\} \tag{4.56}$$

as in Chapters 2 and 3, where C is a parameter that characterizes the orientation of the switching manifold. For a periodic motion, $\Phi_0 = 0$ at the beginning of a step, and $\Phi_f = 1$ at the end of a step.

In this case the trajectories for the controlled variables are defined as a function of $\Phi(x_c, y_c)$, i.e. $q_c^d(\Phi) = [z_c(\Phi),\ x_s^d(\Phi),\ y_s^d(\Phi),\ z_s^d(\Phi),\ q_{c,5}(\Phi), \cdots, q_{c,29}(\Phi)]^\top$, and $\vartheta = q_f = [x_c,\ y_c]^\top$. The desired position of the ZMP is $(p_x^d, p_y^d) = (0, 0)$ with respect to Σ_0 as in

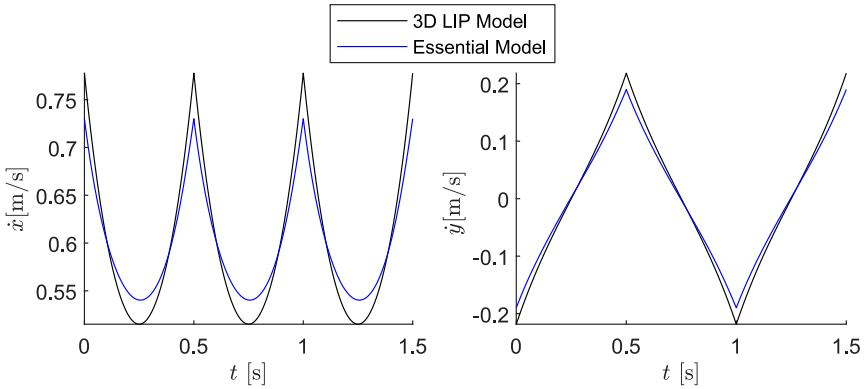

Figure 4.5 – Comparison of two steps of the velocity of the CoM with respect to time for the gaits obtained with the 3D LIP model and the Essential Model, respectively.

the previous case. Then, by following the procedure in Section 4.3.2 the evolution of the joints can be found as a function of x and y, and the Essential Model is computed.

Numerical results

By using the gait parameters shown in Table 4.3 and the upper-body configuration for Romeo shown in Table 4.4 the periodic motion is defined by

$$\begin{aligned} x_c^{*-} &= [\frac{S}{2} + D_x,\ \frac{D}{2} + D_y,\ \dot{x}_c^{*-},\ \dot{y}_c^{*-}]^\top \\ &= [0.152094 \text{ m},\ 0.077590 \text{ m},\ 0.644252 \text{ m/s},\ 0.230389 \text{ m/s}]^\top. \end{aligned}$$

The schematic illustration of three steps is shown in Figure 4.7. It shows the starting and ending configuration of each step. The trajectory of the CoM is highlighted with black solid curve, where its oscillatory vertical motion is noted. The upper body posture is fixed. A video of the walking gait performed by Romeo in simulation for this case is found in [106]. The evolution of the CoM is given by Figure 4.8. The CoM trajectories are represented by the solid curves while the dashed lines connect the CoM and the ZMP at the beginning and ending of each step. The ZMP is represented by a circle and a cross respectively at the beginning and ending of a step. In Figure 4.8, the circle and cross coincide at the zero position as expected. The projections of the CoM trajectory in horizontal, sagittal and frontal planes are shown in Figure 4.8. In the horizontal plane of Figure 4.8, the switching manifold of each step is represented by the solid blue lines. The

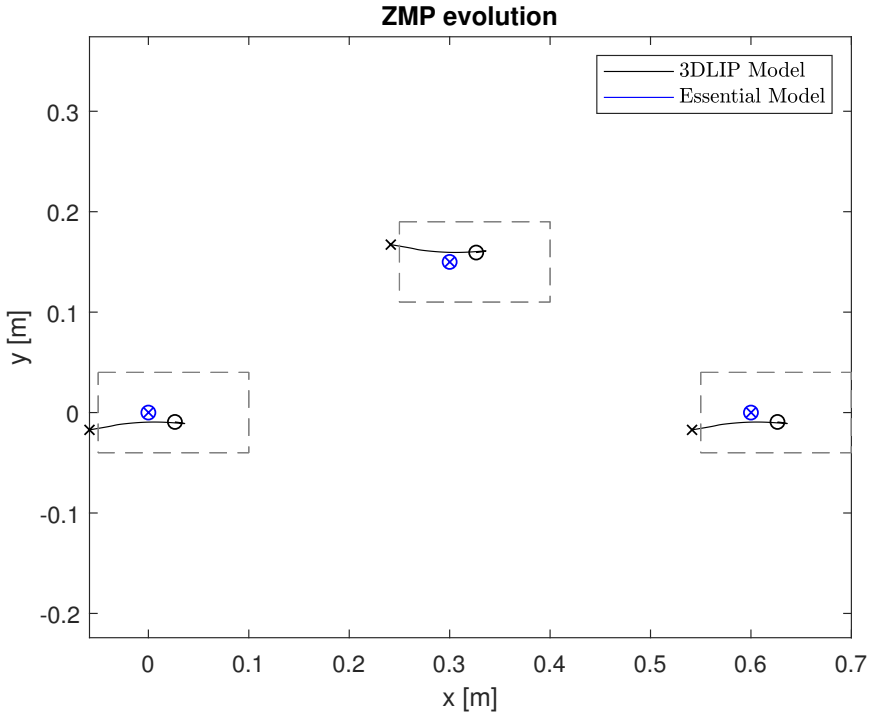

Figure 4.6 – Comparison of the evolution of the ZMP for the gaits obtained with the 3D LIP model and the Essential Model respectively. It is shown how the gait obtained with the Essential Model makes the ZMP be kept in the desired location during all the walking gait. The circles and crosses denote the initial and final points of the ZMP, respectively.

position of the CoM at the end of each step is located inside of this switching manifold.

4.5.6 Case III: As function of the phasing variable with a varying ZMP

In this case, a walking gait that tracks exactly a user-defined trajectory of ZMP is developed. The definition of the trajectories of the controlled variables is the same as in case II, i.e. as functions of a phasing variable proposed in Chapters 2 and 3. The same switching strategy as in the second case is used. Thus the Essential Model for case III is also the same as case II. Different from case II, the upper body motion in case III is considered to be human-like, i.e. with the swing of the arms and turning of the torso.

The desired motion of the ZMP

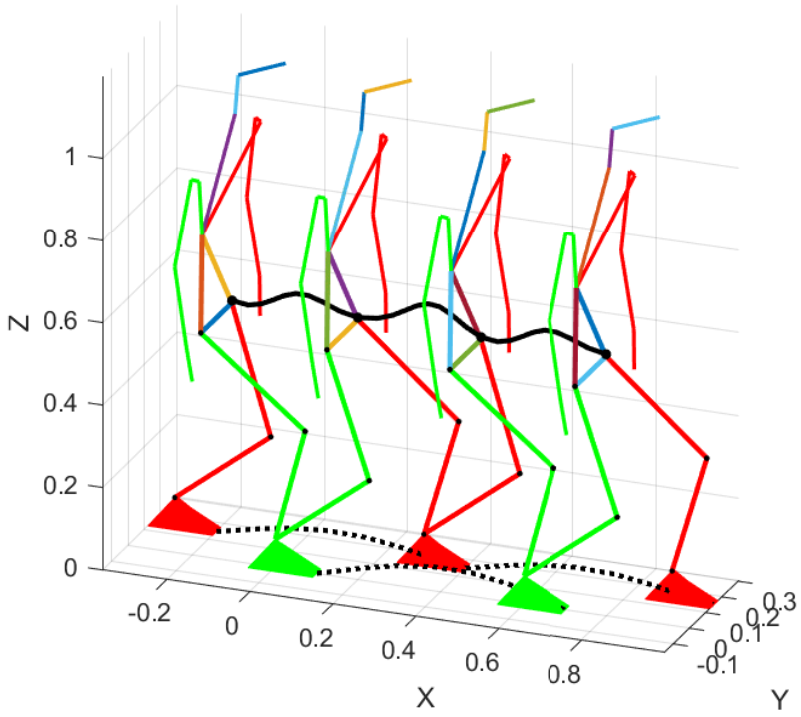

Figure 4.7 – Illustration of 3 steps for Case II.

Unlike Cases I and II where a fixed position of the ZMP was desired, a varying ZMP trajectory while the robot performs a step is proposed in here. Several studies on the evolution of ZMP for a human walking gait, such as [107–109] can be used with the Essential Model in order to develop human-like walking gaits.

In this case, 3^{rd} order polynomial functions are used in order to build a desired trajectory of the ZMP in x and y directions, with the following boundary conditions:

$$p_x^d(\Phi_0) = p_{x0} \qquad p_x^d(\Phi_f) = p_{xf}$$
$$\dot{p}_x^d(\Phi_0) = 0 \qquad \dot{p}_x^d(\Phi_f) = 0,$$

and

$$p_y^d(\Phi_0) = p_{y0} \qquad p_y^d(\Phi_f) = p_{yf}$$
$$\dot{p}_y^d(\Phi_0) = 0 \qquad \dot{p}_y^d(\Phi_f) = 0$$

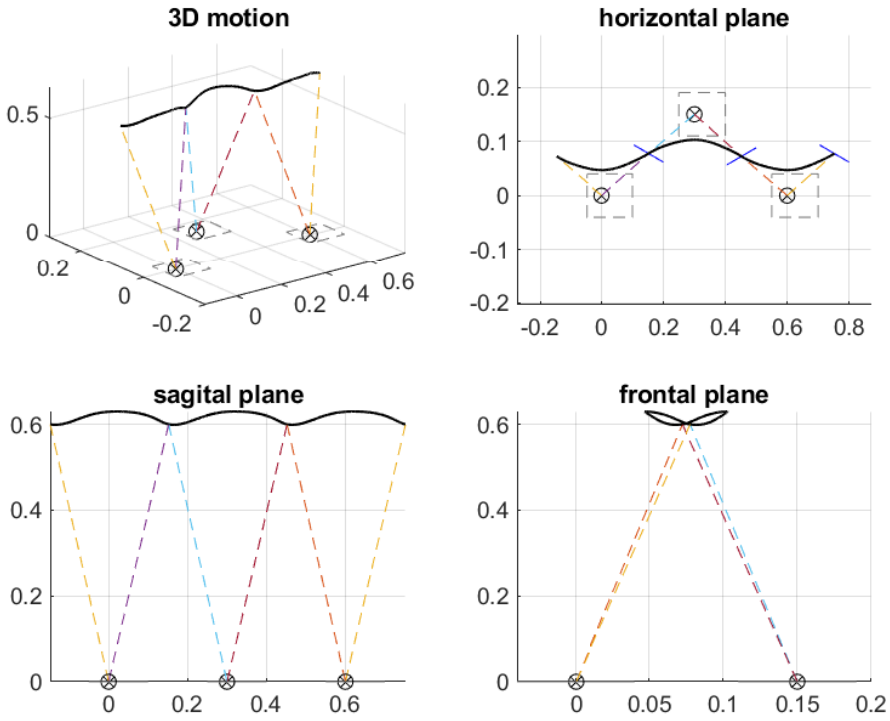

Figure 4.8 – Evolution of the CoM in 3D space and its projections in horizontal, sagittal and frontal planes for Case II.

where $p_{x0} = -0.01$ m, $p_{xf} = 0.08$ m, are the initial and final desired positions of the ZMP in x direction with respect to the support frame Σ_0, and $p_{y0} = p_{yf} = 0.02$ m, are the initial and final positions of the ZMP in y direction with respect to the frame Σ_0.

Numerical results

By using the gait parameters shown in Table 4.3 and the upper-body configuration for Romeo shown in Table 4.4 the periodic motion is defined by

$$\begin{aligned} x_c^{*-} &= [\frac{S}{2} + D_x,\ \frac{D}{2} + D_y,\ \dot{x}_c^{*-},\ \dot{y}_c^{*-}]^\top \\ &= [0.189018 \text{ m},\ 0.076592 \text{ m},\ 0.573714 \text{ m/s},\ 0.166289 \text{ m/s}]^\top. \end{aligned}$$

The schematic illustration of three steps is shown in Figure 4.9. It shows the starting and ending configuration of each step. It can be observed that the two arms swing alternately step after step, and the hip turns around the vertical axis as human beings

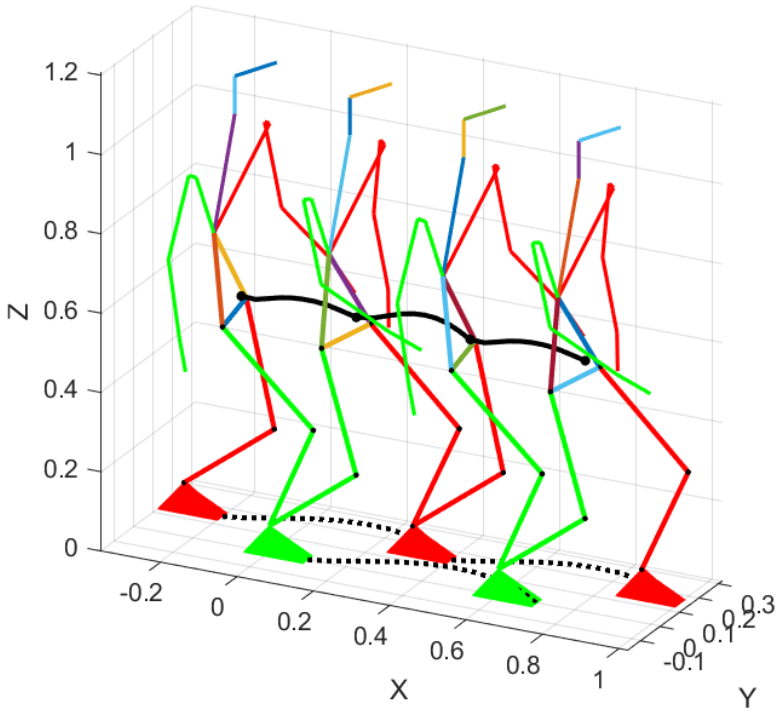

Figure 4.9 – Illustration of 3 steps for Case III.

do. A video of the walking gait performed by Romeo in simulation for this case is found in [110]. The evolution of the CoM is given by Figure 4.10. The CoM trajectories are represented by the solid curves while the dashed lines connect the CoM and the ZMP at the beginning and ending of each step. The ZMP is represented by a circle and a cross respectively at the beginning and ending of a step. It can be seen that the ZMP starts from the position $[p_{x0}, p_{y0}] = [-0.01, 0.02]$ m, follows a desired trajectory, and stop at the position $[p_{xf}, p_{yf}] = [0.08, 0.02]$ m as expected. The projections of the CoM trajectory in horizontal, sagittal and frontal planes are also shown in Figure 4.10.

4.6 Case study: TALOS

4.6.1 Introduction of TALOS

In this section, the application of Essential Model proposed in this chapter is validated on TALOS, which is a full-size humanoid robot developed by PAL robotics [111] shown in

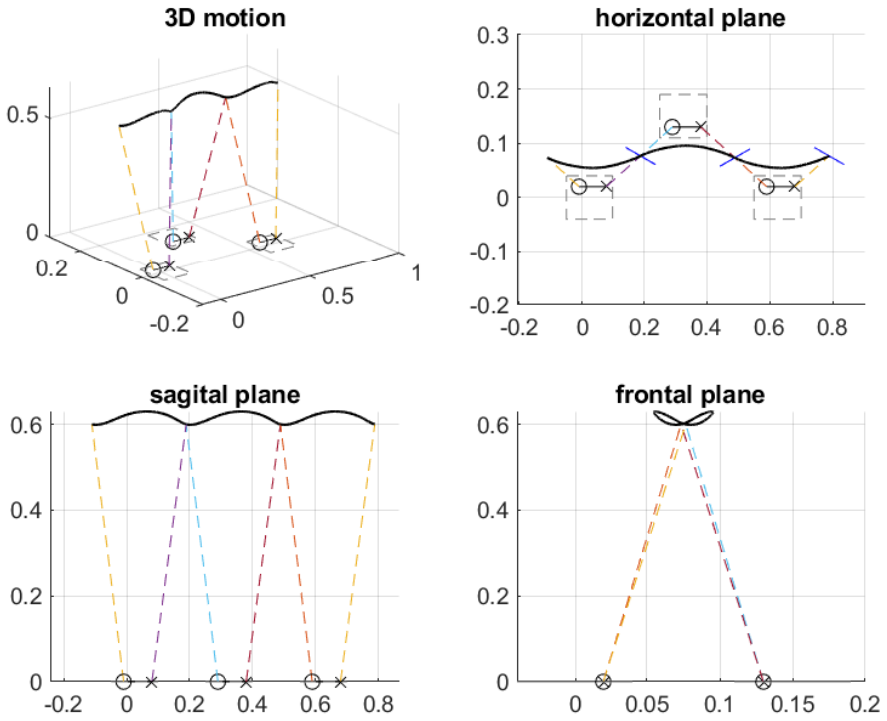

Figure 4.10 – Evolution of the CoM in 3D space and its projections in horizontal, sagittal and frontal planes for Case III.

Figure 4.11. TALOS has a height of 1.75 m and a weight of 95 kg. TALOS has 30 joints (shown in Figure 4.12), including 6 DoFs for each leg, 2 DoFs for the torso, 2 DoFs for the neck and head and 7 DoFs for each arm. The reference frame is located at the projection of the ankle at the sole. The 4 kinematic chains start from the support foot tip and end with swing foot tip, the head, the left and right arms. Several intermediate frames with null mass and inertial are set to facilitate the use of frames with chosen orientations.

4.6.2 Relabeling of TALOS

For the humanoid robot TALOS, the leg joints for the new coordinate system are defined by:

$$q^{+}(1:12) = E_{t1} q^{-}(1:12) \tag{4.57}$$

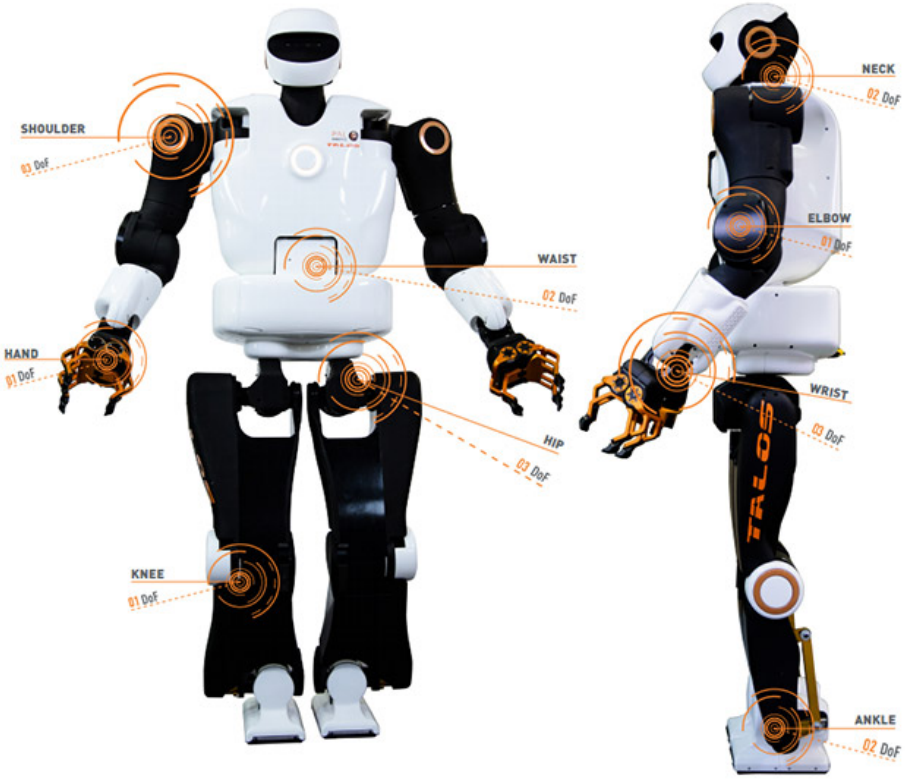

Figure 4.11 – Photo of TALOS.

where

$$E_{t1} = \begin{bmatrix} 0 & 0 & 0 & 0 & 0 & 0 & 0 & 0 & 0 & 0 & 0 & 1 \\ 0 & 0 & 0 & 0 & 0 & 0 & 0 & 0 & 0 & 0 & -1 & 0 \\ 0 & 0 & 0 & 0 & 0 & 0 & 0 & 0 & 0 & -1 & 0 & 0 \\ 0 & 0 & 0 & 0 & 0 & 0 & 0 & 0 & -1 & 0 & 0 & 0 \\ 0 & 0 & 0 & 0 & 0 & 0 & 0 & 1 & 0 & 0 & 0 & 0 \\ 0 & 0 & 0 & 0 & 0 & 0 & 1 & 0 & 0 & 0 & 0 & 0 \\ 0 & 0 & 0 & 0 & 0 & 1 & 0 & 0 & 0 & 0 & 0 & 0 \\ 0 & 0 & 0 & 0 & 1 & 0 & 0 & 0 & 0 & 0 & 0 & 0 \\ 0 & 0 & 0 & -1 & 0 & 0 & 0 & 0 & 0 & 0 & 0 & 0 \\ 0 & 0 & -1 & 0 & 0 & 0 & 0 & 0 & 0 & 0 & 0 & 0 \\ 0 & -1 & 0 & 0 & 0 & 0 & 0 & 0 & 0 & 0 & 0 & 0 \\ 1 & 0 & 0 & 0 & 0 & 0 & 0 & 0 & 0 & 0 & 0 & 0 \end{bmatrix} \tag{4.58}$$

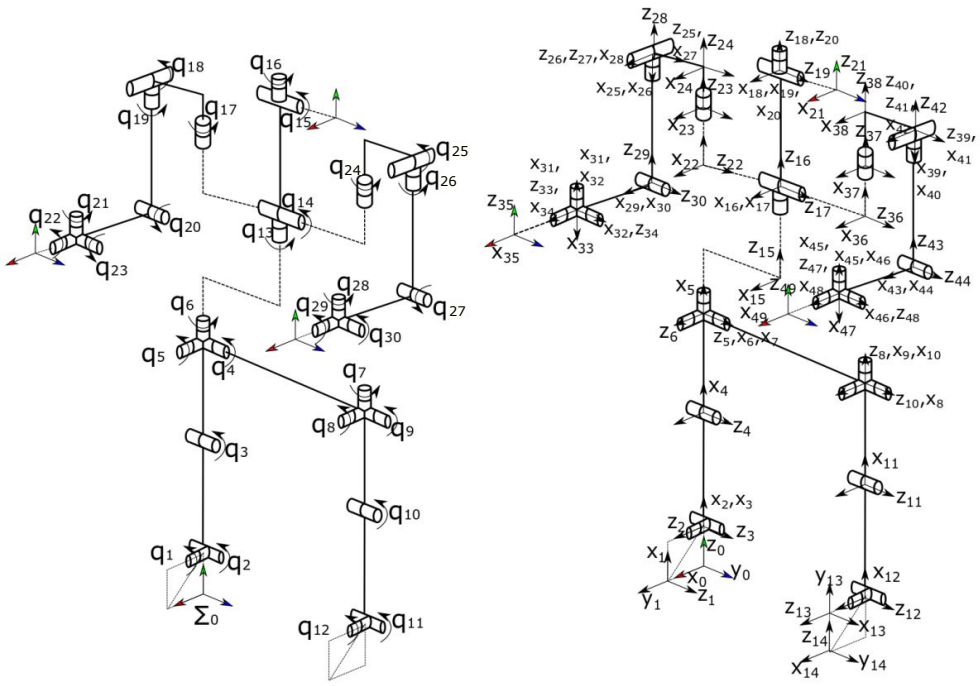

Figure 4.12 – Joints and frames of TALOS.

The torso, neck and head joints for the new coordinate system are defined by:

$$q^+(13:16) = E_{t2} q^-(13:16) \tag{4.59}$$

where

$$E_2 = \begin{bmatrix} -1 & 0 & 0 & 0 \\ 0 & 1 & 0 & 0 \\ 0 & 0 & 1 & 0 \\ 0 & 0 & 0 & -1 \end{bmatrix} \tag{4.60}$$

The arm joints for the new coordinate system are defined by:

$$q^+(17:30) = E_{t3} q^-(17:30) \tag{4.61}$$

where

$$E_{t3} = \begin{bmatrix} 0 & 0 & 0 & 0 & 0 & 0 & 0 & -1 & 0 & 0 & 0 & 0 & 0 & 0 \\ 0 & 0 & 0 & 0 & 0 & 0 & 0 & 0 & 1 & 0 & 0 & 0 & 0 & 0 \\ 0 & 0 & 0 & 0 & 0 & 0 & 0 & 0 & 0 & -1 & 0 & 0 & 0 & 0 \\ 0 & 0 & 0 & 0 & 0 & 0 & 0 & 0 & 0 & 0 & 1 & 0 & 0 & 0 \\ 0 & 0 & 0 & 0 & 0 & 0 & 0 & 0 & 0 & 0 & 0 & -1 & 0 & 0 \\ 0 & 0 & 0 & 0 & 0 & 0 & 0 & 0 & 0 & 0 & 0 & 0 & -1 & 0 \\ 0 & 0 & 0 & 0 & 0 & 0 & 0 & 0 & 0 & 0 & 0 & 0 & 0 & 1 \\ -1 & 0 & 0 & 0 & 0 & 0 & 0 & 0 & 0 & 0 & 0 & 0 & 0 & 0 \\ 0 & 1 & 0 & 0 & 0 & 0 & 0 & 0 & 0 & 0 & 0 & 0 & 0 & 0 \\ 0 & 0 & -1 & 0 & 0 & 0 & 0 & 0 & 0 & 0 & 0 & 0 & 0 & 0 \\ 0 & 0 & 0 & 1 & 0 & 0 & 0 & 0 & 0 & 0 & 0 & 0 & 0 & 0 \\ 0 & 0 & 0 & 0 & -1 & 0 & 0 & 0 & 0 & 0 & 0 & 0 & 0 & 0 \\ 0 & 0 & 0 & 0 & 0 & -1 & 0 & 0 & 0 & 0 & 0 & 0 & 0 & 0 \\ 0 & 0 & 0 & 0 & 0 & 0 & 1 & 0 & 0 & 0 & 0 & 0 & 0 & 0 \end{bmatrix} \tag{4.62}$$

Thus the relabeling of joints for TALOS is given by:

$$q^+ = E_t q^- \tag{4.63}$$

where

$$E_t = \begin{bmatrix} E_{t1} & 0_{12\times4} & 0_{12\times14} \\ 0_{4\times12} & E_{t2} & 0_{4\times14} \\ 0_{14\times12} & 0_{14\times4} & E_{t3} \end{bmatrix} \tag{4.64}$$

4.6.3 Motion of controlled variables

For the robot TALOS as shown in Figure 4.12, the vertical CoM motion, the swing foot, the torso and the upper-body joints are chosen as control variables, i.e.

$$q_c = [z_c, x_s, y_s, z_s, \psi_s, \theta_s, \varphi_s, \psi_t, \theta_t, \varphi_t, q_{13}, ..., q_{30}]^\top,$$

In this chapter, the swing foot velocity is not null, thus the impact between the swing foot and the ground must be considered. Due to the jump of joint velocities caused by the impact, the velocity of the CoM after the impact differs from that before the impact, thus needs to be measured at the beginning of each step. In this case, the controlled variables

are chosen as functions of the phasing variable depending on the horizontal position of the CoM as proposed in Chapters 2 and 3. The oscillation of the CoM of TALOS is considered, thus the evolution of the CoM is chosen to be a 5^{th} order polynomial function with boundary constraints given by equation (4.51). The desired motion of the swing foot along z axis is defined as a 5^{th} order polynomial function with boundary constraints given by equation (4.52). Similarly, the motions of the swing foot along x and y axes are defined as a 3^{th} order polynomial function with boundary constraints given by equation (4.53). The relevant parameters are given in Table 4.3. The upper body motion is chosen to be fixed with the values given in Table 4.4.

Table 4.3 – Gait parameters for the 3D LIP and Essential models

Parameter		Romeo			TALOS	Description
[unit]		I	II	III		
S	[m]	0.3	0.3	0.3	0.4	Step length
D	[m]	0.15	0.15	0.15	0.15	Step width
v_s	[m/s]	0	-0.05	-0.05	-0.1	Desired landing velocity
T	[s]	0.5	0.6	0.6	0.6	Step time
h_s	[m]	0.03	0.05	0.05	0.05	Max. swing foot amplitude
$\varphi_{f,0}$	[deg]	0	0	0	0	Free foot initial rotation
$\varphi_{f,f}$	[deg]	0	0	0	0	Free foot final rotation
g	[m/s^2]	9.81	9.81	9.81	9.81	Gravity acceleration
z_0	[m]	0.65	0.6	0.6	0.85	Height of the CoM
α_z	[m]	0	0.03	0.03	0.03	Max. CoM amplitude
v_m	[m/s]	0	-0.1	-0.1	-0.2	Desired vertical CoM velocity at transition

4.6.4 Numerical analysis

In this case, a varying evolution of the ZMP is chosen, which is a segment starting from $[p_{x0}; p_{y0}] = [-0.01; 0.02]$ m to $[p_{xf}; p_{yf}] = [0.08; 0.02]$ m. The periodic motion obtained for TALOS is:

$$\begin{aligned} x_c^{*-} &= [\frac{S}{2} + D_x,\ \frac{D}{2} + D_y,\ \dot{x}_c^{*-},\ \dot{y}_c^{*-}]^\top \\ &= [0.259423 \text{ m},\ 0.077754 \text{ m},\ 0.785532 \text{ m/s},\ 0.130012 \text{ m/s}]^\top. \end{aligned}$$

The motion is supposed to start with a periodic motion. The schematic illustration

Table 4.4 – Upper-body parameters for Romeo and TALOS (Unit: rad)

Description	Romeo				TALOS	
		I & II	III			
	label	$k_{0,i}$	$k_{0,i}$	$k_{f,i}$	label	$k_{0,i}$
Torso yaw	$q^d_{c,10}$	0	0.1745	-0.1745	$q^d_{c,10}$	0
Torso pitch	$q^d_{c,9}$	0.08	0.08	0.08	$q^d_{c,12}$	0.2
R. shoulder pitch	$q^d_{c,16}$	1.8	1.9199	1.4835	-	-
R. shoulder yaw	$q^d_{c,17}$	0.2	0.2	0.2	$q^d_{c,15}$	0
R. elbow pitch	-	-	-	-	$q^d_{c,18}$	-0.4
R. elbow roll	$q^d_{c,18}$	1.9	1.9	1.9	-	-
R. elbow yaw	$q^d_{c,19}$	0.3	0.3491	0.7854	-	-
L. shoulder pitch	$q^d_{c,23}$	1.8	1.9199	1.4835	-	-
L. shoulder yaw	$q^d_{c,24}$	-0.2	-0.2	-0.2	$q^d_{c,22}$	0
L. elbow pitch	-	-	-	-	$q^d_{c,25}$	-0.4
L. elbow roll	$q^d_{c,25}$	-1.9	-1.9	-1.9	-	-
L. elbow yaw	$q^d_{c,26}$	-0.3	-0.7854	-0.3491	-	-

of three steps for TALOS is shown in Figure 4.13. A fixed upper body and oscillated CoM trajectory can be observed. A video of the walking gait performed by TALOS is in simulation for this case is found in [112]. The CoM and ZMP trajectories of TALOS are highlighted in Figure 4.14, where its projection on horizontal, sagittal and frontal planes are shown. It can be seen that the ZMP starts from the expected initial position, follows a segment given by a 3^{rd} order polynomial function and ends at the expected final position, thus stays inside the convex hull of support, i.e. TALOS is able to perform these 3 steps and will not lose stability. The evolution of the state of the robot is shown in Figure 4.15. The evolution of the state for each step is the same because the motion is periodic and there is no perturbation.

4.7 Conclusion

The use of simple models, as the 3D LIP model, for building walking trajectories is useful. However, the vertical motion of the CoM is constrained and the ZMP is not kept to its desired location when the motion produced by the 3D LIP model is transplanted on the complete robot. Therefore, further techniques for keeping the ZMP inside the convex hull of support are usually carried out. In this chapter, a new model of the same dimension as the 3D LIP model, called Essential Model, has been proposed in order to deal with these

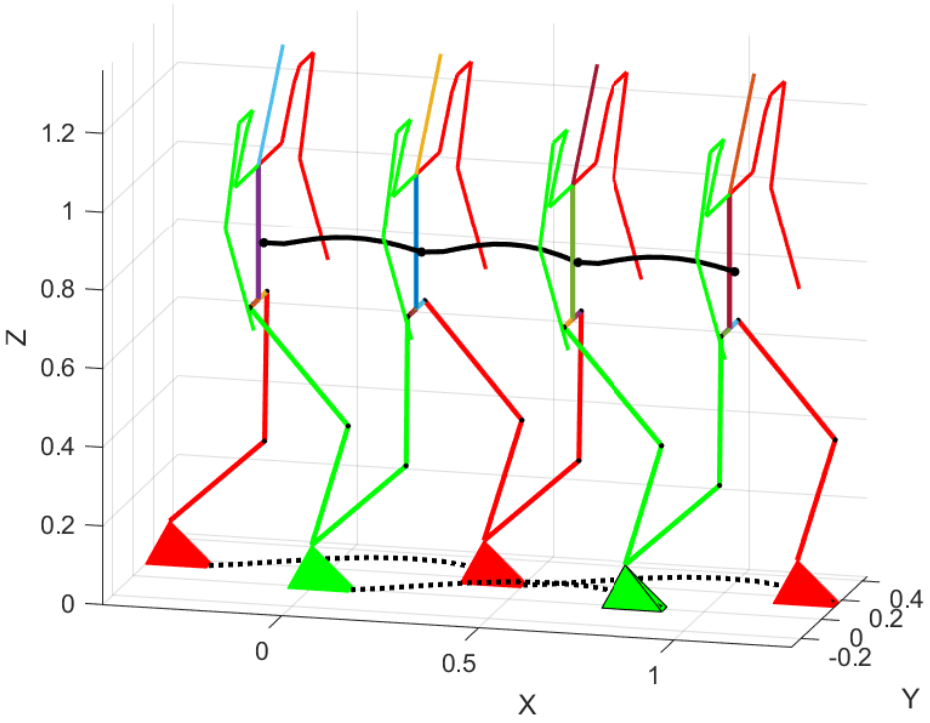

Figure 4.13 – Illustration of 3 steps for the robot TALOS.

difficulties. This model is developed by taking into account the whole dynamics of the robot and the behavior of the robot is given by the hybrid zero dynamics (HZD). Impacts of the swing foot with the ground can also be considered in the development of walking gaits. The dynamics of the Essential Model depend always on the internal states of the robot but can also depend on some external information (such as time). Assuming that a control law has been defined to follow perfectly the desired motion for a desired ZMP path such as [113], the Essential Model describes the robot motion in closed loop. In closed loop, the controlled variables q_c will have the desired behaviors but the evolution of the free variables, i.e. the horizontal position of the CoM, is unknown and must be studied. It will be done in the next chapter. The Essential Model has been used in this chapter to define periodic motions that satisfy imposed evolutions of the ZMP. This model can also be used to produce starting and stopping phases to complement the periodic motion as shown in [114] and to develop motions in double support phases. The Essential Model will be used in the next chapter to study the stability of walking gait.

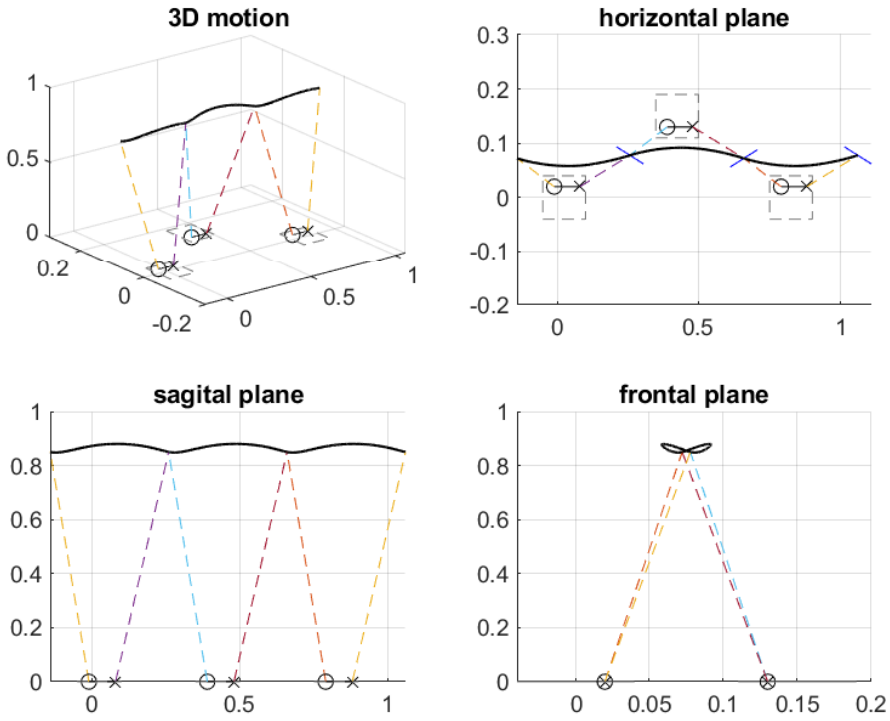

Figure 4.14 – TALOS CoM evoluction.

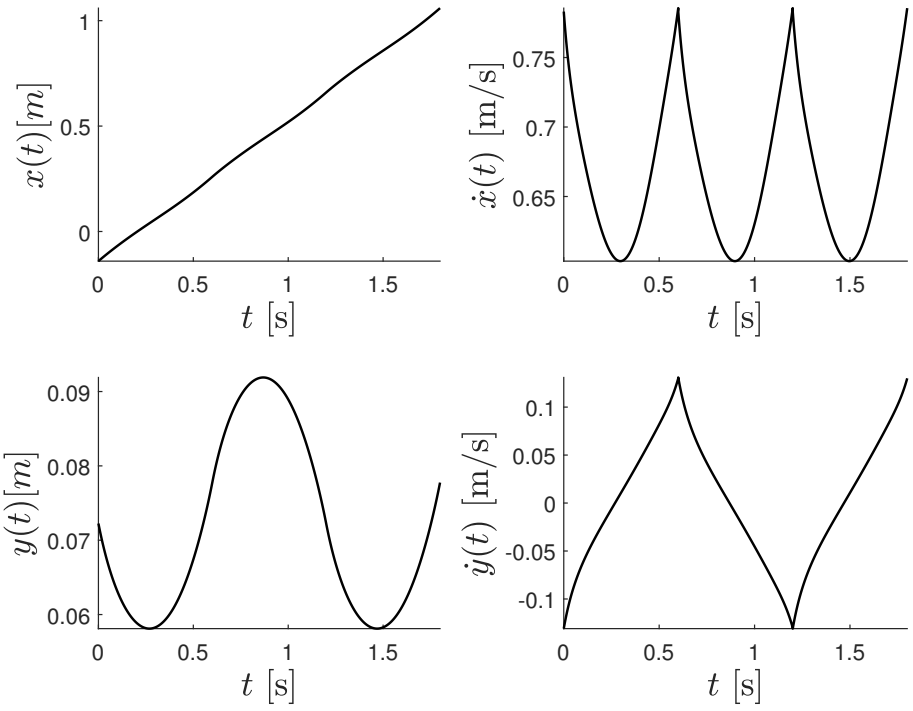

Figure 4.15 – TALOS state evolution.

Chapter 5

Stability analysis of essential model

For a complex hybrid system that is composed of a SS phase and an instantaneous DS phase, it is impossible to study the stability of a walking gait analytically. A practical method is to use Poincaré return map as introduced in Chapter 2. The eigenvalues of the Jacobian matrix of the Poincaré return map can be calculated numerically. It can be known from the numerical results that any eigenvalue with a norm bigger than one will lead to unstable system. It has been shown in Chapter 2 that for a LIP model, a self-synchronized walking gait can be obtained when the controlled variables are defined as functions of a phasing variable based on the horizontal position of the CoM. And Chapter 3 has proven that for a VLIP model, not only the definition of the swing foot trajectory, but also the vertical motion of the CoM is crucial for obtaining stability. In the previous chapters, the stability study has been done for simplified models. In this chapter, how these parameters (i.e. the swing foot motion, the vertical CoM motion, the switching manifold configuration etc.) affect the stability of the walking gait that considers the complete dynamics of the robot is discussed. Besides, how different walking postures and sizes of the robot affect the stability of the walking gait is also discussed. Since it has been proven in [6] and [115] that the stability properties of orbits of the hybrid restriction dynamics carry over to the full-dimensional dynamics, the essential model proposed in Chapter 4 is used in this chapter to analyze the stability of the walking gaits.

This chapter is structured as below. Section 5.1 analyzes several walking gaits with a control law that uses a reference motion expressed as a function of time and shows that this control law based on time is unstable. Section 5.2 analyzes the stability of cases when the phasing variable is based on the internal state of the robot, for different robots and different walking patterns. Simulations are carried out in Section 5.3 for robots Romeo and TALOS to validate the stability of the proposed walking algorithm on the essential model. The conclusion is made in Section 5.4.

5.1 Transition based on time

It has been proven in Chapter 2 that for a 3D LIP model, when the controlled variable (i.e. the swing foot motion) is defined with a phasing variable based on time, i.e. $\Phi = \frac{t}{T^*}$, the walking stability cannot be obtained with only a good tracking of the controlled variables. In order to discuss the influence of different walking patterns on the walking stability applied on the essential model and to compare with the results obtained for the cases when the phasing variable is based on the internal state of the robot, the eigenvalues of several cases when the phasing variable is based on time are calculated here.

The Jacobian matrix of the Poincaré return map at the fixed point is calculated numerically in the coordinate system $[x_c^-, y_c^-, \dot{x}_c^-, \dot{y}_c^-]^\top$, which is the state of the CoM just before the transition of stance leg. Since the study of stability has been done in a space of 4 dimensions, 4 eigenvalues can be calculated. The following characters of walking are analyzed: the vertical CoM motion characterized by v_m and z_0; the swing foot motion characterized by h_s and v_s; the landing position characterized by k_S and k_D. The humanoid robot Romeo is taken as an example here. The reference case (denoted by $Case_tR$) is chosen to have a constant height of CoM, no impact at landing ($v_S = 0$) and fixed step length and width ($k_S = k_D = 1$). The values of these parameters are shown in Table 5.1. For all the cases, a fixed upper-body motion that keeps the robot upright is used, and the step length and width are $S = 0.3$ m, $D = 0.15$ m. The following cases are studied to compare with the $Case_tR$:

— $Case_tI$ has a non-zero vertical swing foot velocity at landing, i.e. $v_s = -0.1$ m/s;
— $Case_tII$ has a landing position that nullifies the initial CoM position error at the beginning of each step, i.e. $k_S = k_D = 0$;
— $Case_tIII$ has a variable height of CoM along z axis. The magnitude of the variation is 0.03 m, while the vertical velocity of CoM before landing is -0.1 m/s.

The other parameters not mentioned above for each case are the same as $Case_tR$.

The maximum norms of the eigenvalues for different cases as functions of time are shown in Figure 5.1. It can be seen from Figure 5.1 that all of these cases with a reference motion that is based on time have at least one eigenvalue that is bigger than one, i.e. none of these cases is stable for any T between 0.3 s and 0.8 s. Compared with $Case_tR$, $Case_tII$ has smaller maximum norms of eigenvalues. This means that choosing $k_S = k_D = 0$ reduces significantly the maximum norm of the eigenvalues for all the values of T, but not enough to make the maximum norm of the eigenvalues smaller than 1. $Case_tI$ shows that

Table 5.1 – Parameters for simulation

	$Case_tR$	$Case_tI$	$Case_tII$	$Case_tIII$
v_m [m/s]	0	0	0	-0.1
z_0 [m]	0.65	0.65	0.65	0.65
a_z [m]	-	-	-	0.03
h_s [m]	0.05	0.05	0.05	0.05
v_s [m/s]	0	-0.1	0	0
k_S	1	1	0	1
k_D	1	1	0	1

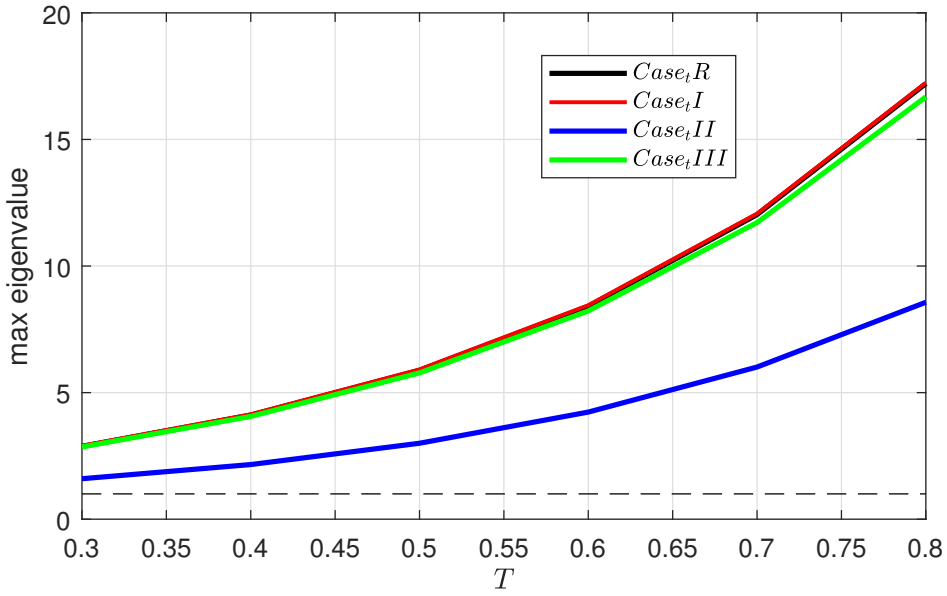

Figure 5.1 – The norms of maximum eigenvalues for different cases as functions of time. The dashed line represents the value 1.

the impact between the swing foot and the ground with a velocity of -0.1 m/s barely affects the stablity because the maximum norms of eigenvalues for this case almost overlap with those of $Case_tR$. The result of $Case_tIII$ shows that the vertical oscillation of the CoM with a negative velocity at transition has a larger influence on the eigenvalues than $Case_tII$ but much smaller than $Case_tII$.

5.2 Transition based on the internal state of the robot

When the controlled variables of the robot are defined as functions of the phasing variable based on the internal state of the robot, the phasing variable defined by equation (2.41) is used. Compared to the simplified models, the stability of the model that considers the complete dynamics of the robot is affected by more parameters. In this section, six groups of comparison will be done for the walking patterns : 1) with different landing positions defined by k_S and k_D as for the simplified model; 2) for robot Romeo and TALOS; 3) with a constant height and a variable height of the CoM; 4) with and without impact with the ground; 5) with and without swing of arms and torso; 6) with a constant ZMP and with a varying ZMP. Similar comparisons as in groups 1) and 3) have been studied for the simplified models, and the other groups can be studied only for complete models. The eigenvalues are expressed with contours as functions of C and T as for the simplified model..

5.2.1 Influence of different landing positions on the stability

As shown in equation (3.16), the choice of the values of k_S and k_D will affect the landing position of the swing foot. Deduced from equation (3.16), the position errors of the landing foot respect to the fixed values are:

$$\begin{aligned} \delta x_s^- &= (1 - k_S)\delta x_c^-, \\ \delta y_s^- &= (1 - k_D)\delta y_c^-, \end{aligned} \tag{5.1}$$

where δx_c^- and δy_c^- are the position error of the CoM along x and y axes at the end of a step.

It has been shown in Chapters 2 and 3 that the values of k_S and k_D affect the stability of the LIP and VLIP models. How the values of k_S and k_D as well as C and T affect the stability of the essential model is discussed in this section. Eigenvalues are calculated numerically as functions of C and T for four different cases: 1) $k_S = k_D = 0$; 2) $k_S = 1, k_D = 0$; 3) $k_S = 0, k_D = 1$; 4) $k_S = k_D = 1$. For all the cases, the robot Romeo is considered and it is supposed to have a constant height of the CoM $z_0 = 0.65$ m, no impact with the ground and a fixed upper body motion. The position of the ZMP is supposed to be constant and kept at $[0; 0]$. The step length and width are $S = 0.3$ m and $D = 0.15$ m respectively. The case with $k_S = k_D = 0$ is also used as a reference case in

further studies on the influence of other parameters.

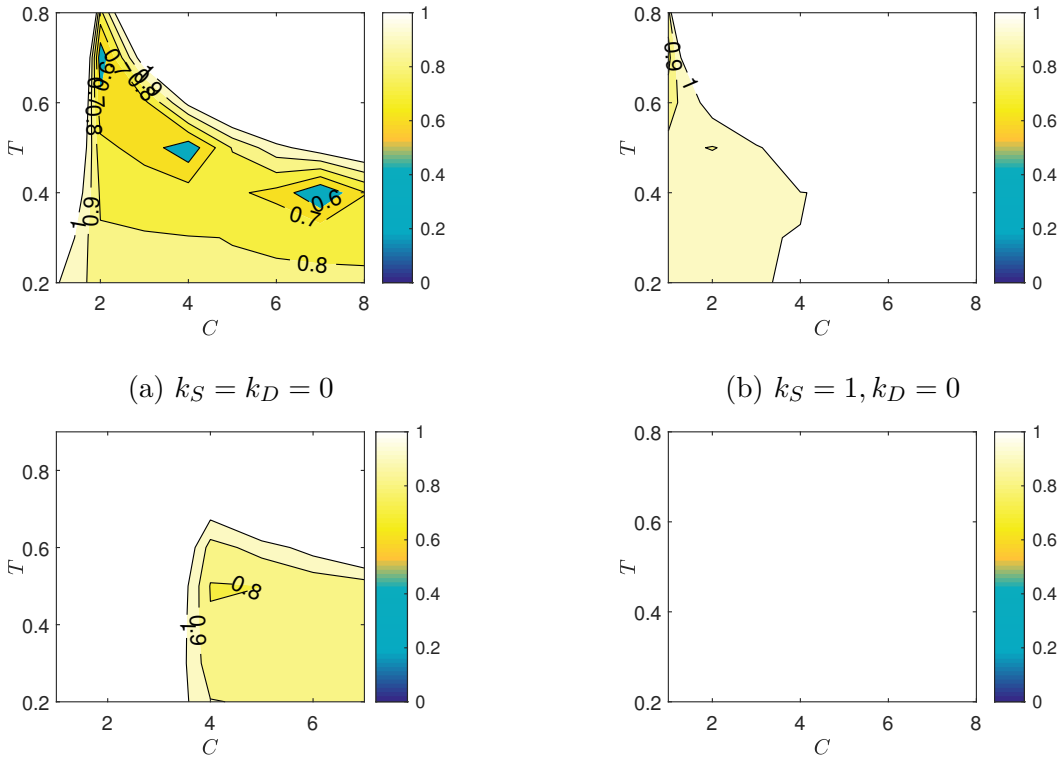

(a) $k_S = k_D = 0$

(b) $k_S = 1, k_D = 0$

(c) $k_S = 0, k_D = 1$

(d) $k_S = k_D = 1$

Figure 5.2 – Influence of k_S and k_D on the eigenvalues for robot Romeo. Contrary to the white areas, the colored areas indicate self-stabilization condition.

It can be seen from Figure 5.2 that when at least one of k_S and k_D equals to zero, there exist some sets of parameters C and T such that all the eigenvalues are smaller than one and thus the walk is stable. Though it is unstable for any C and T when the step length and width are fixed (k_S=k_D=1) with a constant height of the CoM for the essential model, because all the eigenvalues are bigger than one as shown in Figure 5.2d. When $k_S = k_D = 0$, larger stability region can be observed. For the case $k_S = 1, k_D = 0$, stability can be obtained when the value of C is small, while for the case $k_S = 0, k_D = 1$, no stability can be obtained for slow walking velocity with a step timing bigger than 0.7 s.

5.2.2 Comparison of Romeo and TALOS

Romeo and TALOS are two humanoid robots with different heights, weights and inertias. It is interesting to validate the stability of the walking algorithm proposed in this thesis on different robots. The CoM heights of Romeo and TALOS are 0.7008 m and 0.9424 m respectively when their legs are straightened. During walk, the CoM height of Romeo is chosen to be 0.65 m and that of TALOS is 0.8 m to avoid being out of workspace. With bigger size, the step length and width of TALOS are 0.4 m and 0.2 m respectively, while those of Romeo are 0.3 m and 0.15 m. In this comparison, both robots are supposed to have a constant CoM height, no impact between the swing foot and the ground, and a fixed upper body motion. The position of the ZMP is supposed to be constant and kept at the position $[0; 0]$. The positions of the swing feet for the two robots are chosen to nullify the initial CoM position error, i.e. $k_S = k_D = 0$.

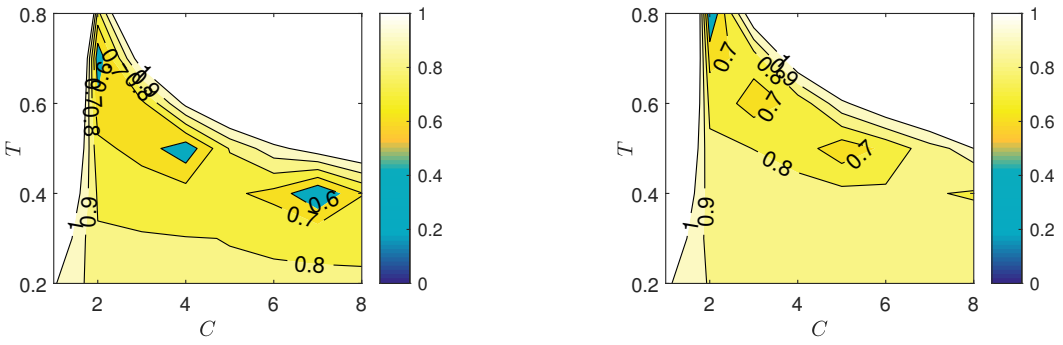

(a) Romeo

(b) TALOS

Figure 5.3 – Comparison of maximum norms of eigenvalues for Romeo and TALOS.

It can be seen from Figure 5.3 that the areas of proper T and C that satisfy the stability condition for TALOS is slightly larger than Romeo. When the step duration increases, the range of proper values of C decreases for both robots. In conclusion, the stability condition obtained for Romeo can be used as a reference for TALOS when they have the same motions of controlled variables and the value for C and T are far from the unstable region.

5.2.3 Influence of the impact

Sometimes, it is important for the swing foot to have a negative vertical velocity before landing, because it will ensure that the swing foot continues to move downward and touches the ground when the ground is uneven. For a complete model, this none-zero vertical velocity will cause impact between the swing foot and the ground. The impact model introduced in Section 4.2.2 is used here. Two cases with and without impact ($v_s = -0.1$ m/s and $v_s = 0$ [1]) are analyzed for Romeo with the same constant CoM height ($z_0 = 0.65$ m) and fixed upper body motion. For both cases, S = 0.3 m, D = 0.15 m, $k_S = k_D = 0$, and the ZMP position is fixed at $[p_x; p_y] = [0; 0]$.

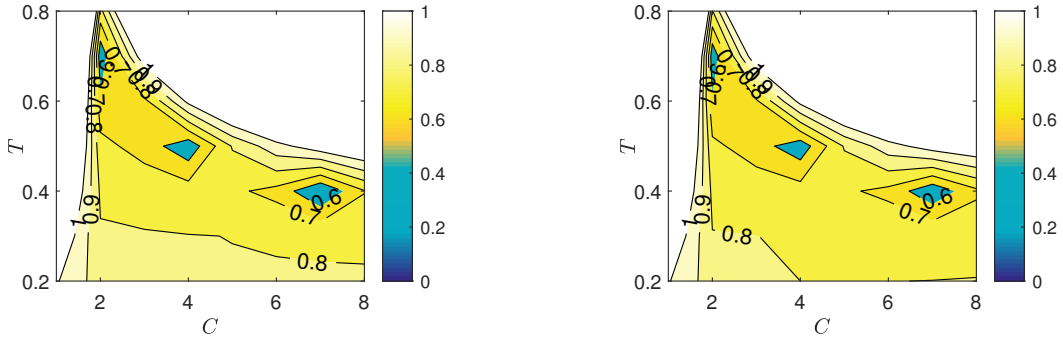

(a) $v_s = 0$ (b) $v_s = -0.1$ m/s

Figure 5.4 – Comparison of maximum norms of eigenvalues for different v_s for robot Romeo.

It can be seen from Figure 5.4 that the impact when $v_s = -0.1$ m/s does not affect the stability of the robot much. Only the change on the contour of eigenvalues equal to 0.8 is observed. That is to say, the stability condition obtained for the case without impact can be used for the case with impact when the vertical velocity of the swing foot at landing is within a certain value. This provides a simpler way to analyze the stability of the walking gait with impact.

1. For $v_s = 0$, the simulation stops when $\Phi = 1$, but when v_s is negative, the simulation stops when the swing foot touches the ground. For a perfect tracking of the controlled variables, when the floor is perfectly flat, this does not introduce differences.

5.2.4 Influence of the vertical CoM motion

As observed in human walking, the CoM of human beings is not constant during a step. It has been proven in Chapter 3 that the vertical CoM velocity $v_m < 0$ at transition is crucial for obtaining stability for an inverted pendulum when no high-level control is performed. How the vertical CoM motion affects the walking stability of the robot Romeo with the essential model is analyzed here. Two cases with the same magnitude $\alpha = 0.03$ m of CoM height but different v_m (-0.1 m/s and -0.2 m/s respectively) are considered to compare with the reference case with a constant CoM height. The CoM height for the reference case is 0.65 m, while the mean CoM height for the comparison cases is 0.65 m as well to avoid being out of workspace. All the reference and comparison cases are supposed to have the same swing foot motion and upper body motion, with S = 0.3 m, D = 0.15 m, $k_S = k_D = 0$, $[p_x; p_y] = [0; 0]$.

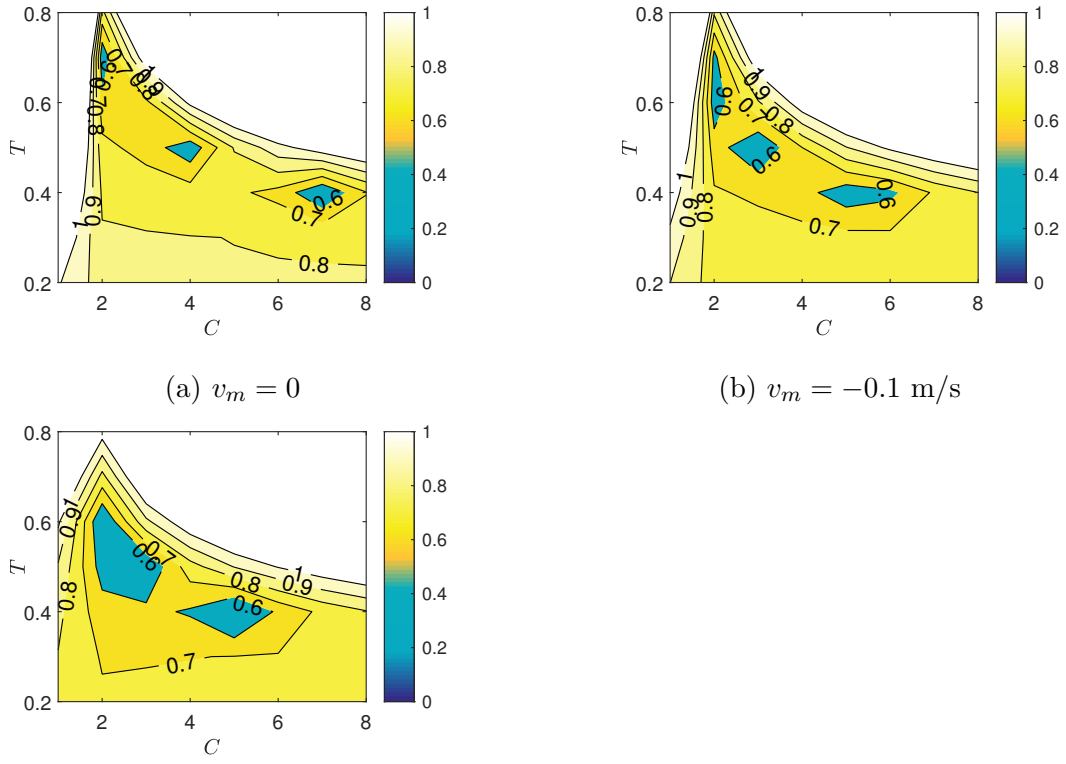

(a) $v_m = 0$

(b) $v_m = -0.1$ m/s

(c) $v_m = -0.2$ m/s

Figure 5.5 – Comparison of maximum norms of eigenvalues for different v_m for robot Romeo.

It can be seen from Figure 5.5 that the norms of the eigenvalues are smaller for walking

gait with larger amplitude of v_m. Stability cannot be obtained for slow walking velocities with step timing larger than 0.8 s when v_m = -0.2 m/s. Different from the VLIP model, the vertical velocity of the CoM being negative is not a necessary condition for the essential model to obtain stability, because the asymmetries in the system during the gaits due to the repartition of masses is enough to generate stability [78]. The vertical velocity of CoM being negative enlarges the area of stability especially for small values of C and reduces the norms of the eigenvalues. However, when v_m is too large, stability cannot be obtained for large step duration such as $T \geq 0.8$ s.

5.2.5 Influence of the upper body motion

As observed in human walking, the human beings swing the arms during a step to reduce the total angular momentum of the body by creating an angular momentum in the direction opposing lower limb rotation. When applying this motion on the robot Romeo, how it affects the stability of the walk is studied here. Two cases with and without upper body motion, i.e. arm and torso swing are compared here. The upper body motions mentioned in Sections 4.5.4 and 4.5.6 are used for these two cases respectively. Both cases are supposed to have no impact and constant CoM height, with S = 0.3 m, D = 0.15 m, $k_S = 0$, $k_D = 0$, $v_s = 0$, $z_m = 0.65$ m and $[p_x; p_y] = [0; 0]$.

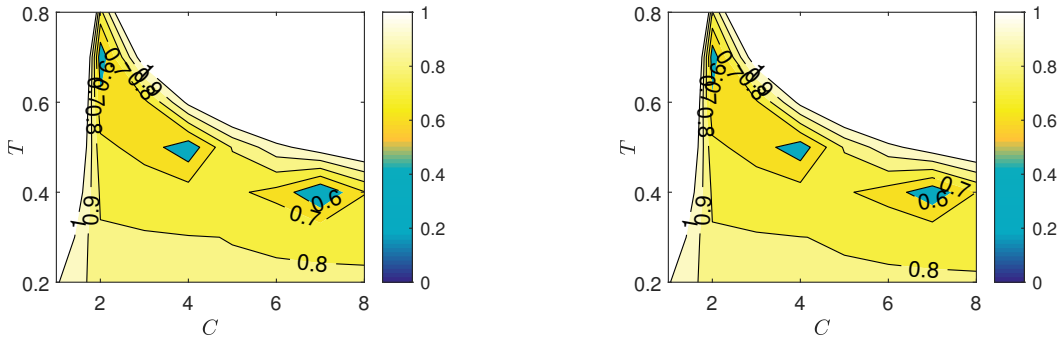

(a) fixed upper body motion

(b) motion with arm swing

Figure 5.6 – Comparison of maximum norms of eigenvalues for different upper body motions for robot Romeo.

It can be seen from Figure 5.6 that the result obtained for the motion with arm and torso swing is almost the same as the result obtained for the fixed upper body motion. Although it is believed that the upper body swing helps reduce the energy cost [116], the

contribution of the upper body swing to the stability is not so obvious with the walking algorithm proposed in this work. On the other hand, this conclusion is interesting since it shows that the stability condition obtained for one fixed upper body motion can be used for the case with a different upper body motion.

5.2.6 Influence of ZMP evolution

One main advantage of the proposed essential model is that a desired location or a path can be imposed for the ZMP during a whole step. This section studies the influence of the ZMP evolution on the stability of walking gaits. Two cases with a constant ZMP and a varying ZMP are compared for robot Romeo. For the case with a constant ZMP, the ZMP is constrained at the zero position, i.e. $[p_{x0}; p_{y0}] = [0; 0]$ and $[p_{xf}; p_{yf}] = [0; 0]$. For the case with a varying ZMP, the 3^{rd} order polynomial functions as in Section 4.5.6 are applied with $[p_{x0}; p_{y0}] = [-0.01; 0.02]$ m and $[p_{xf}; p_{yf}] = [0.08; 0.02]$ m. Both cases are supposed to have no impact, constant CoM height and fixed upper body motion, with S = 0.3 m, D = 0.15 m, $k_S = 0$, $k_D = 0$, $v_s = 0$ and $z_m = 0.65$ m.

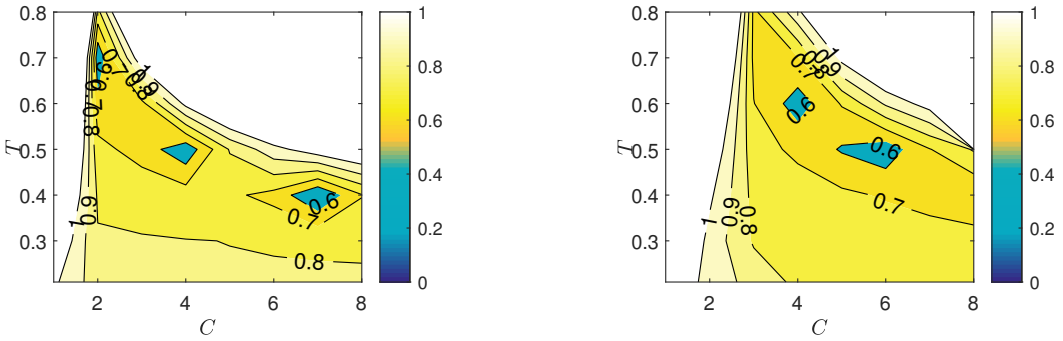

(a) montion with a constant ZMP

(b) motion with a varying ZMP

Figure 5.7 – Comparison of maximum norms of eigenvalues for different ZMP evolutions for robot Romeo.

For the case with a varying ZMP, fast motions with step duration $T < 0.21$ s cannot be calculated with the parameters given above. Thus, motion with step duration $T \geq 0.21$ s are considered in this group. The maximum norms of the obtained eigenvalues are shown in Figure 5.7. It is shown that a varying ZMP enlarges the area of stability in general. However, for slow motions with $T > 0.65$ s, the maximum norm of the eigenvalues of the case with a varying ZMP is larger than that of the case with a constant ZMP.

5.3 Simulations

By considering the stability conditions discussed in the previous section, simulations will be done for the complete models of robots Romeo and TALOS in this section. The starting phase strategy used in the Section 3.5.3 is applied here. Note that the projection of the initial CoM position should be located inside of the support polygon before the first step.

Table 5.2 – Gait parameters for simulations of Romeo and TALOS

Parameter	unit	Romeo	TALOS	Description
k_S	[m]	0	0	Landing position parameter along x axis
k_D	[m]	0	0	Landing position parameter along y axis
T	[s]	0.7	0.5	Step time
z_0	[m]	0.6	0.8	Height of the CoM
h_s	[m]	0.05	0.05	Max. swing foot amplitude
$\varphi_{f,0}$	[deg]	0	0	Free foot initial rotation
$\varphi_{f,f}$	[deg]	0	0	Free foot final rotation
α_z	[m]	0.05	0.05	Max. CoM amplitude
v_m	[m/s]	-0.1	-0.1	Desired vertical CoM velocity at transition
v_s	[m/s]	-0.1	-0.1	Desired landing velocity
$[p_{x0}; p_{y0}]$	[m]	[-0.01;0.02]	[0;0]	Starting point of ZMP
$[p_{xf}; p_{yf}]$	[m]	[0.08;0.02]	[0;0]	Ending point of ZMP

Table 5.3 – Upper-body parameters for TALOS (Unit: rad)

Description	TALOS		
	label	$k_{0,i}$	$k_{f,i}$
Torso yaw	$q^d_{c,10}$	0.1757	- 0.1757
R. shoulder yaw	$q^d_{c,15}$	-0.3	0.2
R. elbow pitch	$q^d_{c,18}$	-0.3491	-0.7854
L. shoulder yaw	$q^d_{c,22}$	-0.2	0.3
L. elbow pitch	$q^d_{c,25}$	-0.7854	-0.3491

5.3.1 Simulations of Romeo

In this section, a humanlike walking pattern is considered for robot Romeo, i.e. with a variable CoM height and swing of arms and torso. The parameters of the CoM and swing foot motions are shown in Table 5.2, while those of the upper body motion is

the same as the Case III in Table 4.4 of Section 4.5.6. Except for the first step, the position of the ZMP is expected to follow a 3^rd order polynomial function varying from $[p_{x0}; p_{y0}] = [-0.01; 0.02]$ m to $[p_{xf}; p_{yf}] = [0.08; 0.02]$ m, and the step timing for the periodic motion is expected to be 0.7 s. A change of step width of the robot from D_1 = 0.15 m to D_2 = 0.2 m is expected at the 15^{th} step. The step length for the periodic value keeps to be S = 0.3 m. Since the proper value of switching manifold parameter C is proportional to the ratio of $\frac{S}{D}$, when C_1 for D_1 = 0.15 m is chosen to be 3, the value of C_2 for D_2 = 0.2 m should be $C_2 = \frac{C_1 D_1}{D_2} = 2.25$. The fixed value for D_1 = 0.15 m is:

$$\begin{aligned} x_{c1}^{*-} &= [\frac{S}{2} + D_{x1},\ \frac{D_1}{2} + D_{y2},\ \dot{x}_{c1}^{*-},\ \dot{y}_{c1}^{*-}]^\top \\ &= [0.192454 \text{ m},\ 0.0766134 \text{ m},\ 0.544429 \text{ m/s},\ 0.176781 \text{ m/s}]^\top. \end{aligned}$$

and that for D_2 = 0.2 m is:

$$\begin{aligned} x_{c2}^{*-} &= [\frac{S}{2} + D_{x2},\ \frac{D_2}{2} + D_{y2},\ \dot{x}_{c2}^{*-},\ \dot{y}_{c2}^{*-}]^\top \\ &= [0.191754 \text{ m},\ 0.101798 \text{ m},\ 0.542622 \text{ m/s},\ 0.257281 \text{ m/s}]^\top. \end{aligned}$$

The maximum eigenvalues for these two cases are:

$$\begin{aligned} \lambda_{D=0.15} &= 0.725880; \\ \lambda_{D=0.2} &= 0.786737. \end{aligned}$$

The step timing for the starting phase is chosen to be 0.7 s in order to obtain an initial CoM position that makes the ZMP located inside of the support polygon. Since the initial CoM position for the starting phase is calculated based on the 3D LIP model, the ZMP evolution for the starting phase is chosen to be fixed at $[0; 0]$ to be more close to the 3D LIP model.

The schematic illustration of the first 5 steps including the starting phase for Romeo is shown in Figure 5.8. Figure 5.9 presents the projections of the CoM motion of Romeo in horizontal, sagittal and frontal planes, and the position of the stance ankle for each step. Note that the local reference frame is attached to the projection of the stance ankle on the ground, the circles in Figure 5.9(a) represent also the positions of the local frame in the world frame. From Figure 5.9 it can be seen that the trajectory of the CoM starts from a position close to the stance foot at the starting phase, and converges to the periodic motion for D_1 = 0.15 m after several steps. At the 15^{th} step, it can been seen clearly

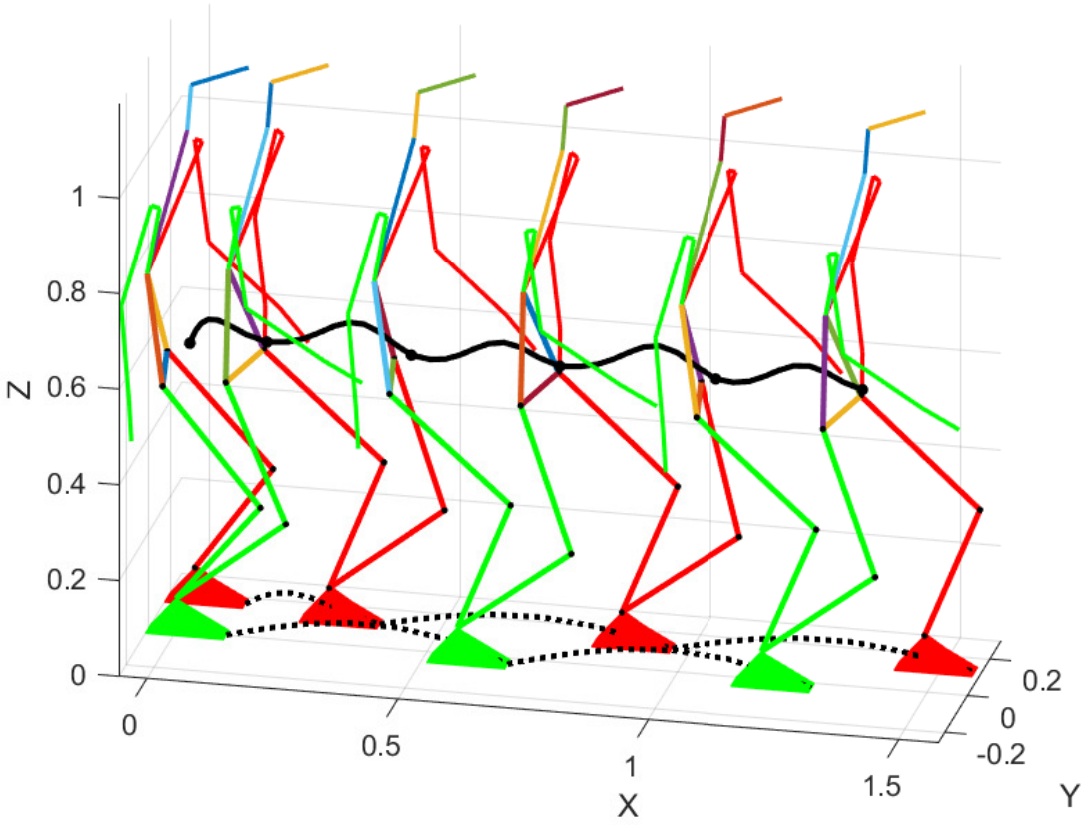

Figure 5.8 – Illustration of 5 steps for Romeo.

that the step width is increased. The change of the step width at the 15^{th} step causes an initial CoM position error at the 16^{th} step and this is regarded as a disturbance, and then the CoM converges to the periodic motion for $D_2 = 0.2$ m. The blue lines in Figure 5.9(a) represent the switching manifold given by equation (3.13). The cyclic motion in the frontal place shown in Figure 5.9(c) is displaced along y axis due to the change of D and $k_D = 0$. The evolutions of the ZMP for the first 5 steps are shown in Figure 5.10. It can be seen that except for the first step that the ZMP stays at the zero position, the ZMP of the other steps moves from the rear to the front of the sole, following a straight segment given by the desired values. Figures 5.11 and 5.12 present the evolutions of the step timing and the state of the robot. Since the step timing is not imposed by the control law, its value varies after the starting phase and during the change of step width, and eventually converges to the expected value. The variation of step timing contributes to

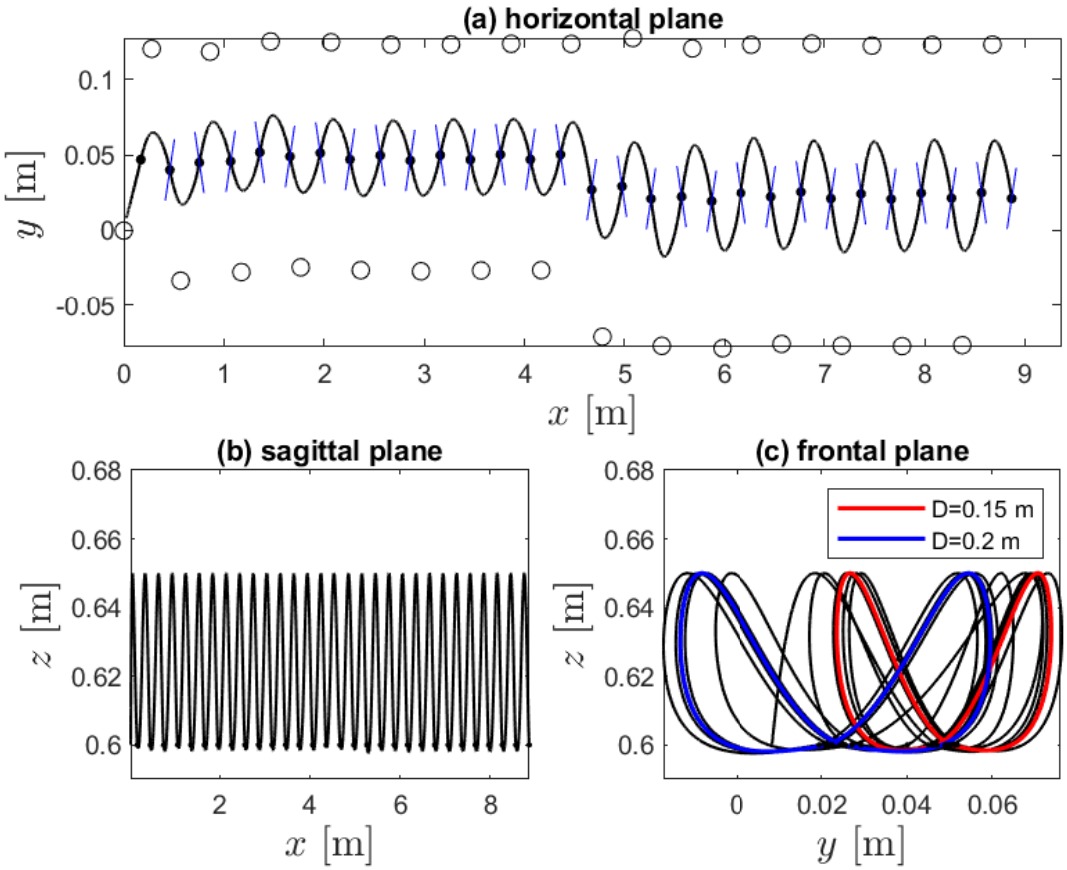

Figure 5.9 – Projections of the CoM trajetory in horizontal, sagittal and frontal planes. The blue lines represent the switching manifold for each step, and the circles represent the positions of the ZMP.

resist the perturbation. The fixed values of the first 15 steps in Figure 5.12 is given by x_1^{*-}, while that of the last 15 steps is given by x_2^{*-}. It can be seen that the change of step width D has a larger influence on the state along y axis than that along x axis. The state of the robot converges to the periodic motion with $D = 0.15$ m after the starting phase, experiences a change of D, and eventually converges to the periodic motion with $D = 0.2$ m. The tracking of controlled variables and the ZMP is imposed, and the free variables i.e. the horizontal position of the CoM converges to the periodic motion. Thus, self-stabilization is obtained.

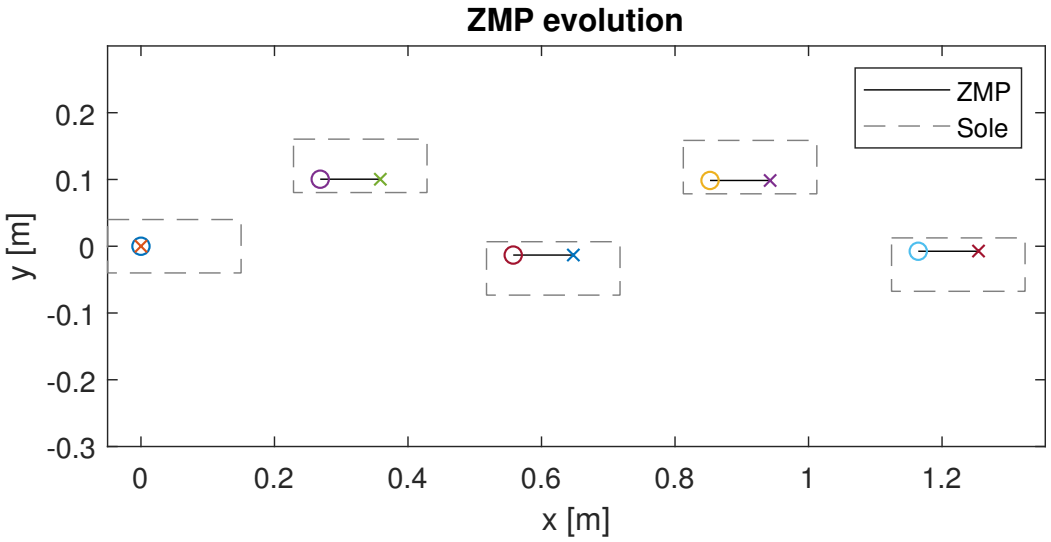

Figure 5.10 – The ZMP evolution of Romeo. The circles and the crosses represent the starting and ending points of the stance ankle at each step.

5.3.2 Simulations of TALOS

In this section, another humanoid robot TALOS is analyzed. A humanlike walking pattern that has vertical CoM motion and swing of torso and arms with parameters shown in Tables 5.2 and 5.3 is considered. The position of the ZMP is expected to be fixed at the point $[p_x^d; p_y^d] = [0; 0]$. For TALOS, a change of step length from $S_1 = 0.4$ m to $S_2 = 0.5$ m is expected at the 10^{th} step, while the step width is $D = 0.2$ m. The switching manifold parameter C_1 for $S_1 = 0.4$ m is chosen to be 5 and C_2 for $S_2 = 0.5$ m is $C_2 = \frac{C_1 S_2}{S_1} = 6.25$. The expected step timing for the periodic motion is 0.5 s. The fixed value for $S_1 = 0.4$ m is:

$$\begin{aligned} x_{c1}^{*-} &= [\frac{S}{2} + D_{x1},\ \frac{D_1}{2} + D_{y2},\ \dot{x}_{c1}^{*-},\ \dot{y}_{c1}^{*-}]^\top \\ &= [0.223876 \text{ m},\ 0.100068 \text{ m},\ 0.932822 \text{ m/s},\ 0.226575 \text{ m/}s]^\top. \end{aligned}$$

and that for $S_2 = 0.5$ m is:

$$\begin{aligned} x_{c2}^{*-} &= [\frac{S}{2} + D_{x2},\ \frac{D_2}{2} + D_{y2},\ \dot{x}_{c2}^{*-},\ \dot{y}_{c2}^{*-}]^\top \\ &= [0.278119 \text{ m},\ 0.100222 \text{ m},\ 1.168078 \text{ m/s},\ 0.225770 \text{ m/s}]^\top. \end{aligned}$$

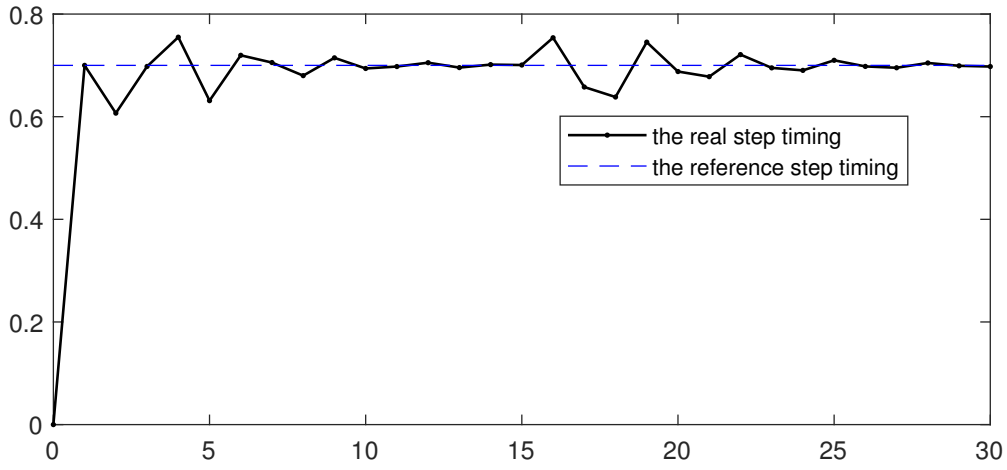

Figure 5.11 – State evolution of step timing for Romeo.

The maximum eigenvalues for these two cases are:

$$\lambda_{S=0.4} = 0.482944;$$
$$\lambda_{S=0.45} = 0.484544$$

The schematic illustration of the first 5 steps including the starting phase for TALOS is shown in Figure 5.13. Figure 5.14 presents the projection of the CoM motion of TALOS in horizontal, sagittal and frontal planes, and the position of the ZMP for each step. Since the ZMP is constrained to be located at the projection of the stance leg ankle on the ground due to the condition $(p_x^d, p_y^d) = (0, 0)$, the circles in Figure 5.14 indicate also the stance foot locations. It can be seen from Figure 5.14 that the CoM converges to the periodic motion before and after the change of step length. The distance between the positions of two stance foot is obviously larger after the 10_{th} step due to the change of step length. Figures 5.15 and 5.16 present the evolution of step timing and the state of the robot. The state of the robot converges to the periodic motion during the first 10 step, and perturbed due to the change of step length. The increase of sagittal position and velocity is obvious because the step length is increased. Meanwhile, only a slight change of lateral position and velocity can be observed. Both the step timing and the state of the robot converge to the new expected periodic motion after the change of step length, thus self-stabilization is obtained.

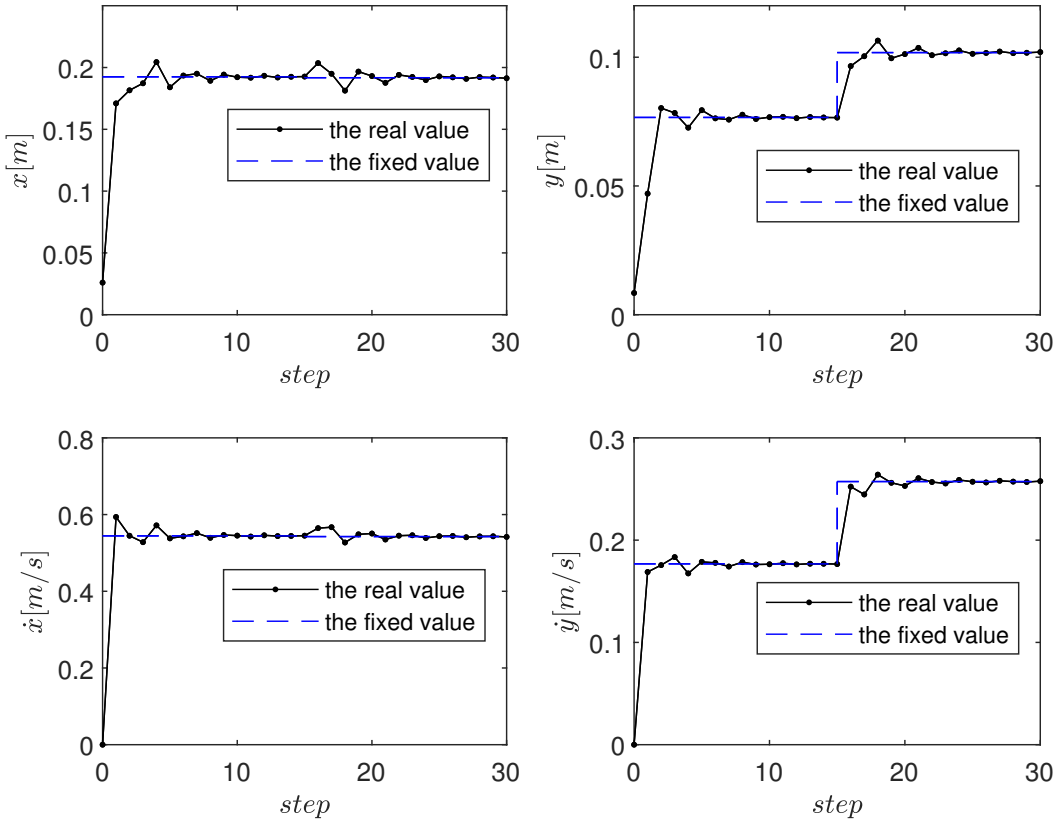

Figure 5.12 – State evolution of Romeo.

5.4 Conclusion

This chapter analyzed the stability of many different walking patterns on robots Romeo and TALOS. It has been proven that when the controlled variables are defined as functions of time, no stability can be obtained for any value of k_S, k_D, v_m or v_s without a high-level controller. Then the stability of cases when the phasing variable is based on the internal state of the robot (i.e. x and y) is analyzed. These cases are divided into six comparison groups, each of them compares a different character of walking patterns: the landing positions of the swing foot; size, mass and inertia; the swing foot motion; the vertical CoM motion, the upper body motion and the ZMP evolution. It has been shown that the impact and upper body motion barely affect the stability of the system because they have almost the same eigenvalue contours. The values of k_S and k_D affect the stability

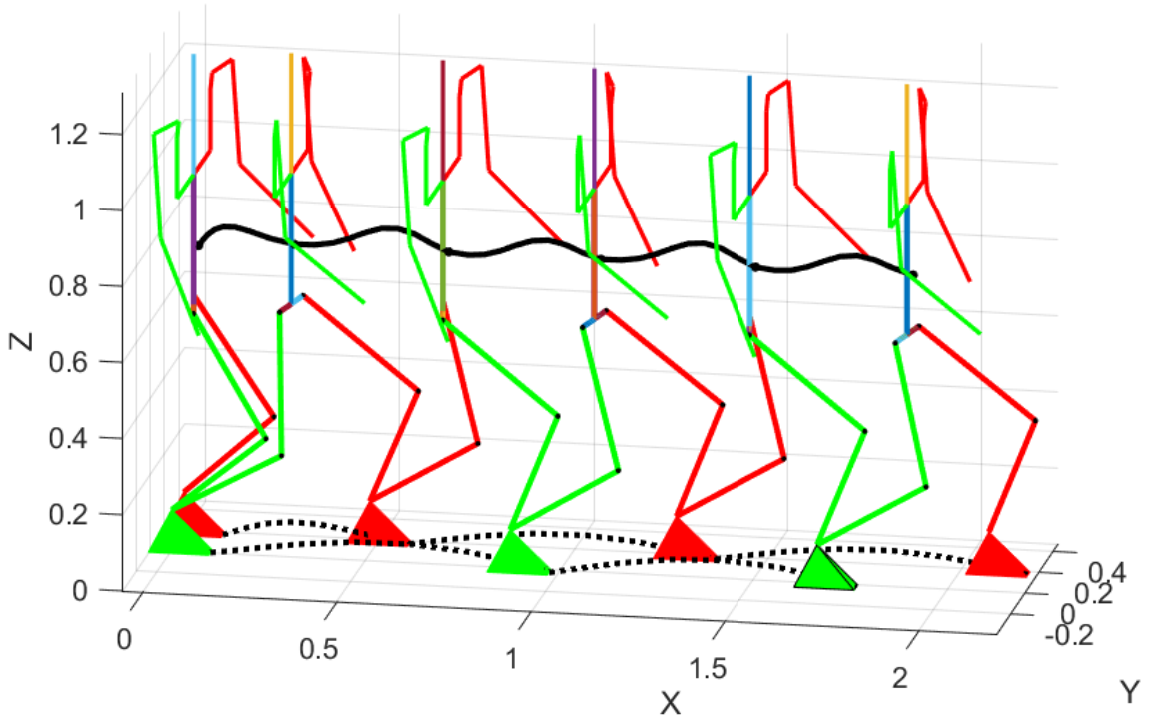

Figure 5.13 – Illustration of 5 steps for TALOS.

most, thus stability analysis must be done separately for different choices of k_S and k_D. With the same motion of controlled variables, the stability condition of robot Romeo can serve as a reference for the robot TALOS. As for the vertical CoM motion, it has been proven that with bigger magnitude of v_m, the obtained eigenvalue is smaller. It can be also observed that a varying ZMP enlarges the stability area. The results of the simulations have shown that the walk converges to the periodic value from a perturbed value. Thus, by extending the walking algorithm proposed for the simplified model in this thesis to the complete model, self-stabilization can also be obtained.

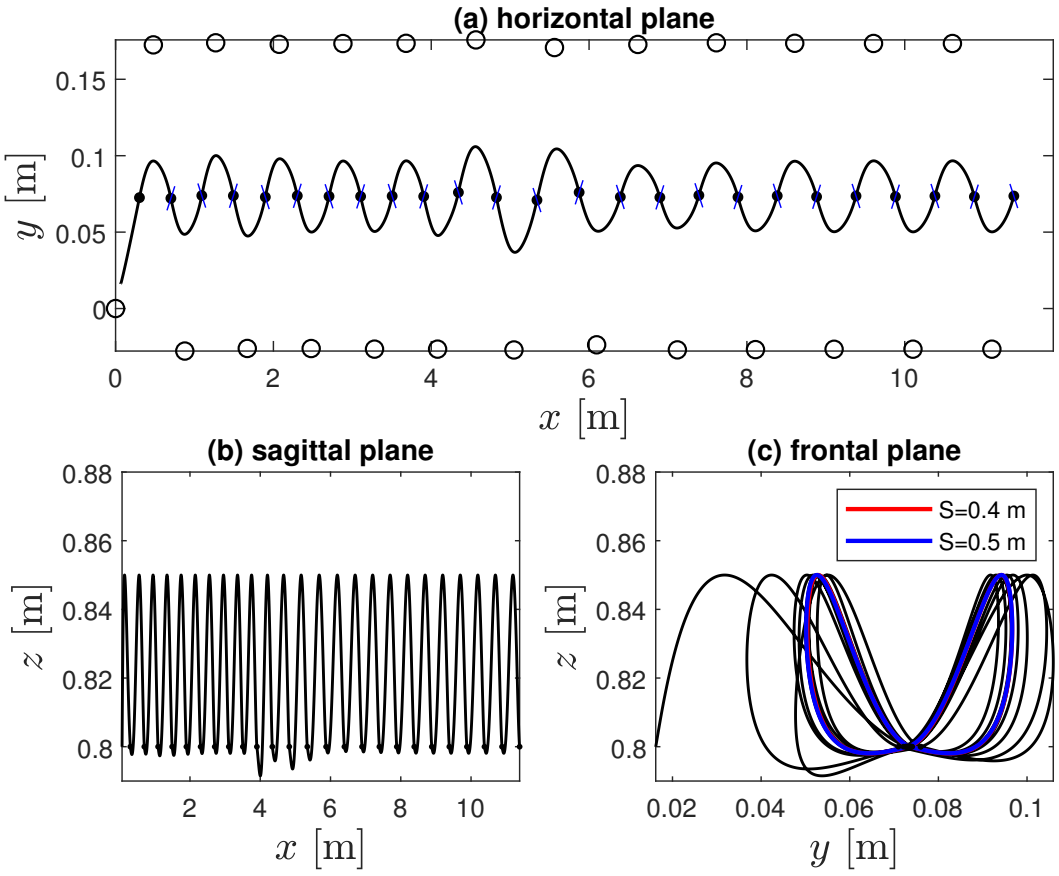

Figure 5.14 – Projections of the CoM trajetory in horizontal, sagittal and frontal planes. The blue lines represent the switching manifold for each step, and the circles represent the positions of the ZMP.

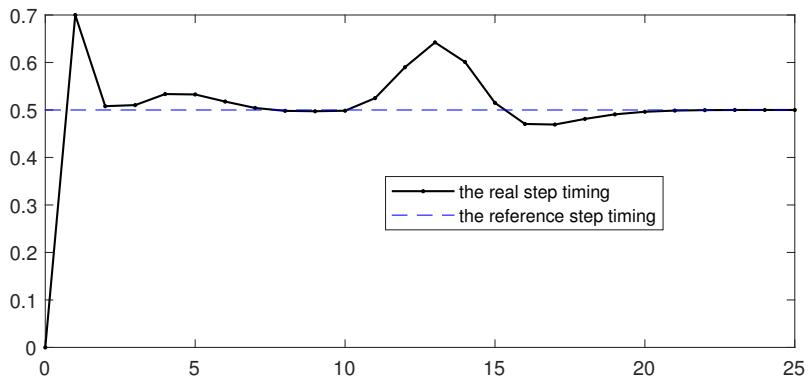

Figure 5.15 – State evolution of step timing.

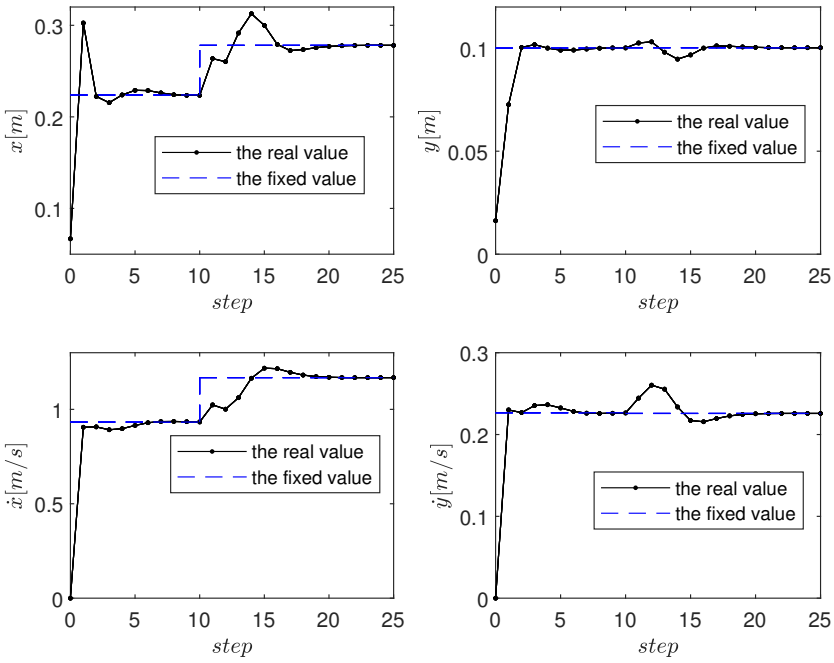

Figure 5.16 – State evolution of TALOS.

Chapter 6

Conclusions and perspectives

6.1 Conclusions

When walking on a relatively even ground, human beings do not have to pay attention to the steps. The main contribution of this thesis is having proposed a novel walking algorithm which imitates the intrinsic nature of human walking to avoid using online optimization or predictive control methods. This walking algorithm has been applied to the simplified models (LIP model and VLIP model) and the complete model of the robot. With this method, the controlled variables are defined as functions of a phasing variable based on the internal state of the robot instead of time. Moreover, a switching manifold has been proposed. With proper choice of the characteristics of the switching manifold and landing position of the swing foot, self-synchronization or self-stability can be obtained for the waling gait. Self-synchronization implies that the velocity is not controlled but that the robot motion converges toward a periodic motion and evolves along a straight path, while self-stabilization implies that the walking velocity can be chosen. A perfect tracking of the controlled variables is assumed in this thesis.

For the LIP Model, a phasing variable that is a quadratic function of the horizontal positions of the CoM along x and y axes has been proposed, and its monotonicity has been analyzed. It has been shown that self-synchronization can be obtained when controlled variables are defined with the proposed phasing variable and the swing foot lands at a position where the initial CoM position error of next step is reduced. Then it has been proven that the introduction of the CoM velocity feedback into the phasing variable permits to achieve self-stabilization of the walking gait for a LIP model.

For a VLIP Model, when the vertical CoM velocity of the robot is negative, it is possible to obtain self-stability by defining the controlled variables as functions of the phasing variable based on the horizontal position of the CoM. Furthermore, when the walking velocity is considered in the phasing variable, the robot can converge to another periodic motion with a different walking speed. This provides a novel approach to find a

periodic motion of bipedal robots without using any kind of offline or online search for fixed points.

For a humanoid robot, the essential model has been proposed, which is a novel dynamic model that has the same dimension as the 3D LIP model but considers the complete dynamics of the robot. This essential model is especially useful for fully actuated humanoid robots with feet, because it is able to generate walking gaits that ensure the ZMP to be kept in an expected position or trajectory. Simulations have been done with the robot Romeo to compare the essential model and the LIP model. It has shown that it is important to take into account the complete dynamics for a robot with none-point feet to make sure that the ZMP stays inside of the support polygon. Then different walking gaits and ZMP evolutions have been demonstrated on robots Romeo and TALOS with the essential model.

Then results obtained for the simplified models have been extended to the study of humanoid robots considering the complete dynamics. The influence of different walking patterns on the stability of the proposed walking algorithm applied on the essential model have been analyzed. It has been shown that the impact and upper body motion barely affect the stability of the walking gait while the landing position of the swing foot affects the stability most. The vertical CoM motion and ZMP evolution affect the stability a little but not too much. With the same motion of controlled variables, the stability condition of robot Romeo can serve as a reference for the robot TALOS.

6.2 Perspectives

In the thesis, numerical simulations have been done to validate the proposed walking algorithm and the essential model. Some future works on this issue are:

— Experiments on the robot TALOS; tests in Gazebo, which consider the real physical environment need to be conducted first, and then results can be applied on the real robot TALOS. The difficulties are the modeling uncertainty and the tracking errors;

— Introducing optimization to the controlled variables i.e. the upper body, the vertical CoM and swing foot motions in order to reduce the joint torques, energy consumption etc.; in this thesis, polynomial functions or spline functions are used to define the trajectories of the controlled variables. More choices are possible such as the Bézier curves [117, 118] or the cycloidal curves [87, 119];

— Proposing human-like trajectories for the ZMP; It has been shown in [120] that

in human walking, the ZMP goes from the heel to the tip of each foot, which corresponds to the rolling motion of the feet and the mobility of the human sole. In the future, more human-like ZMP trajectories can be studied to imitate the human walking and the contribution of the ZMP trajectories to the efficiency of walking gait can be studied;

— Introducing different external information to define the desired trajectories of the controlled variables, not just the time. This external information could be the CoM position or velocity of other robots in order to achieve walking synchronization among robots by using the k_v term mentioned in Section 3.6;

— How the motion of the head affects the stability of the walking gaits can also be studied; since it has been shown in [121] that the head stabilization enables a humanoid robot to generate intrinsically more stable gait kinematics than a rigid neck, the influence of the head stabilization on the walking stability can also be interesting;

— Exploiting the possibility to control the direction of the walking by changing the orientation of the foot. The swing ankle rotation control proposed in [74] can be integrated in the walking algorithms proposed in this thesis, thus the direction of the walking can be controlled.

BIBLIOGRAPHY

[1] Shuuji Kajita, Fumio Kanehiro, Kenji Kaneko, Kazuhito Yokoi, and Hirohisa Hirukawa. The 3d linear inverted pendulum mode: A simple modeling for a biped walking pattern generation. In *Intelligent Robots and Systems, 2001. Proceedings. 2001 IEEE/RSJ International Conference on*, volume 1, pages 239–246. IEEE, 2001.

[2] S. Kajita, F. Kanehiro, K. Kaneko, K. Fujiwara, K. Harada, K. Yokoi, and H. Hirukawa. Biped walking pattern generation by using preview control of zero-moment point. In *2003 IEEE Int. Conf. on Robotics and Automation (Cat. No.03CH37422)*, volume 2, pages 1620–1626, September 2003.

[3] Johannes Englsberger, Christian Ott, Máximo A Roa, Alin Albu-Schäffer, and Gerhard Hirzinger. Bipedal walking control based on capture point dynamics. In *Intelligent Robots and Systems (IROS), 2011 IEEE/RSJ International Conference on*, pages 4420–4427. IEEE, 2011.

[4] S. Kuindersma, F. Permenter, and R. Tedrake. An efficiently solvable quadratic program for stabilizing dynamic locomotion. In *2014 IEEE International Conference on Robotics and Automation (ICRA)*, pages 2589–2594, May 2014.

[5] Jean-Paul Laumond, Mehdi Benallegue, Justin Carpentier, and Alain Berthoz. The yoyo-man. *The International Journal of Robotics Research*, 36(13-14):1508–1520, 2017.

[6] Eric R Westervelt, Christine Chevallereau, Jun Ho Choi, Benjamin Morris, and Jessy W Grizzle. *Feedback control of dynamic bipedal robot locomotion*. CRC press, 2007.

[7] Hamed Razavi, Anthony M Bloch, Christine Chevallereau, and Jessy W Grizzle. Restricted discrete invariance and self-synchronization for stable walking of bipedal robots. In *American Control Conference (ACC), 2015*, pages 4818–4824. IEEE, 2015.

[8] C. Chevallereau, G. Abba, Y. Aoustin, E. R. Westervelt F. Plestan, C. Canudas, and J.W. Grizzle. Rabbit: a testbed for advanced control theory. *IEEE Control Systems Magazine*, 23(5):57–79, October 2003.

[9] Eric R Westervelt, Jessy W Grizzle, and Daniel E Koditschek. Hybrid zero dynamics of planar biped walkers. *IEEE transactions on automatic control*, 48(1):42–56, 2003.

[10] Christine Chevallereau and Yannick Aoustin. Self-stabilization of 3d walking via vertical oscillations of the hip. In *Robotics and Automation (ICRA), 2015 IEEE International Conference on*, pages 5088–5093. IEEE, 2015.

[11] Kazuo Hirai, Masato Hirose, Yuji Haikawa, and Toru Takenaka. The development of honda humanoid robot. In *Proceedings. 1998 IEEE International Conference on Robotics and Automation (Cat. No. 98CH36146)*, volume 2, pages 1321–1326. IEEE, 1998.

[12] Guang-Zhong Yang, Bradley J. Nelson, Robin R. Murphy, Howie Choset, Henrik Christensen, Steven H. Collins, Paolo Dario, Ken Goldberg, Koji Ikuta, Neil Jacobstein, Danica Kragic, Russell H. Taylor, and Marcia McNutt. Combating covid-19—the role of robotics in managing public health and infectious diseases. *Science Robotics*, 5(40), 2020.

[13] Ichiro Kato. Development of wabot 1. *Biomechanism*, 2:173–214, 1973.

[14] Tad McGeer et al. Passive dynamic walking. *I. J. Robotic Res.*, 9(2):62–82, 1990.

[15] Steven H Collins, Martijn Wisse, and Andy Ruina. A three-dimensional passive-dynamic walking robot with two legs and knees. *The International Journal of Robotics Research*, 20(7):607–615, 2001.

[16] Christine Chevallereau, Gabriel Abba, Yannick Aoustin, Franck Plestan, Eric Westervelt, Carlos Canudas De Wit, and Jessy Grizzle. Rabbit: A testbed for advanced control theory. 2003.

[17] Eric R Westervelt, Gabriel Buche, and Jessy W Grizzle. Experimental validation of a framework for the design of controllers that induce stable walking in planar bipeds. *The International Journal of Robotics Research*, 23(6):559–582, 2004.

[18] Jessy W Grizzle, Jonathan Hurst, Benjamin Morris, Hae-Won Park, and Koushil Sreenath. Mabel, a new robotic bipedal walker and runner. In *2009 American Control Conference*, pages 2030–2036. IEEE, 2009.

[19] Jesse A Grimes and Jonathan W Hurst. The design of atrias 1.0 a unique monopod, hopping robot. In *Adaptive Mobile Robotics*, pages 548–554. World Scientific, 2012.

[20] Brian G Buss, Alireza Ramezani, Kaveh Akbari Hamed, Brent A Griffin, Kevin S Galloway, and Jessy W Grizzle. Preliminary walking experiments with underac-

tuated 3d bipedal robot marlo. In *2014 IEEE/RSJ International Conference on Intelligent Robots and Systems*, pages 2529–2536. IEEE, 2014.

[21] Taylor Apgar, Patrick Clary, Kevin Green, Alan Fern, and Jonathan W Hurst. Fast online trajectory optimization for the bipedal robot cassie. In *Robotics: Science and Systems*, 2018.

[22] Agility Robotics. Meet digit — agility robotics. `https://www.agilityrobotics.com/robots#digit`. Accessed May 10, 2020.

[23] Yoshiaki Sakagami, Ryujin Watanabe, Chiaki Aoyama, Shinichi Matsunaga, Nobuo Higaki, and Kikuo Fujimura. The intelligent asimo: System overview and integration. In *IEEE/RSJ international conference on intelligent robots and systems*, volume 3, pages 2478–2483. IEEE, 2002.

[24] Kazuhito Yokoi, Naoto Kawauchi, Naoyuki Sawasaki, Toshiya Nakajima, Shinya Nakamura, Kazuya Sawada, Ikuo Takeuchi, Katsumi Nakashima, Yoshitaka Yanagihara, Kazuhiko Yokoyama, et al. Humanoid robot applications in hrp. *International Journal of Humanoid Robotics*, 1(03):409–428, 2004.

[25] Fumio Kanehiro, Hirohisa Hirukawa, and Shuuji Kajita. Openhrp: Open architecture humanoid robotics platform. *The International Journal of Robotics Research*, 23(2):155–165, 2004.

[26] Kenji Kaneko, Kensuke Harada, Fumio Kanehiro, Go Miyamori, and Kazuhiko Akachi. Humanoid robot hrp-3. In *2008 IEEE/RSJ International Conference on Intelligent Robots and Systems*, pages 2471–2478. IEEE, 2008.

[27] Kenji Kaneko, Fumio Kanehiro, Mitsuharu Morisawa, Kazuhiko Akachi, Go Miyamori, Atsushi Hayashi, and Noriyuki Kanehira. Humanoid robot hrp-4-humanoid robotics platform with lightweight and slim body. In *2011 IEEE/RSJ International Conference on Intelligent Robots and Systems*, pages 4400–4407. IEEE, 2011.

[28] Shuuji Kajita, Kenji Kaneko, Fumio Kaneiro, Kensuke Harada, Mitsuharu Morisawa, Shin'ichiro Nakaoka, Kanako Miura, Kiyoshi Fujiwara, Ee Sian Neo, Isao Hara, et al. Cybernetic human hrp-4c: A humanoid robot with human-like proportions. In *Robotics Research*, pages 301–314. Springer, 2011.

[29] Kenji Kaneko, Hiroshi Kaminaga, Takeshi Sakaguchi, Shuuji Kajita, Mitsuharu Morisawa, Iori Kumagai, and Fumio Kanehiro. Humanoid robot hrp-5p: An elec-

trically actuated humanoid robot with high-power and wide-range joints. *IEEE Robotics and Automation Letters*, 4(2):1431–1438, 2019.

[30] Kai Henning Koch, Katja Mombaur, Olivier Stasse, and Philippe Soueres. Optimization based exploitation of the ankle elasticity of hrp-2 for overstepping large obstacles. In *2014 IEEE-RAS International Conference on Humanoid Robots*, pages 733–740. IEEE, 2014.

[31] Jonas Koenemann, Andrea Del Prete, Yuval Tassa, Emanuel Todorov, Olivier Stasse, Maren Bennewitz, and Nicolas Mansard. Whole-body model-predictive control applied to the hrp-2 humanoid. In *2015 IEEE/RSJ International Conference on Intelligent Robots and Systems (IROS)*, pages 3346–3351. IEEE, 2015.

[32] Justin Carpentier, Steve Tonneau, Maximilien Naveau, Olivier Stasse, and Nicolas Mansard. A versatile and efficient pattern generator for generalized legged locomotion. In *2016 IEEE International Conference on Robotics and Automation (ICRA)*, pages 3555–3561. IEEE, 2016.

[33] SCHAFT Inc. Who is schaft, the robot company bought by google and winner of the drc? https://spectrum.ieee.org/automaton/robotics/humanoids/schaft-robot-company-bought-by-google-darpa-robotics-challenge-winner. Accessed Feb 06, 2014.

[34] Yuki Asano, Toyotaka Kozuki, Soichi Ookubo, Masaya Kawamura, Shinsuke Nakashima, Takeshi Katayama, Iori Yanokura, Toshinori Hirose, Kento Kawaharazuka, Shogo Makino, et al. Human mimetic musculoskeletal humanoid kengoro toward real world physically interactive actions. In *2016 IEEE-RAS 16th International Conference on Humanoid Robots (Humanoids)*, pages 876–883. IEEE, 2016.

[35] Boston Dynamics. What's new, atlas? `https://www.youtube.com/watch?v=fRj34o4hN4I`. Accessed November 16, 2017.

[36] Boston Dynamics. More parkour atlas. `https://www.youtube.com/watch?v=_sBBaNYex3E`. Accessed September 19, 2019.

[37] Olivier Stasse, Thomas Flayols, Rohan Budhiraja, Kevin Giraud-Esclasse, Justin Carpentier, Joseph Mirabel, Andrea Del Prete, Philippe Souères, Nicolas Mansard, Florent Lamiraux, et al. Talos: A new humanoid research platform targeted for industrial applications. In *2017 IEEE-RAS 17th International Conference on Humanoid Robotics (Humanoids)*, pages 689–695. IEEE, 2017.

[38] Giorgio Metta, Giulio Sandini, David Vernon, Lorenzo Natale, and Francesco Nori. The icub humanoid robot: an open platform for research in embodied cognition.

In *Proceedings of the 8th workshop on performance metrics for intelligent systems*, pages 50–56, 2008.

[39] UBTECH Robotics. Your end-to-end robotics partner. `https://www.ubtrobot.com/collections/innovation-at-ubtech?ls=en`. Accessed March 31, 2020.

[40] Shuuji Kajita, Hirohisa Hirukawa, Kensuke Harada, and Kazuhito Yokoi. *Introduction to humanoid robotics*, volume 101. Springer, 2014.

[41] S. Kajita and K. Tani. Study of dynamic biped locomotion on rugged terrain-derivation and application of the linear inverted pendulum mode. In *Proceedings. 1991 IEEE International Conference on Robotics and Automation*, pages 1405–1411 vol.2, 1991.

[42] Miomir Vukobratović and Branislav Borovac. Zero-moment point—thirty five years of its life. *International journal of humanoid robotics*, 1(01):157–173, 2004.

[43] Philippe Sardain and Guy Bessonnet. Forces acting on a biped robot. center of pressure-zero moment point. *IEEE Transactions on Systems, Man, and Cybernetics-Part A: Systems and Humans*, 34(5):630–637, 2004.

[44] Pierre-Brice Wieber. Trajectory free linear model predictive control for stable walking in the presence of strong perturbations. In *2006 6th IEEE-RAS International Conference on Humanoid Robots*, pages 137–142. IEEE, 2006.

[45] Koichi Nishiwaki and Satoshi Kagami. High frequency walking pattern generation based on preview control of zmp. In *Proceedings 2006 IEEE International Conference on Robotics and Automation, 2006. ICRA 2006.*, pages 2667–2672. IEEE, 2006.

[46] Jerry Pratt, John Carff, Sergey Drakunov, and Ambarish Goswami. Capture point: A step toward humanoid push recovery. In *2006 6th IEEE-RAS international conference on humanoid robots*, pages 200–207. IEEE, 2006.

[47] Johannes Englsberger, Christian Ott, and Alin Albu-Schäffer. Three-dimensional bipedal walking control based on divergent component of motion. *IEEE Transactions on Robotics*, 31(2):355–368, 2015.

[48] S. Kajita, M. Benallegue, R. Cisneros, T. Sakaguchi, S. Nakaoka, M. Morisawa, K. Kaneko, and F. Kanehiro. Biped walking pattern generation based on spatially quantized dynamics. In *IEEE-RAS 17th International Conference on Humanoid Robotics (Humanoids)*, pages 599–605, Nov 2017.

[49] Liandong Zhang and Changjiu Zhou. Optimal three-dimensional biped walking pattern generation based on geodesics. *International Journal of Advanced Robotic Systems*, 14(2):1–11, 2017.

[50] T. Erez and W. D. Smart. Bipedal walking on rough terrain using manifold control. In *2007 IEEE/RSJ International Conference on Intelligent Robots and Systems*, pages 1539–1544, 2007.

[51] Ambarish Goswami, Bernard Espiau, and Ahmed Keramane. Limit cycles in a passive compass gait biped and passivity-mimicking control laws. *Autonomous Robots*, 4(3):273–286, 1997.

[52] F. Asano, M. Yamakita, and K. Furuta. Virtual passive dynamic walking and energy-based control laws. In *Proceedings. 2000 IEEE/RSJ International Conference on Intelligent Robots and Systems (IROS 2000) (Cat. No.00CH37113)*, volume 2, pages 1149–1154 vol.2, 2000.

[53] F. Asano and M. Yamakita. Virtual gravity and coupling control for robotic gait synthesis. *IEEE Transactions on Systems, Man, and Cybernetics - Part A: Systems and Humans*, 31(6):737–745, 2001.

[54] F. Asano, M. Yamakita, N. Kamamichi, and Zhi-Wei Luo. A novel gait generation for biped walking robots based on mechanical energy constraint. *IEEE Transactions on Robotics and Automation*, 20(3):565–573, 2004.

[55] F. Asano, Zhi-Wei Luo, and M. Yamakita. Biped gait generation and control based on a unified property of passive dynamic walking. *IEEE Transactions on Robotics*, 21(4):754–762, 2005.

[56] M. W. Spong and F. Bullo. Controlled symmetries and passive walking. *IEEE Transactions on Automatic Control*, 50(7):1025–1031, 2005.

[57] JA Scott Kelso, Kenneth G Holt, Philip Rubin, and Peter N Kugler. Patterns of human interlimb coordination emerge from the properties of non-linear, limit cycle oscillatory processes: Theory and data. *Journal of motor behavior*, 13(4):226–261, 1981.

[58] Hassan K Khalil and Jessy W Grizzle. *Nonlinear systems*, volume 3. Prentice hall Upper Saddle River, NJ, 2002.

[59] Carlos Canudas-de Wit. On the concept of virtual constraints as a tool for walking robot control and balancing. *Annual Reviews in Control*, 28(2):157–166, 2004.

[60] Yannick Aoustin and Alexander Formal'sky. Design of reference trajectory to stabilize desired nominal cyclic gait of a biped. In *Proceedings of the First Workshop on Robot Motion and Control. RoMoCo'99 (Cat. No. 99EX353)*, pages 159–164. IEEE, 1999.

[61] Y Aoustin and AM Formal'sky. Control design for a biped: Reference trajectory based on driven angles as functions of the undriven angle. *Journal of Computer and Systems Sciences International*, 42(4):645–662, 2003.

[62] Leonid B Freidovich, Uwe Mettin, Anton S Shiriaev, and Mark W Spong. A passive 2-dof walker: Hunting for gaits using virtual holonomic constraints. *IEEE Transactions on robotics*, 25(5):1202–1208, 2009.

[63] Pedro X Miranda La Hera, Anton S Shiriaev, Leonid B Freidovich, Uwe Mettin, and Sergey V Gusev. Stable walking gaits for a three-link planar biped robot with one actuator. *IEEE Transactions on Robotics*, 29(3):589–601, 2013.

[64] Christine Chevallereau, ER Westervelt, and JW Grizzle. Asymptotically stable running for a five-link, four-actuator, planar bipedal robot. *The International Journal of Robotics Research*, 24(6):431–464, 2005.

[65] Víctor De-León-Gómez, Qiuyue Luo, Anne Kalouguine, J Alfonso Pámanes, Yannick Aoustin, and Christine Chevallereau. An essential model for generating walking motions for humanoid robots. *Robotics and Autonomous Systems*, 112:229–243, 2019.

[66] ER Westervelt, B Morris, and KD Farrell. Analysis results and tools for the control of planar bipedal gaits using hybrid zero dynamics. *Autonomous Robots*, 23(2):131–145, 2007.

[67] B. G. Buss, K. A. Hamed, B. A. Griffin, and J. W. Grizzle. Experimental results for 3d bipedal robot walking based on systematic optimization of virtual constraints. In *2016 American Control Conference (ACC)*, pages 4785–4792, 2016.

[68] Brent Griffin and Jessy Grizzle. Nonholonomic virtual constraints and gait optimization for robust walking control. *The International Journal of Robotics Research*, 36(8):895–922, 2017.

[69] J. W. Grizzle, E. R. Westervelt, and C. Canudas-de-Wit. Event-based pi control of an underactuated biped walker. In *42nd IEEE International Conference on Decision and Control (IEEE Cat. No.03CH37475)*, volume 3, pages 3091–3096 Vol.3, 2003.

[70] JW Grizzle. Remarks on event-based stabilization of periodic orbits in systems with impulse effects. In *Second International Symposium on Communications, Control and Signal Processing*, 2006.

[71] Brent Griffin and Jessy Grizzle. Nonholonomic virtual constraints for dynamic walking. In *2015 54th IEEE Conference on Decision and Control (CDC)*, pages 4053–4060. IEEE, 2015.

[72] Christine Chevallereau, Jessy W Grizzle, and Ching-Long Shih. Asymptotically stable walking of a five-link underactuated 3-d bipedal robot. *IEEE transactions on robotics*, 25(1):37–50, 2009.

[73] Ching-Long Shih, JW Grizzle, and Christine Chevallereau. From stable walking to steering of a 3d bipedal robot with passive point feet. *Robotica*, 30(7):1119–1130, 2012.

[74] Ting Wang, Christine Chevallereau, and David Tlalolini. Stable walking control of a 3d biped robot with foot rotation. *Robotica*, 32(4):551–570, 2014.

[75] Christine Chevallereau, Hamed Razavi, Damien Six, Yannick Aoustin, and Jessy Grizzle. Self-synchronization and self-stabilization of 3d bipedal walking gaits. *Robotics and Autonomous Systems*, 100:43–60, 2018.

[76] ER Westervelt, B Morris, and KD Farrell. Sample-based hzd control for robustness and slope invariance of planar passive bipedal gaits. In *2006 14th Mediterranean Conference on Control and Automation*, pages 1–6. IEEE, 2006.

[77] Volker Dietz. Spinal cord pattern generators for locomotion. *Clinical Neurophysiology*, 114(8):1379–1389, 2003.

[78] Hamed Razavi, Anthony M Bloch, Christine Chevallereau, and Jessy W Grizzle. Symmetry in legged locomotion: a new method for designing stable periodic gaits. *Autonomous Robots*, 41(5):1119–1142, 2017.

[79] Majid Khadiv, Alexander Herzog, S Ali A Moosavian, and Ludovic Righetti. Step timing adjustment: A step toward generating robust gaits. In *Humanoid Robots (Humanoids), 2016 IEEE-RAS 16th International Conference on*, pages 35–42. IEEE, 2016.

[80] LUO Qiuyue. 3d lip self stabilization. `https://github.com/luoyueer/3D_LIP_self_stabilization`, 2020.

[81] Alberto Isidori. The zero dynamics of a nonlinear system: From the origin to the latest progresses of a long successful story. *European Journal of Control*, 19(5):369–378, 2013.

[82] David E. Orin, Ambarish Goswami, and Sung-Hee Lee. Centroidal dynamics of a humanoid robot. *Autonomous Robots*, 35(2):161–176, Oct 2013.

[83] S. Kajita, T. Yamaura, and A. Kobayashi. Dynamic walking control of a biped robot along a potential energy conserving orbit. *IEEE Trans. Robot. Autom.*, 8(4):431–438, 1992.

[84] Ambarish Goswami, Bernard Espiau, and Ahmed Keramane. Limit cycles and their stability in a passive bipedal gait. In *Robotics and Automation, 1996. Proceedings., 1996 IEEE International Conference on*, pages 246–251. IEEE, 1996.

[85] Benjamin Morris and Jessy W Grizzle. A restricted poincaré map for determining exponentially stable periodic orbits in systems with impulse effects: Application to bipedal robots. In *Decision and Control, 2005 and 2005 European Control Conference. CDC-ECC'05. 44th IEEE Conference on*, pages 4199–4206. IEEE, 2005.

[86] Qiuyue LUO. a passive pendulum walking on an uneven ground. `https://www.youtube.com/watch?v=jmIAVi4NKTA&feature=youtu.be`. Accessed March 31, 2020.

[87] Justin Carpentier, Mehdi Benallegue, and Jean-Paul Laumond. On the centre of mass motion in human walking. *International Journal of Automation and Computing*, 14(5):542–551, 2017.

[88] Cynthia R. Lee and Claire T. Farley. Determinants of the center of mass trajectory in human walking and running. *The Journal of experimental biology*, 201:2935–2944, 1998.

[89] Sahab. Omran, Sophie. Sakka, and Yannick Aoustin. Effects of com vertical oscillation on joint torques during 3d walking of humanoid robots. *Int. J. of Humanoid Robotics*, 13(4):1650019, 2016.

[90] Gianluca Garofalo, Christian Ott, and Alin Albu-Schäffer. Walking control of fully actuated robots based on the bipedal slip model. In *2012 IEEE International Conference on Robotics and Automation*, pages 1456–1463. IEEE, 2012.

[91] Kensuke Harada, Kanako Miura, Mitsuharu Morisawa, Kenji Kaneko, Shin'ichiro Nakaoka, Fumio Kanehiro, Tokuo Tsuji, and Shuuji Kajita. Toward human-like

walking pattern generator. In *2009 IEEE/RSJ International Conference on Intelligent Robots and Systems*, pages 1071–1077. IEEE, 2009.

[92] Qiuyue Luo, Victor De-León-Gómez, Anne Kalouguine, Christine Chevallereau, and Yannick Aoustin. Self-synchronization and self-stabilization of walking gaits modeled by the three-dimensional lip model. *IEEE Robotics and Automation Letters*, 3(4):3332–3339, 2018.

[93] Sylvain Miossec and Yannick Aoustin. A simplified stability study for a biped walk with underactuated and overactuated phases. *The International Journal of Robotics Research*, 24(7):537–551, 2005.

[94] Sotiris Apostolopoulos, Marion Leibold, and Martin Buss. Transitioning between underactuated periodic orbits: An optimal control approach for settling time reduction. *International Journal of Humanoid Robotics*, 15(06):1850027, 2018.

[95] Jessy W Grizzle, Christine Chevallereau, Ryan W Sinnet, and Aaron D Ames. Models, feedback control, and open problems of 3d bipedal robotic walking. *Automatica*, 50(8):1955–1988, 2014.

[96] Fuzhen Zhang. *The Schur complement and its applications*, volume 4. Springer Science & Business Media, 2006.

[97] Alberto Isidori. The zero dynamics of a nonlinear system: From the origin to the latest progresses of a long successful story. 19:18 – 25, 08 2011.

[98] Aaron D. Ames, Paulo Tabuada, Austin Jones, Wen-Loong Ma, Matthias Rungger, Bastian Schürmann, Shishir Kolathaya, and Jessy W. Grizzle. First steps toward formal controller synthesis for bipedal robots with experimental implementation. *Nonlinear Analysis: Hybrid Systems*, 25:155 – 173, 2017.

[99] Christine Chevallereau, Hamed Razavi, Damien Six, Yannick Aoustin, and Jessy Grizzle. Self-synchronization and self-stabilization of 3d bipedal walking gaits. *Robotics and Autonomous Systems*, 100(Supplement C):43 – 60, 2018.

[100] Tarik Saidouni and Guy Bessonnet. Generating globally optimised sagittal gait cycles of a biped robot. *Robotica*, 21(2):199–210, 2003.

[101] D. Tlalolini, Y. Aoustin, and C. Chevallereau. Design of a walking cyclic gait with single support phases and impacts for the locomotor system of a thirteen-link 3d biped using the parametric optimization. *Multibody Syst Dyn*, 23:33–56, 2010.

[102] Víctor De-León-Gómez, J. Alfonso Pámanes, and Víctor Santibanez. Experimental evaluation of the real-time walking of a 5 dof biped robot with a gait based on

cycloidal motions. *Revista Iberoamericana de Automática e Informática Industrial RIAI*, 12(04):408–418, 2015.

[103] Jacqueline Romkes and Katrin Bracht-Schweizer. The effects of walking speed on upper body kinematics during gait in healthy subjects. *Gait & Posture*, 54:304–310, 2017.

[104] J. Liu, U. Schwiegelshohn, and O. Urbann. Stable walking of a bipedal humanoid robot involving three-dimensional upper body motion. In *2014 IEEE-RAS Int. Conf. on Humanoid Robots*, pages 80–85, Nov 2014.

[105] Qiuyue LUO. Animation of romeo walking with a constant height and fixed zmp. `https://https://www.youtube.com/watch?v=PrQD0MMWCxg`. Accessed April 11, 2020.

[106] Qiuyue LUO. Romeo walking with a variable height of com and fixed zmp. `https://www.youtube.com/watch?v=nk0QUWCdQco`. Accessed April 11, 2020.

[107] Igor Danilov, Bulat Gabbasov, Ilya Afanasyev, and Evgeni Magid. Zmp trajectory from human body locomotion dynamics evaluated by kinect-based motion capture system. In *Int. Conf. on Computer Vision Theory and Applications (VISAPP)*, pages 160–166, Rome, Italy, 02 2016.

[108] X. Zhang, H. Wang, Y. Shi, C. Fu, H. Wang, and G. Wang. A measure system of zero moment point using wearable inertial sensors. *China Communications*, 13(5):16–27, May 2016.

[109] Y. Aoustin and A. M. Formalskii. Walking of biped with passive exoskeleton: evaluation of energy consumption. *Multibody System Dynamics*, 43(1):71–96, May 2018.

[110] Qiuyue LUO. Romeo walking with a variable height of com and a varying zmp. `https://www.youtube.com/watch?v=tYyEs87GtmQ`. Accessed April 11, 2020.

[111] PAL Robotics. Talos - pal robotics: Leading service robotics. `http://pal-robotics.com/robots/talos/`. Accessed May 10, 2020.

[112] Qiuyue LUO. Talos walking with a variable height of com and varying zmp. `https://www.youtube.com/watch?v=xAjOUcl7I_c`. Accessed April 11, 2020.

[113] Ting Wang, Christine Chevallereau, and Carlos F Rengifo. Walking and steering control for a 3d biped robot considering ground contact and stability. *Robotics and Autonomous Systems*, 60(7):962–977, 2012.

[114] A Kalouguine, V. De-Leon-Gomez, C. Chevallereau, S. Dalibard, and Y. Aoustin. Definition of a walking with starting and stopping motions for the humanoid romeo. In *Icinco 2020, 7-9 Juillet 2020, Paris*, 2020.

[115] Jessy W Grizzle and Christine Chevallereau. Virtual constraints and hybrid zero dynamics for realizing underactuated biped locomotion (proposed chapter).

[116] Yannick Aoustin and AM Formalskii. 3d walking biped: optimal swing of the arms. *Multibody System Dynamics*, 32(1):55–66, 2014.

[117] Mathieu Hobon, Nafissa Lakbakbi El Yaaqoubi, and Gabriel Abba. Gait optimization of a rolling knee biped at low walking speeds. In *ICINCO (2)*, pages 207–214, 2013.

[118] Eric R Westervelt, Jessy W Grizzle, and C Canudas De Wit. Switching and pi control of walking motions of planar biped walkers. *IEEE Transactions on Automatic Control*, 48(2):308–312, 2003.

[119] Ill-Woo Park, Jung-Yup Kim, Jungho Lee, and Jun-Ho Oh. Online free walking trajectory generation for biped humanoid robot khr-3 (hubo). In *Proceedings 2006 IEEE International Conference on Robotics and Automation, 2006. ICRA 2006.*, pages 1231–1236. IEEE, 2006.

[120] Michael Grundy, PA Tosh, RD McLeish, and L Smidt. An investigation of the centres of pressure under the foot while walking. *The Journal of bone and joint surgery. British volume*, 57(1):98–103, 1975.

[121] Mehdi Benallegue, Jean-Paul Laumond, and Alain Berthoz. On the mechanical contribution of head stabilization to passive dynamics of anthropometric walkers. *The International Journal of Robotics Research*, 39(4):461–475, 2020.

Appendices

Appendix A

A.1 Analytical expression of eigenvalue for LIP model

With the landing position of swing foot give by Equation (2.26), we can deduce the expression of the error in position of the CoM ($\delta X = X - X^*$) through the change of support:

$$\begin{aligned} \delta X_{k+1}^+ &= k_S \delta X_k^- \\ \delta Y_{k+1}^+ &= -k_D \delta Y_k^- \end{aligned} \tag{A.1}$$

In presence of perturbation, deduced from Equation (2.39) the final CoM position error satisfies:

$$\delta X_k^- + C \delta Y_k^- = 0 \tag{A.2}$$

For a chosen evolution of the swing leg, the initial position of CoM can be deduced.

To study the stability of the walking gait, the Poincaré return map is used. Since X_k^- and Y_k^- are coupled via the switching manifold (2.39), and the dynamic is autonomous (the time does not appear), the chosen independent state variables are (X_k^-, L_k^-, K_k^-). The Jacobian is defined for a given periodic motion, and is characterized by the direction of the velocity of the CoM α.

Due to the existence of disturbance, the initial state of the robot after step k is written as:

$$\begin{aligned} X_k^+ &= X^{*+} + \delta X_k^+ \\ Y_k^+ &= Y^{*+} + \delta Y_k^+ \\ \dot{X}_k^+ &= \dot{X}^{*+} + \delta \dot{X}_k^+ \\ \dot{Y}_k^+ &= \dot{Y}^{*+} + \delta \dot{Y}_k^+ \end{aligned} \tag{A.3}$$

where $X_0 = -\frac{1}{2}, Y_0 = \frac{1}{2}$. At the end of the step, the state of the robot is denoted as:

$$\begin{array}{rcl} X_k^- & = & -X^{*-} + \delta X_k^- \\ Y_k^- & = & Y^{*-} + \delta Y_k^- \\ \dot{X}_k^- & = & \dot{X}^{*-} + \delta \dot{X}_k^- \\ \dot{Y}_k^- & = & -\dot{Y}^{*-} + \delta \dot{Y}_k^- \end{array} \tag{A.4}$$

Using the fact that $\dot{X}_0$ and $\dot{Y}_0$ define a synchronized motion and neglecting the second order terms, we obtain:

$$L_k = \delta \dot{X}_k \dot{Y}_0 + \dot{X}_0 \delta \dot{Y}_k - \frac{\omega^2}{2}(\delta X_k - \delta Y_k) \tag{A.5}$$

We will now express the final error in velocity as function of the initial error for the step k. As the orbital energies, E_x and E_y and synchronizaiton measure L are conserved quantities, we have:

$$(\dot{X}_k^-)^2 - \omega^2 (X_k^-)^2 = (\dot{X}_k^+)^2 - \omega^2 (X_k^+)^2 \tag{A.6}$$

$$(\dot{Y}_k^-)^2 - \omega^2 (Y_k^-)^2 = (\dot{Y}_k^+)^2 - \omega^2 (Y_k^+)^2 \tag{A.7}$$

$$\dot{X}_k^- \dot{Y}_k^- - \omega^2 X_k^- Y_k^- = L_k^- \tag{A.8}$$

Submit equation (A.3) and (A.4) into equation (A.6), (A.7) and (A.8) and neglect the second order terms, we can obtain:

$$\begin{array}{c} (\delta \dot{X}_k^-)^2 + 2\delta \dot{X}_k^- \dot{X}_0 + \dot{X}_0^2 - \frac{\omega^2}{4} - \omega^2 \delta X_k^- - \omega^2 (\delta X_k^-)^2 = \\ (\delta \dot{X}_k^+)^2 + 2\delta \dot{X}_k^+ \dot{X}_0 + \dot{X}_0^2 - \frac{\omega^2}{4} + \omega^2 \delta X_k^+ - \omega^2 (\delta X_k^+)^2 \end{array} \tag{A.9}$$

$$\begin{array}{c} (\delta \dot{Y}_k^-)^2 - 2\delta \dot{Y}_k^- \dot{Y}_0 + \dot{Y}_0^2 - \frac{\omega^2}{4} - \omega^2 \delta Y_k^- - \omega^2 (\delta Y_k^-)^2 = \\ (\delta \dot{Y}_k^+)^2 + 2\delta \dot{Y}_k^+ \dot{Y}_0 + \dot{Y}_0^2 - \frac{\omega^2}{4} - \omega^2 \delta Y_k^+ - \omega^2 (\delta Y_k^+)^2 \end{array} \tag{A.10}$$

$$L_k^- = \dot{X}_0 \delta \dot{Y}_k^- - \delta \dot{X}_k^- \dot{Y}_0 - \frac{\omega^2}{2}(\delta X_k^- + \delta Y_k^-) \tag{A.11}$$

Using these equations and neglecting the second order terms, we obtain:

$$\delta\dot{X}_k^- = \frac{\omega^2}{2\dot{X}_0}(\delta X_k^- + \delta X_k^+) + \delta\dot{X}_k^+ \tag{A.12}$$

$$\delta\dot{Y}_k^- = \frac{\omega^2}{2\dot{Y}_0}(-\delta Y_k^- + \delta Y_k^+) - \delta\dot{Y}_k^+ \tag{A.13}$$

Submit equation (A.12) and (A.13) into equation (A.11) and rearrange it, we obtain:

$$\begin{aligned}(1-\frac{1}{\alpha})\delta Y_k^- + (1-\alpha)\delta X_k^- = \\ \alpha\delta X_k^+ - \frac{\delta Y_k^+}{\alpha} - \frac{4L_k}{\omega^2} - \delta X_k^+ + \delta Y_k^+\end{aligned} \tag{A.14}$$

Because of the fact that:

$$\delta X_k^- = -C\delta Y_k^- \tag{A.15}$$

$$\delta X_k^+ = \frac{k_S C}{k_D}\delta Y_k^+ \tag{A.16}$$

Thus replace δY with δX in equation (A.14) and rearrange it, we obtain:

$$\begin{aligned}\frac{(-1+\alpha)(1+\alpha C)}{\alpha}\delta Y_k^- = \\ \frac{(-1+\alpha)(\alpha C k_S + k_D)}{\alpha k_D}\delta Y_k^+ - \frac{4L_k}{\omega^2}\end{aligned} \tag{A.17}$$

From the geometric relationship, we know that:

$$\delta X_{k+1}^+ = k_S\delta X_k^- \tag{A.18}$$

$$\delta Y_{k+1}^+ = -k_D\delta Y_k^- \tag{A.19}$$

Thus, from equation (A.17), we can obtain:

$$\begin{aligned}-[1-\frac{1}{\alpha} - C(1-\alpha)]\delta X_{k+1}^+ = \\ (\frac{k_S C}{k_D}\alpha - \frac{1}{\alpha} - \frac{k_D C}{k_D} + 1)\delta X_k^+ - \frac{4L_k k_S C}{\omega^2}\end{aligned} \tag{A.20}$$

and then:

$$\delta X_{k+1}^+ = -\frac{k_D + \alpha C k_S}{1+\alpha C}\delta X_k^+ + \frac{4\alpha C k_S}{\omega^2(-1+\alpha)(1+\alpha C)}L_k \tag{A.21}$$

From equation (A.17), we know that:

$$\delta X_k^- = -C(\frac{-4\alpha L_k}{\omega^2(-1+\alpha)(1+\alpha C)} + \frac{k_D+\alpha C k_S}{k_D+\alpha C k_D}\delta Y_k^+ \tag{A.22}$$

$$\delta Y_k^- = \frac{-4\alpha L_k}{\omega^2(-1+\alpha)(1+\alpha C)} + \frac{k_D+\alpha C k_S}{k_D+\alpha C k_D}\delta Y_k^+ \tag{A.23}$$

Submit equation (A.22) and (A.23) into equation (A.12) and (A.13), we obtain:

$$\begin{aligned}\delta \dot{X}_k^- = \delta \dot{X}_k^+ + \frac{2C\alpha L_k}{\dot{X}_0(-1+\alpha)(1+\alpha C)} + \frac{\omega^2 \delta X_k^+}{2\dot{X}_0} - \\ \frac{C\omega^2(k_D+\alpha C k_S)\delta Y_k^+}{2(k_D+\alpha C k_D)\dot{X}_0}\end{aligned} \tag{A.24}$$

$$\begin{aligned}\delta \dot{Y}_k^- = -\delta \dot{Y}_k^+ + \frac{2\alpha L_k}{\dot{Y}_0(-1+\alpha)(1+\alpha C)} + \\ \frac{\alpha\omega^2 C(k_D-k_S)}{2(1+\alpha C)k_D\dot{Y}_0}\delta Y_k^+\end{aligned} \tag{A.25}$$

For the step $k+1$, the synchronization measure is:

$$L_{k+1}^- = \dot{X}_0 \delta \dot{Y}_{k+1}^- - \delta \dot{X}_{k+1}^- \dot{Y}_0 - \frac{\omega^2}{2}(\delta X_{k+1}^- + \delta Y_{k+1}^-) \tag{A.26}$$

Submit equation (A.24) and (A.25) into (A.26) and rearrange it, we obtain the relationship between L_{k+1}, L_k and δX_K^+:

$$\begin{aligned}L_{k+1} = &\frac{(1+\alpha)(\alpha C-1) - 2\alpha(k_D - Ck_S)}{(1-\alpha)(\alpha C+1)} L_k + \\ &\frac{(-1+C+Ck_S-k_D)(k_D+\alpha C k_S)\omega^2}{2(1+\alpha C)Ck_S}\delta X_k^+\end{aligned} \tag{A.27}$$

In conclusion, the Jacobian matrix is:

$$J = \begin{bmatrix} -\frac{k_D+\alpha C k_S}{(k_S+\alpha C)} & \frac{4\alpha C k_S}{\omega^2(1+\alpha C)(\alpha-1)} & 0 \\ J_{21} & \frac{2\alpha(k_D-Ck_S)+(1-\alpha C)(\alpha+1)}{(1+\alpha C)(\alpha-1)} & 0 \\ * & * & 1 \end{bmatrix} \tag{A.28}$$

with $J_{21} = \frac{(k_D+\alpha C k_S)(-1+C+Ck_S-k_D)\omega^2}{2(1+\alpha C)Ck_S}$.

Appendix B

B.1 Publications

B.1.1 Journal Papers

— Q. Luo, V. De-León-Gómez, A. Kalouguine, C. Chevallereau and Y. Aoustin, *Self-Synchronization and Self-Stabilization of Walking Gaits Modeled by the Three-Dimensional LIP Model*[J], IEEE Robotics and Automation Letters, 2018, 3(4): 3332-3339 (presented in IROS2018)

— Q. Luo, C. Chevallereau, and Y. Aoustin, *Walking Stability of a Variable Length Inverted Pendulum Controlled with Virtual Constraints*[J], International Journal of Humanoid Robotics, Vol. 16, No. 06, 1950040 (2019)

— V. De-León-Gómez, Q. Luo, A. Kalouguine, J.A. Pámanes, Y. Aoustin, and C. Chevallereau, *An essential model for generating walking motions for humanoid robots*[J], Robotics and Autonomous Systems, 2019, 112: 229-243.

B.1.2 Conferences

— Q. Luo, V. De-León-Gómez, A. Kalouguine, C. Chevallereau, and Y. Aoustin, *Self-Synchronization and Self-Stabilization of Walking Gaits Modeled by the Three-Dimensional LIP Model*, 2018 IEEE/RSJ International Conference on Intelligent Robots and Systems, October, 1-5, 2018 Madrid, Spain.

Titre : Marche Bipède 3D Auto-Stabilisante

Mot clés : Robotique, marche bipède, Stabilité

Résumé : Les robots humanoïdes, bien adaptés pour évoluer dans le milieux humains, peuvent avec leurs bras et mains effectuer des tâches complexes. Ils peuvent être considérés comme l'un des robots ultimes. Cependant, la marche bipède reste un phénomène complexe qui n'a pas été entièrement compris.

La thèse est consacrée à trouver quelques caractéristiques physiques qui peuvent expliquer la stabilité de la marche périodique sur le sol horizontal. Dans la marche humaine, la démarche est généralement exprimée en fonction d'une variable de phase fondée sur l'état interne au lieu du temps. Les variables commandées (trajectoires du pied libre, oscillation verticale du centre de masse (CdM), mouvement du haut du corps, etc.) des robots ont une évolution désirée exprimée en fonction d'une variable de phase via l'utilisation de contraintes virtuelles et la durée des pas n'est pas explicitement imposée mais implicitement adaptée en présence de perturbations. Dans la première partie, deux modèles simplifiés du robot : le modèle du pendule inversé linéaire (LIP) et le modèle du pendule inversé de longueur variable (VLIP) sont utilisés pour étudier les stratégies de commande. La stratégie de commande proposée pour les modèles LIP et VLIP est étendue à travers le modèle essentiel pour commander un modèle humanoïde complet.

L'algorithme de marche proposé ci-dessus est appliqué sur les robots humanoïdes Roméo et TALOS.

Title: Self-stabilization of 3D Walking of a Biped Robot

Keywords: Robotics, biped walking, stability

Abstract: Humanoid robot, which can walk by two legs and perform skillful tasks using both arms with hands, could be considered as one of the ultimate robots. However, bipedal walking remains a complex phenomenon that has not been fully understood.

The thesis is dedicated to find some physical insights that can explain the stability of periodic walking on horizontal floor. In human walking, the gait is usually expressed as a function of a phasing variable based on the internal state instead of time. The controlled variables (swing foot trajectories, vertical oscillation of center of mass, upper body motion, etc.) of the robots are based on a phasing variable via the use of virtual constraints and the step timing is not explicitly imposed but implicitly adapted under disturbances. Firstly, simplified models of the robot: the linear inverted pendulum (LIP) model and variable length inverted pendulum (VLIP) model are used to study control strategies. The proposed control strategy for the LIP and VLIP models is extended through the proposed essential model to control a complete humanoid model.

The walking algorithm proposed above is applied on the humanoid robots Romeo and TALOS.